Compressive Raman Imaging: Applications in pharmacology and environmental sciences

Clément Grand

NNT/NL : 0000AIXM0000/000ED000

THÈSE DE DOCTORAT

Soutenue à Aix-Marseille Université

Le 7 Décembre 2022 par
Clément GRAND

Compressive Raman Imaging: Applications in pharmacology and environmental sciences

Discipline
Physique et Sciences de la matière

Spécialité
Optique, Photonique et Traitement d'Image

École doctorale
352, Physique et sciences de la matière

Composition du jury

Éric FINOT	Rapporteur
Professeur	
Randy BARTELS	Rapporteur
Professeur	
Julien DUBOISSET	Examinateur
Maître de conférence	
Enora PRADO	Examinatrice
Chargée de recherche	
Andreas ZUMBUSCH	Examinateur
Professeur	
Sophie Brasselet	Présidente du jury
Directrice de Recherche	
Hervé RIGNEAULT	Directeur de thèse
Directeur de recherche	

Abstract

Recent developments in Raman microspectroscopy have extended its application to biology, medicine and pharmaceutical sciences. A prime example is the significant improvements in imaging sensitivity and speed that have enabled to apply Raman to biomedical research. Raman imaging is nowadays a new imaging modality that can provide molecular level information in biological systems inaccessible by conventional optical techniques. Raman imaging provides label free, non-destructive, high chemical selectivity with superb optical resolution.

However, Raman-based microspectroscopy still has its drawbacks. In general, the Raman signal is scattered and detected by a camera to ultimately form a hyperspectral image. This generates large volumes of data, as well as requires very long acquisition times. The high data volume inherent in Raman microspectroscopy is the major challenge that prevents dynamic spectral imaging fore live applications.

In this thesis, we used the Compressive Raman Technology (CRT), the development of which represents a significant advance in the field of Raman spectroscopy. CRT speeds up the measurement process and simultaneously simplifies the data analysis. CRT uses a programmable filter located in the spectral plane of a spectrometer. It is then possible to select a set of Raman lines specific to a chemical compound and detect them not with a camera, but with a faster single-pixel detector. The technology is accompanied by a suite of algorithms that define the optimal filters to detect and identify known chemical species and recover their proportions. We apply first CRT imaging for the quantification of chemical species in the context of polymorph active molecular ingredient in pharmaceutical tablets. Second CRT imaging is applied for the detection of micro-plastics coming from natural environmental samples. In both cases we demonstrate the superiority of CRT imaging as compared to conventional Raman approaches.

Contents

Introduction

I have a quite atypical academic cursus coming from environment and biology background I ended up doing a PhD in Physics. The main reason to do a thesis is (for me) to learn new things without staying in the same field of study. In the search of new approaches that could allow to progress in my fields of interest such as ecology. I could read a paper that was using laser light to interrogate the molecular content of a sample. This reading was the turning point and I decided to go further into this direction and new field for me. Scientific articles linking disciplines such as physics, biology, ecology or evolution presented the Raman technique as a candidate to learn more about the intimate molecular structure of an unknown sample [1] [2] [3]. *I convinced myself that molecular Raman spectroscopy and imaging could fit well with the conceptual, technical and pragmatic considerations of ecology* [2].

Spontaneous Raman spectroscopy is a molecular spectroscopy technique based on the interaction of light with matter [4]. It brings information on the composition or characteristics of the material owing to an inelastic light scattering process. When light interacts with molecules in gas, liquid or solid media, the vast majority of photons are scattered or propagated but the kinetic energy of the excitatory photons is conserved. This phenomenon is called elastic scattering, or Rayleigh scattering. A small number of photons, approximately 1 photon for 10 million, will scatter at a different frequency from the excitatory photons [5]. This process is called inelastic scattering, or the Raman effect [4]. This effect was predicted by A.G. Smekal in 1923 [6], and demonstrated experimentally for the first time in 1928, by C. V. Raman (laureate of the Nobel Prize in 1930) and K. S. Krishnan while looking for an optical analogue of the Compton effect (1928) in India and by G. Landsberg and L. Mandelstam (1928) in the Soviet Union [7]. Since then, the Raman effect has been used in a wide range of applications, from medical diagnostics to materials science to reaction analysis.
Raman spectroscopy provides information on intra- and intermolecular vibrations induced by a light stimulus. The vibrational spectrum of a molecule appears as a "molecular fingerprint" or a molecular specific "barcode" [8]. This barcode identifies a substance, its structure and the way it interact with the molecules around it. Because Raman scattering results from the interaction of light with the intrinsic vibration of molecules. A label free technique requires no sample preparation.

Nevertheless, two notable factors constrain the use of hyperspectral Raman imaging on a larger scale, despite its multiple advantages. The Raman scattering efficiency process is a first factor because it is extremely low: only about 10^{-6} of the incident intensity is converted into Raman signal and thus leads to low signal levels (especially in endogenous compounds) and long integration times [9] [10]. Imaging an area of a few hundred μm can easily take minutes or even hours with currently available instruments. This limits the implementation of spontaneous Raman imaging to slow dynamics and ex-vivo studies.

The development and use of coherent Raman scattering could be an effective solution which will come at the expense of spectral range or resolution, cost and complexity [11].
If the information contained in a hyperspectral image is considerably more complete than in other imaging techniques (*i.e*. fluorescence), but it comes at the expense of an immeasurably greater volume of data. This represents the second constrain of hyperspectral Raman imaging where an image of a few hundred μm generates several gigabytes of data.
In the case of hyperspectral imaging, the data acquired is generally very compressible [12] [13]. This parameter is relevant in order to be able to find a more efficient way not only to store, but also to acquire data. The recent theoretical and technological progress makes it possible not only to better compress the data after acquisition, but also to apply this compressibility further upstream to acquire less data. This is to achieve faster and smaller acquisitions in terms of memory used [12] [14] [15]. Under certain conditions, this paradigm can go further: the acquisition process can be modified in such a way that the partial processing is carried out directly in the hardware [16] [17]. This also reduces the need for post-processing sessions.

In this thesis, we develop and use an imaging method named compressive Raman technology (CRT) to overcome the speed and storage limitation on conventional Raman. Unlike commercial devices that record the full Raman spectrum on an array detector, CRT selects and combines some specific Raman lines on a fast single-pixel detector. The spectral components are selected (i) numerically with an optimisation procedure which minimizes the estimation variance, and (ii) physically with a programmable optical filter (digital micromirror device (DMD) [15]). This programmable optical filter is located in the spectral plane of a spectrometer [18]. A suite of algorithms that define the optimal spectral filters for detecting known chemical species and recovering their concentrations accompanies the technology [19] [20] [21]. CRT aims to obtain a substantial acceleration as well as a massive reduction in the volumes of data generated.

The work carried out in this thesis has enabled the development of CRT, in particular through two applications where the adaptability and efficiency of CRT have been demonstrated.
The background and the advantages of Raman spectroscopy are presented in the first chapter, but also the limits of the technique. The discussion continues by describing alternative acquisition methods and recent improvements.
This path leads directly to chapter 2 where the main principles of compressive Raman are introduced. Firstly, various concepts are presented to introduce the processes on which CRT is based. At the same time, we show that the efficiency of these processes helps to justify a simpler, optimized and faster workflow for compressive Raman imaging. A comparison between conventional and compressive spectrometers is presented. We then present our configuration of CRT, oriented for application purposes,

with detailed descriptions of the different components and their key roles. This chapter ends with a simple experimental implementation on a test sample.
Chapters 3 and 4 represent the application part of this thesis. CRT is applied to the fields of chemical sensing for health problems and pharmacology, initially, with precise analysis of the composition of drugs. It will then be translated, to an important environmental problem : the detection of plastic pollution. In these two application chapters, we demonstrate the effectiveness of CRT to detect, classify, quantify ad image molecular species present in the samples.
Finally, the potential of CRT will be presented in Chapter 5 where scopes for improvement the technology, but also concrete collaborative projects are described.

This work, builds up on the initial PhD of C. Scotté on CRT and results from a collaboration with P. Réfrégier, F. Galland and T. Justel from the signal processing team (PhyTI) of the Fresnel Institute. External collaborations include the laboratories of SANOFI (Montpellier, France) and IFREMER (Brest, France).

Chapter 1

Introduction to the method of using the Raman Effect

Contents

This chapter introduces the physical and chemical principles underlying Raman scattering and the methods based on this phenomenon. This description highlights the context and the issues related to Raman scattering and is based on recently published research works. The phenomenon behind Raman scattering will first be presented from a classical perspective. While this simplified approach is defective to fully understand the mechanisms, it provides a general qualitative understanding and explains the basic principles of spontaneous Raman scattering.

The important features and advantages of Raman spectroscopy will be mentioned but also the limitations of the technique. We will continue the discussion by describing alternative acquisition methods and recent improvements to finally end up on the analysis of compressive Raman which will be quickly introduced here and will be seen in detail in the second chapter of this thesis. Finally we will present the compressive Raman analysis. The books of D. Long [5], a tutorial article by H. Rigneault and P. Berto [22], and the doctoral thesis by C. Scotté [23] mainly inspire this chapter.

1.1 Raman effect: Historical development

1.1.1 Discovery of the Raman effect

In all preliminary studies of light scattering, centuries ago, the light source was the sun. A light beam passing through a dense medium induces different processes. Light is partially reflected, scattered and transmitted through the sample, with a certain amount of loss (Fig. 1.1). At thermodynamic equilibrium, refraction (deflection of the light wave at the interface between two media), absorption (temporary conservation of light energy by the molecule or solid) and diffusion govern the interaction light with matter.

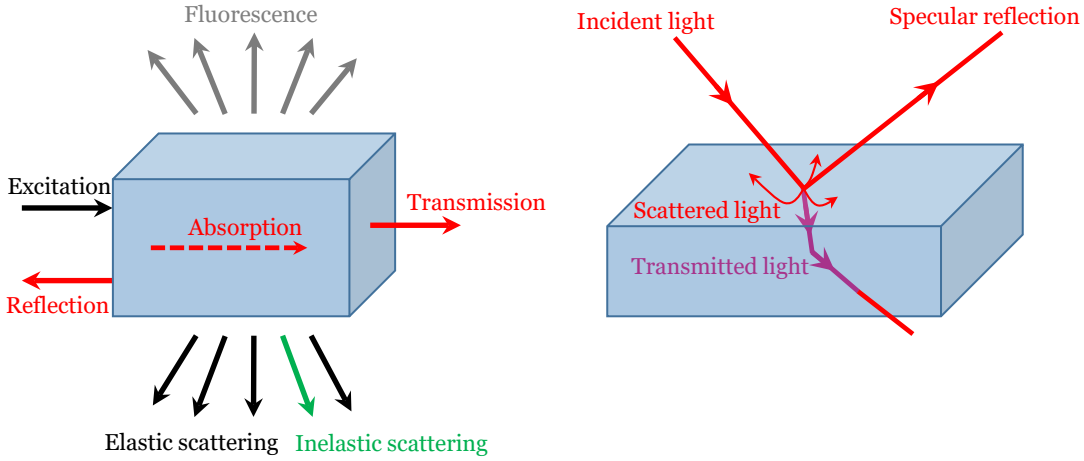

Figure 1.1: Schematic representation of different phenomena produced in the interaction between radiation and dense medium.

Light scattering is indicated by the instantaneous deviation by the molecule from a part of the light beam in multiple directions and different from that of the incoming beam. Most of the scattered light has the same energy as the incident light. This phenomenon of elastic scattering of light at the incident wavelength is called Rayleigh scattering. However, a small part of the scattered photons (about one photon out of 10^6) gains or loses energy and therefore experiences a wavelength shift. This physical phenomenon is called Raman scattering, an inelastic molecular dispersion of light [5] [24] [25]. It is directly opposed to infrared spectrometry based on the absorption process. Raman scattering was predicted by A.G. Smekal in 1923 [6], and demonstrated experimentally in India for the first time in 1928 by C.V. Raman (Nobel Prize winner in 1930) and K.S. Krishnan by seeking an optical analogue of the Compton effect (1928). This effect was also found at the same time by and by G. Landsberg and L. Mandelstam (1928) in the Soviet Union [4], [7]. By focusing spectrally filtered sunlight in a material, it was possible to observe new frequencies in the scattered light.

1.1.2 Infrared spectroscopy: A direct and historic competitor to Raman spectroscopy

During the first years after its discovery, the Raman effect has been extensively addressed in more than 700 articles in the scientific literature, mainly by physicists and chemists who used it to study the vibration and rotation of molecules and to link these phenomenon to molecular structure [26]. By the late 1930s, the Raman effect had become the primary method of non-destructive chemical analysis of compounds, organic and non-organic, as providing to scientists a way to elucidate the vibrational modes of molecules using visible light. It was a ubiquitous technique, providing qualitative and quantitative information in a plethora of samples. Then, as noted the biographer Raman G. Venkataraman, there was a decline in interest, as "*the first bloom of novelty had worn off and physicists were satisfied that they understood the origin of the effect*".

The development of infrared (IR) spectroscopy, still at the end of the 1930s, was, in part, motivated and facilitated by the (un)advances of Raman spectroscopy. The techniques have similarities. They are both molecular vibrational signatures by observing localized bonds. However, IR observes electric dipole moment variations, while Raman observes electric polarizability variations. The spectra also differ, with IR showing irregular absorbance lines and Raman showing a scattered Rayleigh line and the Stoke/anti-Stoke lines [27]. A practical example of differentiating between these two approaches is the study of a crystallization process, in which Raman spectroscopy analyses the solid crystal form(s) and IR spectroscopy simultaneously measures characteristics of the solution phase, such as supersaturation [28].

This is why the rules for selecting the excitations “seen” by Raman and IR are slightly different and provide complementarity information [29]. IR spectroscopy is not, *a priori*, a superior technique to Raman spectroscopy. In particular, it has certain important constraints, such as its sensitivity to the presence of water, the influence of the local atmosphere, etc. [30]. Nevertheless, its deployment was much faster, mainly for practical reasons. IR instruments are more accessible and very easy to use for academic communities. Consequently, the Raman technique remained little used for a few years and confined only to a limited number of research laboratories.

The use of Raman spectroscopy as a basic analytical tool changed considerably after the Second World War. During the war, IR spectroscopy was reinforced by the development of sensitive detectors and advances in electronics. IR measurements quickly became routine operations, while Raman measurements still required skilled operators and darkroom facilities. Raman spectroscopy could no longer compete with IR until other developments in physics - the laser (1960) and the cameras (1980) - worked to revive Raman spectroscopy in a new form from the 1960s. In addition, in the 1980s, the development of IR spectroscopy gave a boost to Raman spectrometry. They go so far as to merge with

the development of Fourier transform Raman which prefigures the real revival of Raman spectrometry [31]. Finally, and thanks to the enormous advances in IR spectroscopy, Raman spectroscopy can be used as a routine analytical technique. Many laboratories are using Raman spectroscopy for analyses where IR spectroscopy could not be used in the field of analysis of polymorphs [32], local microcrystalline structure [33], aqueous systems [34], etc.

It was also at this time that a technical development indirectly introduced a new advantage for the deployment of Raman spectroscopy. Indeed, astronomy pushes for the development of new instruments having some similarities with the needs of Raman spectroscopy. As in the case of Raman scattering, it involves capturing very small quantities of photons (emitted by stars) at very specific wavelengths. This requires very high resolution spectrometers, and avoiding the glare of the detector by light sources close to the point of analysis (filter light from stars close to those studied or, in the Raman case, avoid recording the light from the laser beam). This is how charge coupled devices (CCD detectors) and powerful new Rayleigh filters were made available to the public.

At the end of the 1980s and the beginning of the 1990s, the scientific community finally had a large number of Raman instruments and the technique regained significant momentum and became routine in certain university laboratories. However, the number of equipped industrial laboratories remains very low, except in the pharmaceutical sector which makes extensive use of it for the characterization of new compounds and for identifying polymorphs.

We need to close this historical description to make room for a more in-depth explanation of the different mechanisms that we have introduced here. In particular, we will develop the notion of molecular vibration, then we will continue with the very principles of spontaneous Raman to the limits of this process. From these discussions we will be able to bounce back on the existing solutions including our technology on which this thesis is based.

1.2 Spontaneous Raman scattering

1.2.1 Molecular vibration notion

What is a molecular vibration? How can a molecule vibrate? Rather than talking directly about the principles of spontaneous Raman scattering, these questions will be answered first. An understanding will thus be provided on the notion of molecular vibration in the simplest way, without going into too much detail.

At a molecular level, the atoms are linked through molecular orbitals filled with electrons brought into play by the atoms; these bonds are sorts of "bridges" between two atoms, which accommodate at least two electrons, shared in a more or less balanced way by the atoms.
When a molecule is subjected to electromagnetic waves in the IR range, these waves interact specifically with the bonds, which leads the molecule to "vibrate", *i.e.* to make atoms approach and move away from each other. Each bond has its own characteristics whose depends on the atoms composing the bond (in terms of size, valence and atomic mass) and their electrons involved, but also depending on the surroundings. This is why each bond specifically absorbs certain wavelengths in the IR, while remaining transparent to other wavelengths in the IR [35].

In order to complete these answers in a somewhat more schematic way, we must begin the study of a very simple system by adopting a classical wave point of view. A molecule of diatomic gas is thus considered (Fig. 1.2). The two atoms, of masses $m_1$and m_2 are connected by a chemical bond, similar to a spring aligned on the x-axis. As with a conventional mass-spring-mass system, this bond-atom assembly can vibrate.

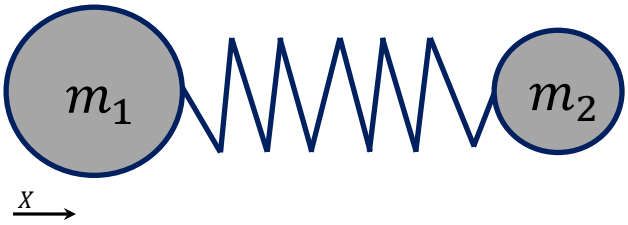

Figure 1.2: Simple model of the gas molecule

For this molecule, it is necessary to refer to the following equation to obtain a description faithful to the experimental observations. This case study is also called the harmonic oscillator [36] [37].

$$\upsilon_0 = \frac{1}{2\pi}\sqrt{\frac{k}{\mu}} \tag{1.1}$$

Where $\mu = \frac{m_1 m_2}{m_1+m_2}$ is the reduced mass of the system (in kg) and k the stiffness constant (or "force constant") of the connection (in N/m). The frequency υ_0 thus depends specifically on the molecule studied.
The vibrational states of a molecule can be probed in different ways. The most direct way is IR spectroscopy, since vibrational transitions generally require an amount of energy that corresponds to the IR region of the spectrum. In our case study Raman spectroscopy which, unlike direct absorption processes, generally uses visible light, can also be used to directly measure vibrational frequencies. Also, in Raman scattering, the frequency of the applied electric field need not to match the resonant

frequencies of the system. On the contrary, the electric field must simply induce a disturbance of the electronic cloud [29] [30].

1.2.2 Principle

Among the existing analytical techniques, Raman spectroscopy is widely used in research laboratories. Indeed, the wide range of analysable materials, the diversity of features that can be measured (nature and chemical structure, orientation of molecules etc.) as well as the non-invasive aspect of this method, explains its popularity [38]. The phenomenon of Raman scattering concerns photons, which is why we use here classical and quantum mechanics to understand the phenomenon correctly.

To begin with, at the microscopic scale, molecules can be visualized as a set of dipoles with positive (nuclei) and negative (electrons) charges. The electrons are found in the area surrounding the nucleus and are an integral part of the atom: this area is called the "electron cloud". Under the influence of an oscillating electric field $\vec{E}$, the positively charged particles vibrate in one direction (that of the electric field $\vec{E}$), while the others, negatively charged, vibrate in the other direction (opposite direction to that of the field $\vec{E}$). In dielectric materials, these charges being bound by electrostatic interactions, there is a certain elasticity of the bond between the charges. Their movement, according to the frequency of the oscillating field $\vec{E}$, create an oscillating dipole. In the Figure 1.3, a representation at the molecular scale shows this oscillation of an electron bound to its nucleus.

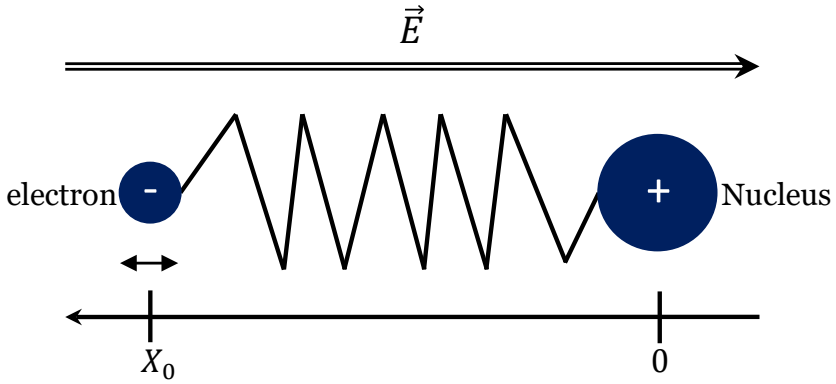

Figure 1.3: Schematic representation of an oscillating electric dipole

In a classical approach, the inelastic scattering of light arises from an induced dipole oscillating at a frequency different from that of the incident light. The polarizability assesses the response of the electron cloud to the external electric field $\vec{E}$.

As soon as the material studied is subjected to a monochromatic electromagnetic wave of frequency $\boldsymbol{\omega}$, it is possible to model the deformation of the electronic field as a spring which oscillates slightly around its equilibrium position at the frequency $\boldsymbol{\omega}$:

$$\vec{E} = \vec{E}_0 \cos(\omega t) \tag{1.2}$$

The response of the molecule to the perturbation $\vec{E}$ can be measured with the electric dipole moment $\vec{P}$:

$$\vec{P} = [\alpha]\vec{E} \tag{1.3}$$

[α] being the polarizability tensor of the molecule (or of the solid). It represents the response capacity (in the case of charge displacement) of the electronic cloud to deform when submitted to an external electric field $\vec{E}$. It reads as follows:

$$\alpha = \begin{pmatrix} \alpha_{XX} & \alpha_{XY} & \alpha_{XZ} \\ \alpha_{YX} & \alpha_{YY} & \alpha_{YZ} \\ \alpha_{ZX} & \alpha_{ZY} & \alpha_{ZZ} \end{pmatrix}$$

Where α_{ij} are the components of α in the frame (Oxyz).

The dipole moment $\vec{P}$ will then be defined by the expression below, equivalent to equation (1.2):

$$\begin{pmatrix} P_X \\ P_Y \\ P_Z \end{pmatrix} = \begin{pmatrix} \propto_{XX} & \propto_{XY} & \propto_{XZ} \\ \propto_{YX} & \propto_{YY} & \propto_{YZ} \\ \propto_{ZX} & \propto_{ZY} & \propto_{ZZ} \end{pmatrix} \begin{pmatrix} E_X \\ E_Y \\ E_Z \end{pmatrix}$$

Polarizability evaluates the response of the electron cloud to the external electric field. It increases as the volume occupied by the bonding electrons increases. The vibrations can be represented by the variation of the normalized coordinate, u, of the displacement of the atoms compared to their equilibrium position, u_0, at a frequency Ω of the following form:

$$u = u_0 \cos(\Omega t) \tag{1.4}$$

The first order development of polarizability as a function of the u coordinate gives:

$$[\alpha] = [\alpha_0] + \left[\frac{\partial[\alpha]}{\partial u}\right]_{u=u_0} (u - u_0) \tag{1.5}$$

Where $[\alpha_0]$ being the polarizability tensor undisturbed by the nuclear movement. The combination of equations (1), (2), (3) and (4) gives:

$$\vec{P} = [\alpha_0]\ \vec{E}_0\, cos(\omega t) + \left[\frac{\partial[\alpha]}{\partial u}\right]_{u=u_0} (u - u_0)\, u_0 \vec{E}_0\, cos(\Omega t) cos(\omega t) \qquad (1.6)$$

However,

$$\cos(\Omega t)\cos(\omega t) = {}^{1}/_{2}\left[\cos\big((\omega - \Omega)t\big) + \cos\big((\omega + \Omega)t\big)\right] \qquad (1.7)$$

So the expression of polarization becomes:

$$\vec{P} = [\alpha_0]\ \vec{E}_0 \cos(\omega t) + {}^{1}/_{2}\left[\frac{\partial[\alpha]}{\partial u}\right]_{u=u_0} u_0 \vec{E}_0\left[\cos\big((\omega - \Omega)t\big) + \cos\big((\omega + \Omega)t\big)\right] \qquad (1.8)$$

In equation (1.8), the first term is a dipole oscillating at the frequency ω, giving rise to elastic Rayleigh scattering. In that case, the electronic dipole radiation oscillates at same frequency identically that of the incident electromagnetic wave. The other two terms correspond to two dipoles radiating at ω and oscillating at frequencies $\omega - \Omega$ and $\omega + \Omega$. They are responsible for Raman Stokes and Anti-Stokes scattering, respectively, and come from energy transfer between light and molecules. During the interaction, the molecule reaches a higher energetic state with a short lifespan called "virtual state" (Fig. 1.4). Thus, the system being excited into a virtual level of energy by absorption of an incident photon is correlated to a photon being emitted with the same energy in the case of Rayleigh scattering, and different energy in the case of Raman scattering [39]. In the latter case, the system transits to a different energy level than its initial state. For Stokes scattering ($\omega - \Omega$), the final state has higher energy than the initial one while for anti-Stokes scattering ($\omega + \Omega$), the system reaches a lower energy level. Therefore, the energy difference between the incident and the scattered photons matches the energy shift between two vibration levels of the molecule (or of the solid). As a result, using monochromatic light and analysing the spectrum of scattered light enables to recover the vibrational spectrum of molecules (or solids) concerned.

The energy of the scattered light is shifted from that of the incident wave by a value equal to the energy transition between vibration states of the molecule. According to this approach, the Stokes scattering and the anti-Stokes scattering would be of the same intensity. However, experimentally, the intensity of the Stokes scattering is always (excluding resonance) greater than that of the anti-Stokes scattering. The simplified Jablonski diagram corresponding to the different scattering processes is shown in Fig. 1.4. This diagram is an energy diagram. It arranged with energy on a vertical axis. The energy levels can be quantitatively denoted, but most of these diagrams use energy levels schematically. The rest of the diagram is arranged into columns.

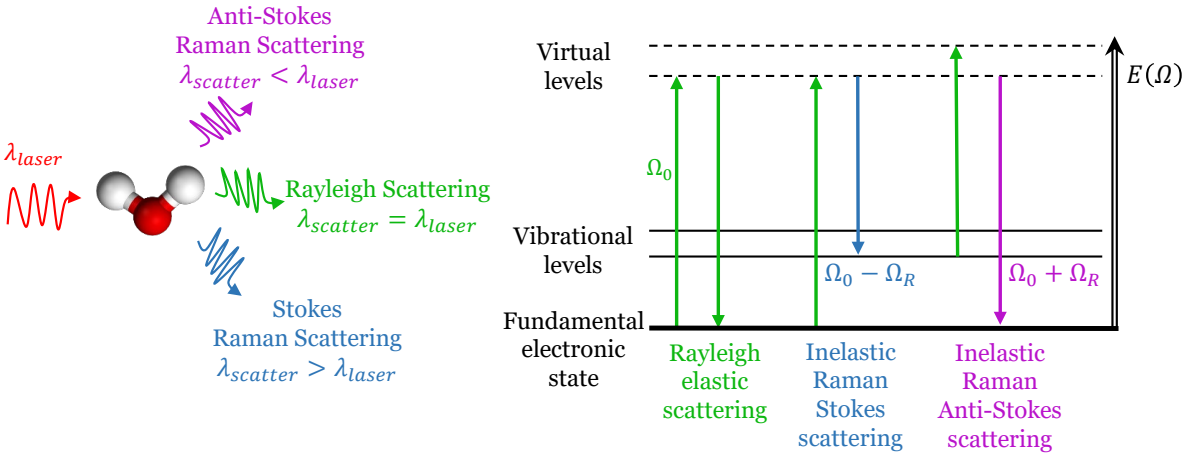

Figure 1.4: Different energy transitions that can take place during a Raman analysis. Ω_0 corresponds to the excitation frequency of the laser, Ω_R corresponds to the vibration frequency of the molecule. The vertical axis represents energy (E) analysed.

The probability that the system is initially in an excited vibrational level is always lower than the probability that it is in the fundamental level at ambient temperature, but it increases with temperature according to Boltzmann's law. Consequently, as it has already been said, except under resonant excitation conditions, the Raman Stokes scattering is always more intense than the anti-Stokes scattering and the ratio of their intensities depends on the temperature and the frequency of the vibration concerned. (Fig 1.5) [40].

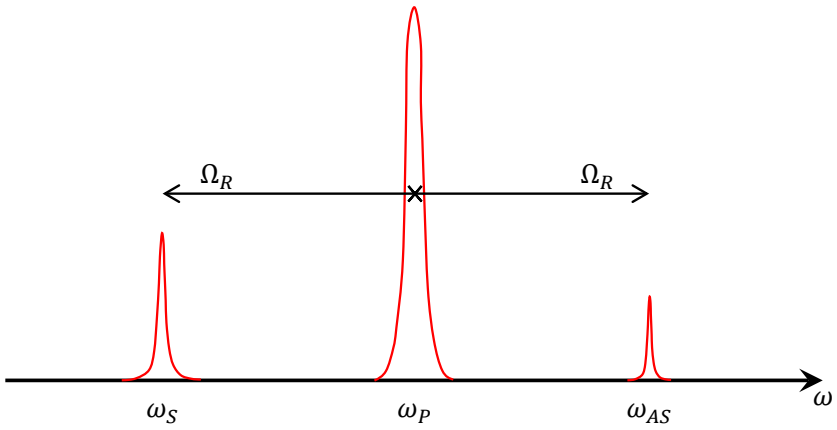

Figure 1.5: Scattered Raman light for a molecule having a single vibrational frequency mode Ω_R. The anti-Stokes scattered line is less intense than the Stokes one.

Concerning the Rayleigh line, it serves as an origin to measure the Raman displacements that are defined as the difference between the wave number of the Rayleigh line and that of the scattered light. The Raman displacement associated with a given vibration is therefore independent of the wavelength of the excitation beam. In practice, the Rayleigh line, which is very intense, is removed using a highly dispersive filter or monochromator and most often only Stokes scattering is observed.

1.2.3 Spontaneous Raman conventional technology

After having quickly described the theoretical principles of spontaneous Raman scattering, the knowledge of the experimental implementation of the process will allow to have a better overview. Thus, typically, in a conventional Raman imaging optical system, there is first a laser beam focused on a sample. Raman scattering is then collected and spectrally dispersed on an array detector - for each spatial position of the sample (Fig. 1.6). The essential components of a classical Raman system involve:

In the excitation path

(1) A light excitation source, usually a continuous wave laser, (2) a microscope and an with (ideally) a large numerical aperture (NA) to detect as much scattered light as possible, and (3) a scanning system, which scans the excitation beam (galvanometer mirrors or xy table). Or the sample itself (*e.g.* with a piezo-electric stage).

In the detection path

(1) Filters that separate Raman scattered light from the excitation beam and Rayleigh scattered light. (dichroic mirror, notch filter), (2) a confocal slit or pinhole, (3) a diffractive component such as a prism or grating followed by a confocal system and (4) an array of detectors, such as a charged couple device (CCD) or an electron multiplying charged couple device (EMCCD).

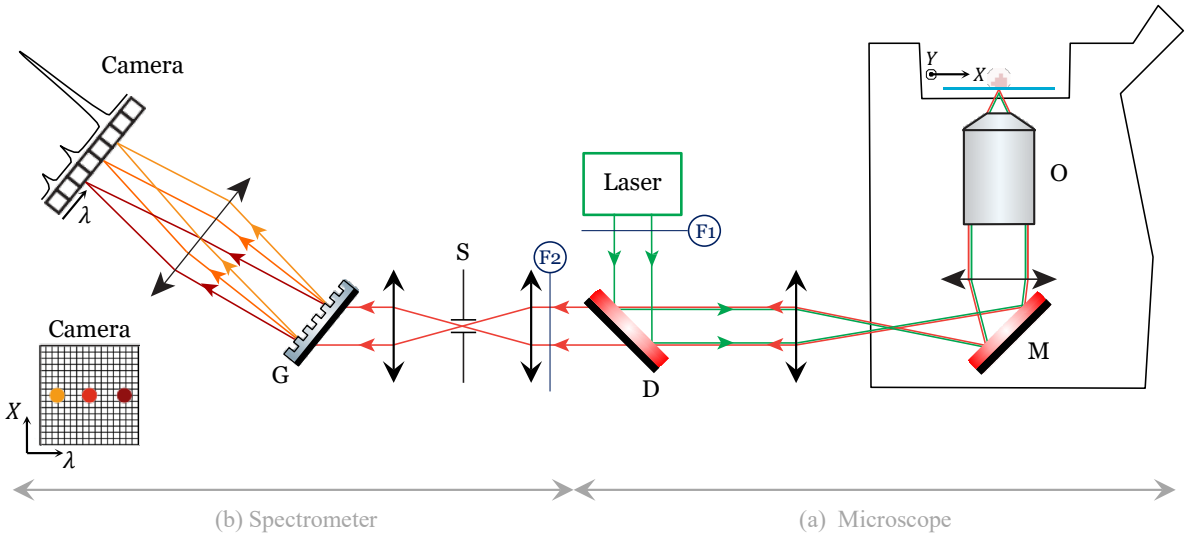

Figure 1.6: Conventional setup for Raman imaging **(a)** the microscope where a laser beam is focused is imaged on the sample. Raman scattered light is collected and filtered by **(b)** a spectrometer and confocal element (slit). The Raman light frequency components are dispersed by a grating on a camera. The scanning of the laser beam (or of the sample) in x and y, which can be ensured by galvanometric mirrors or a stage *e.g.*, leads to an image through raster scan reconstruction. O: lens, M: mirror, D: dichroic mirror, S: slit, G: grating, F1: laser line filter, F2: notch filter.

1.2.4 Limits

Each band of a Raman spectrum represents the interaction of incident light with certain atomic vibrations. Therefore, the atomic vibrations, in turn, are controlled by the sizes and masses of the atomic species of which the sample is composed, the bond strengths between these atoms and the symmetry of their arrangement in the molecular structure. These factors affect not only the frequencies of the atomic vibrations and the observed Raman shifts, but also the number of Raman bands observed, their relative intensities, their widths and their polarization. Therefore, Raman spectra are very specific for a certain type of sample and can be used for identification and structural characterization of unknowns [41].
This is how Raman spectroscopy technique offers high chemical selectivity with optical resolution in label free imaging. This method uses, as said above, the intrinsic imprint of the vibrational spectrum of molecules that can be considered as a "barcode" for them, each species having a unique set of amplitudes and frequencies. This is why, by reading a vibration spectrum, one can identify quantitatively and qualitatively the chemical species present. A key advantage of confocal Raman microscopy is that it uses excitation and detection wavelengths in the visible or near IR, thus providing high spatial resolution microscopy capabilities on the order of hundreds of nanometers. On the other hand, despite its low cost on the market and the higher signal levels, conventional vibrational spectroscopy uses the absorption of IR radiation which, due to its longer wavelength (ranging from 2.5 μm at 25 μm), does not provide high resolution microscopy (a few micrometers only) and cannot be operated in water.

Raman and IR cross-sections

Spontaneous Raman imaging is an appropriate candidate for chemical imaging of biological samples. In practice, the Raman scattering efficiency process is nevertheless extremely low (only of the order of 10^{-6} of the incident intensity is converted into a signal) and leads to low signal levels (especially in endogenous compounds) and long integration times [9], [10]. This is a limiting factor for applications. The Raman scattering cross sections are of the order of 10^{-30} cm^2 per molecule (10^{-11} less efficient than IR absorption) whereas a fluorescent absorption cross section with 1 photon can reach 10^{-16} cm^2 [42].

Acquisition time

Therefore, to obtain an appropriate Raman spectrum, it is necessary to integrate several tens or hundreds of milliseconds for each pixel, which means that a single image can take from a few minutes to several hours to acquire.
But this long acquisition time is not only due to the low Raman cross section. It is also caused by the detection method itself. The system uses, as demonstrated in the previous part in 1.1.2.2, a grating combined with a detector array which makes possible to capture a whole Raman spectrum on the camera at once. This detection scheme divides the total Raman signal onto different camera pixels. This can

lead to a very limited stream affecting each camera pixel and data storage management [43]. These sensitive multi-pixel cameras of the CCD or even EMCCD type are necessary in order to compensate for the weak spontaneous Raman effect. Such cameras, which are then expensive, limit dynamic applications where fast imaging is required, due to slow reading speed and associated electronic noise [44]. This part is very well illustrated in Scotté's thesis (2020) by the well-detailed appendix B.1 [23].
Commercially available camera capabilities can best record a spectrum in 10 ms for CCD cameras (with associated high readout noise) and 760 μs using less than 10 lines along the x-axis for EMCCDs [45] [46]. This acquisition time therefore makes "live dynamic process" imaging impossible with such a technique. For example, in biology, nothing is really fixed in a medium that we observe; due to the inherent motion of organelles, or such as the simple contraction of a muscle, bio-imaging must often be faster than any motion artifact. The acceleration of Raman imaging is therefore essential to its evolution.

Background signal

The problem of fluorescence sometimes arises. The Raman effect is different from that of fluorescence since it is a scattering process: Raman is scattering, fluorescence is not, but both are incoherent. Fluorescence occurs when the frequency of the incident radiation makes it possible to reach an excited electronic level of the molecule, as may be the case during the analysis of organic materials *e.g.*, which brings the system into an excited state. After a certain time (fluorescence lifetime), the system relaxes to its at lower energy levels thanks to the emission of photons very often masking the Raman signal [10]. Essentially, the result of both processes is the same: a photon with a different frequency than the incident photon is emitted and the molecule is brought to a lower energy level. However, the difference is that Raman scattering can occur at any frequency of incident light. Unlike fluorescence, Raman scattering is not an electronic resonant effect except in the case of resonant Raman spectroscopy [47]. This means that the wavelength of a Raman peak will change according to the excitation wavelength, whereas a much broader fluorescence peak is linked to a specific frequency and will therefore be insensitive to the excitation wavelength [48].
It is possible overcome this fluorescence background phenomenon by using excitation wavelengths that are less energetic such as 1064 nm, in the near IR. The drawback is a decrease of the Raman signal being proportional to $1/\lambda^4$, that must be compensated by a higher laser excitation power or longer integration time [39]. Another method would be to look at the lifetime of these two phenomena. Given that the lifetime of the florescence emission is longer (a few nanoseconds) than that of the Raman scattering (a few picoseconds), it is possible to use time gating and temporal filtering to detect the Raman photons just after (few hundreds of ps) the arrival of the excitation pulse [49] [50] [51]. Further background information is detailed on which methods can be employed for fluorescence suppression purposes in Raman spectroscopy in the article by W. Dong in 2015 [48].

1.3 Improvement of spontaneous Raman spectrometry

Despite its relatively low cost, the spontaneous Raman effect nevertheless leads to long acquisition times for a single image, from a few minutes to several hours. In addition, in biology, if organelles of a cell are not fixed in one way or another, the images can show significant artefacts [52].
In this thesis, we will only consider spontaneous Raman. Nevertheless, it is necessary to mention briefly nonlinear optical approaches as another possible solution to speed up Raman imaging.

1.3.1 Nonlinear optical technique: CARS and SRS

By using nonlinear optics, It is possible to excite coherently the vibrational modes and to increase the Raman signal by several orders of magnitude [11].

Thus, complementary nonlinear optical techniques have been developed such as coherent Raman scattering. Unlike the phenomenon of spontaneous Raman scattering, coherent Raman scattering microscopies - with the two most popular versions being stimulated Raman scattering (SRS) and coherent anti-Stokes Raman scattering (CARS) - have shown the ability to access fast imaging (with a pixel dwell time down to 1 μs). Thus allowing live, label free imaging of biochemical components in cells. Nonlinear optical phenomena were made possible by the invention of the laser in 1960, even though the first predictions of these phenomena are dated 1930s [53] [54]. The first experiment of nonlinear optics was made in 1961 (generation of second harmonic) and starting from 1965, most of the effects of nonlinear optics were explained theoretically including, among them, the coherent Raman process [55] and stimulated Raman scattering (SRS) more specifically, in a ruby laser study [56].
CARS and SRS conventional implementation uses two laser beam: a pump beams with an angular frequency ω_P, and a Stokes beam with ω_S. The beat frequency of the two lasers pulses reaching simultaneously the sample is $\Omega = \omega_P - \omega_S$ and can cause the molecules to oscillate at this beat frequency Ω_R if $\Omega_R = \omega_P - \omega_S$. It is this resonant and coherent process which makes possible to obtain an enhancement factor of 10^7 as compared to spontaneous Raman scattering [57]. A notable example is the real-time imaging of lipid droplets in living cells [58] [59].

CARS

Since its revival in microscopy in 1999 [60] [61], the CARS method has become a leading vibrational imaging tool in biological medicine [62] [63]. To explain it briefly, CARS is a four-wave mixing process that generates a new field blue-shifted from the pump and Stokes frequencies, called the anti-Stokes

field at frequency $\omega_{AS} = 2\omega_P - \omega_S$ and a red-shifted field called coherent-Stokes scattering (CSRS) at frequency $\omega_{CSRS} = 2\omega_S - \omega_P$. These anti-Stokes photons (blue-shifted) are more easily detected in the presence of single-photon fluorescence [64]. Figure 1.7 gives a spectral view of the CARS process. When the energy difference between the pump and Stokes photons corresponds to a molecular vibration of the sample, the scattering process is amplified coherently. Rodriguez's review article can provide more in-depth detail on the CARS process [65].

CARS microscopy is relevant for many areas of research such as imaging of living cells [62] [64], skeletal stem cells [66], tracing of toxic nanomaterials in biological tissues [67], monitoring of organelle transport in living cells [59], detection of brain tumors [68], volumetric imaging of human somatic cell division [69] etc. A comprehensive review can be found in [11].

SRS

The SRS process splits in two processes now as stimulated Raman gain (SRG) and stimulated Raman loss (SRL). Unlike the CARS process, the SRS signal is generated at the same frequencies as the incoming pump and Stokes beams and manifest itself as the SRL and SRG signals [57]. At the resonance $\Omega = \Omega_R$, where Ω_R is the vibrational frequency of the molecule, the intensity of the pump undergoes a depletion (SRL), while the Stokes field experiences a gain (SRG) [22]. A detailed description of the SRS process can be found in review articles by Hellwarth [70] and Shen and Bloembergen [71].

SRS has been successfully applied to imaging of biomolecules in food products [72], atomic interferometry [73], plasma physics [74], chemical imaging inside cells [75], bulk and nanoscale specimens [76] etc. A comprehensive review of the SRS process can be found in [77].

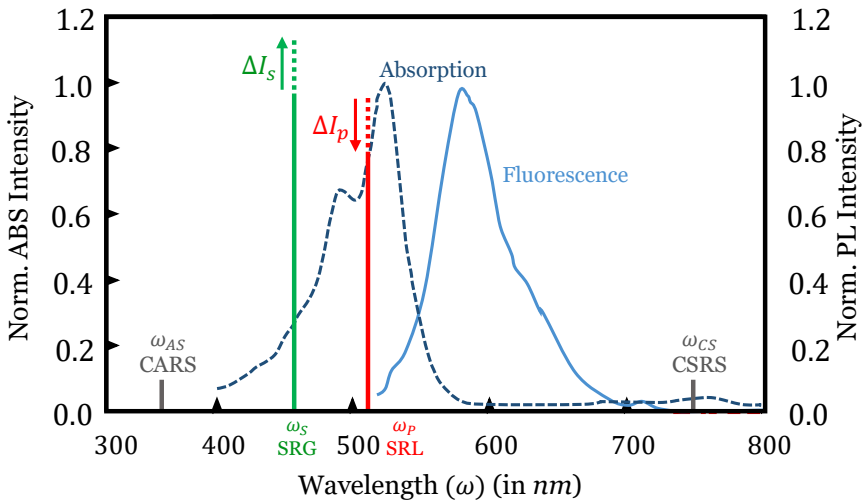

Figure 1.7: Spectral domain view of coherent Raman scattering, induced by two laser beams at frequencies ω_S and ω_P, with different absorption and fluorescence intensities. Different from the CARS and CSRS processes (in grey) which generated new frequencies, the SRL (in red) and SRG (in green) processes result in a loss of intensity ΔI_P on the pump beam and a gain in intensity ΔI_S on the Stokes beam, respectively. The process of absorption and fluorescence (linear emission mechanism) are also shown in dark blue and light blue, respectively.

However, CARS and SRS use complicated and expensive laser sources that limit their broad dissemination over the scientific and industrial communities. Another problem is that coherent Raman imaging usually focuses on small spectral regions if not a single Raman line, therefore, it does not fully address the complexity of the vibration spectrum "barcode". Recent efforts have advanced this limited spectral window issue [78].

1.3.2 A linear alternative approach: Compressive Raman technology

Regardless of the method used, to be effective in real-world applications, spectral imaging must overcome a major challenge: data throughput. This is even more true when we talk about the Raman effect. Given the available data bit rate in computer, it is still difficult to process useful multi-spectral information in real time. Nevertheless, the speeds at which spontaneous Raman spectral information can be obtained can be increased by using different detection strategies.
Compressive Raman imaging is one of these detection strategies, that minimises the measurement time and the post-processing required by conventional Raman. Meaning that this new technology allows researchers to speed up the measurement process and simultaneously simplify data analysis. This method is the main object of this thesis as we will detail in chapter 2.

1.4 Conclusion

In this first chapter, we demonstrated the Raman optical contrast used throughout this thesis. A relatively simple theoretical description helped to understand some important properties of spontaneous Raman scattering. This efficient and “label free” process is able to address the molecular fingerprint as a “molecule bar code” in order to identify different chemical species. The instrumentation needed to obtain a Raman image is simply a focused laser beam that spatially scans the sample and a dispersive element that scatters the spectrum on a camera. We showed that the poor efficiency of Raman spectroscopy and its long acquisition time are inherent to the low Raman scattering cross section but also to its technical implementation, *i.e.* using cameras. These long acquisition times limit the implementation of spontaneous Raman imaging to slow dynamics. These limitations have motivated the development of new technological approaches and in particular the “compressive Raman technology” that appears as an appealing alternative.

Chapter 2

Compressive Raman technology

Contents

In this chapter, the main principles of compressive Raman technology (CRT) will be presented. Simple descriptions accompanied by visual aspects will be adopted to explain the different concepts on which the compressive method is based.

In the first part of this chapter, CRT basics will be presented. A comparison of conventional and compressive spectrometers will be presented.

Our experimental implementation of CRT, oriented for application, will be presented with its different components and the key roles they have. At the end of this chapter, we will conclude with a simple application example which provides further information and allows to get a complete idea of how to apply CRT.

2.1 Introduction to compressive Raman

2.1.1 Basics

To understand why the compressive Raman imaging framework enables a simpler and faster workflow, the notion of hypersctral data cube, but also two other distinct concepts need to be explained: compressive sensing and single pixel imaging.

Hyperspectral Data Cube

We saw in 1.2.3 that a conventional Raman imaging optical system requires (i) a light source focused on a sample and (ii) a spectrometer where Raman scattering is then collected and spectrally dispersed on an array detector. If the sample needs to be imaged, the microscope will combined with a beam scanning mechanism that raster scan the beam across the sample and collects, for each pixel the Raman spectrum.

The combination of Raman spectroscopy and microscopy is called "Raman Hyperspectral Imaging" [79]. This combination associates a Raman spectrum to each spatial pixel of the sample. Thus, a so-called "hyperspectral" data cube can be used to represent the signals collected from the system (Fig. 2.1 – represented here for the reflectance case).

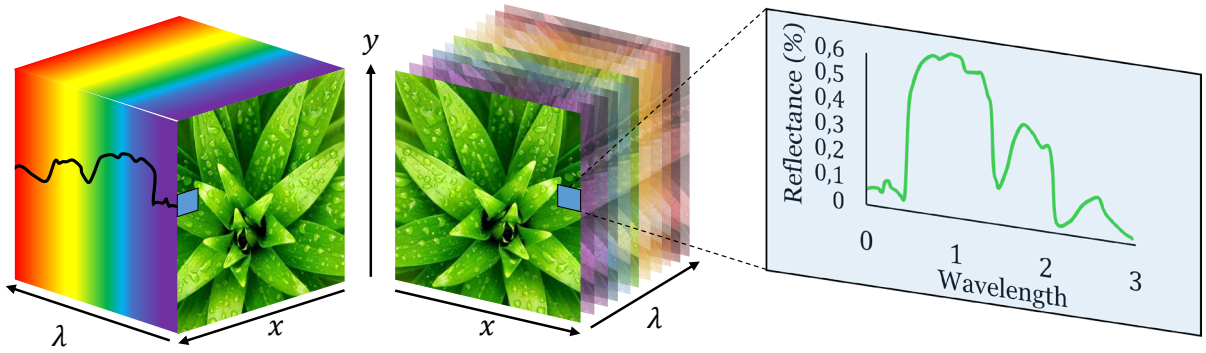

Figure 2.1: Representation of a reflectance hyperspectral data cube of green leaf seen in two different illustration method. On the left side a hyperspectral cube with its pixel represented in blue associated with its given spectrum on λ. On the right side, a sub-image stack forming a 3D hypercube and the reflectance spectrum associated with a particular pixel in blue.

By definition, hyperspectral imaging exhibits the spectral content of the scene and imaged objects. For each spatial position imaged, it provides a large number of spectral bands (hence the term "hyperspectral"), comparable to that of a spectrometer. Since each spatial position is associated with a spectral content, we naturally represent the hyperspectral data using a cube, with 2 spatial dimensions (x, y axes) and 1 spectral dimension (λ). As shown in the figure 2.1, these data can be seen as a large number of images of the scene that contain the reflectance of visible and infrared light broken down into tens or hundreds of spectral bands or as a set of spectra at each spatial position [79].

The growing interest in hyperspectral imaging is linked to the wealth of data it contains. Compared to monochromatic (in grayscale) and color (known as "RGB") images where objects are represented on 1 and 3 spectral bands respectively, hyperspectral imaging gives access for each pixel to a full spectrum, discretized over several tens or even hundreds of values. This fineness of spectral information gives hyperspectral imaging a much greater ability to analyze scenes than black & white or color imaging [80]. By giving access to the spectrum, it is possible to identify the sample nature very accurately – the term "spectral signature" illustrates this capacity for identification [81] [82].

Nevertheless, the intrinsic three-dimensional structure of hyperspectral images induce two main constraints: (i) a hyperspectral image contains a large number of data, (ii) imaging technologies rely on two-dimensional sensors, which can therefore only perceive a projection of the hyperspectral cube. The size of hyperspectral images can reach several hundred of megabytes for spatially and spectrally well-resolved data [83]. This raises storage, transmission and above all processing difficulties, which add to the poor efficiency of spontaneous Raman scattering as mentioned in 1.2.4. For these reasons, only few on-board systems use hyperspectral data in real time. In this chapter, we aim to explore which solution(s) the compressive Raman methodology can bring in order to acquire these data in a faster and more efficient way.

Compressive sensing (CS)

As we have understood, the data processing, is the area that must be optimized. Once detected, these high levels of quantitative information must be processed quickly and efficiently.

A majority of in-situ microscopy video captures are performed with charge-coupled device cameras (CCD). The use of these cameras made it possible to acquire the entire image in a single measurement thanks to a matrix of pixels similar to that of a digital camera. These devices are based on the charge transfer mechanism. It allows to transfer the photoelectrons of each pixel to a single analog/digital converter; This allows to digitise the entire image with a reading rates in the range of a few tens of MB/s [84]. Despite significant progress made with the introduction of CCD direct detection cameras: which dramatically increase the magnitude of the readout rate (less than ms to capture a full frame), improvement in temporal readout and reduction in the use of electrons [85] [86] data transfer remains limited. Data transfer therefore becomes the main challenge to overcome compared to that of electron detection.

Compressive sensing (CS) is a signal processing technique which allows one to efficiently acquire and reconstruct a signal. This was highlighted in Candès *et al.* and Donoho, in 2006 in [87] [88]. CS combines detection and compression in a single operation and could still have the potential to improve the temporal resolution of all detectors [86]. Conventionally, the signal sampling frequency for lossless data acquisition is given by the *Nyquist-Shannon* theorem which states that to accurately reconstruct a band-limited signal, it must be sampled at a frequency at least twice the frequency higher present. That is, to solve a spectral feature with a bandwidth d_ω in a spectral interval D_ω one requires $P_w = D_\omega / d_\omega$

spectral samples. In addition, spectral imaging requires $P_w \times P_s$ total samples (P_s = the number of spatial pixels). CS uses computationally efficient algorithms to increase the data acquisition speed. The way it works is as follow : CS manages to design a non-adaptive detection scheme to measure signals in basis that makes the signal must be sparse in some basics, effectively reducing the number of measurements below the Nyquist-Shannon theorem [86] [89]. This is possible in an unsupervised way, *i.e.* with little prior knowledge of the sample studied. CS measures with M filters to retrieve N information ($M < N$) if the information is sparse in a certain basis.

In other words, CS makes possible to directly capture a representation of an image with a small dimension. This, in order to obtain a considerable under-sampling of the signal by using post-acquisition reconstruction algorithms [79] as it has been done in the fields of magnetic resonance imaging [90] and radar imaging [91] [92]. Also, regarding the many real-life datasets that may be sparse (some spectral or spatial features are essentially zero value or redundant), the development of a wider range of imagery would not necessary provide more spectroscopic detail [79].

Single pixel image

CS is largely based on a process called "multiplexed measurement" [93]. In multiplex measurement, the signal is mixed, detected by a multi-channel or even single-channel sensor, and not mixed by calculation. This framework is called "single pixel imaging" because it requires only one light-sensitive detector more commonly called "single pixel detector" (SPD) (Fig. 2.2).

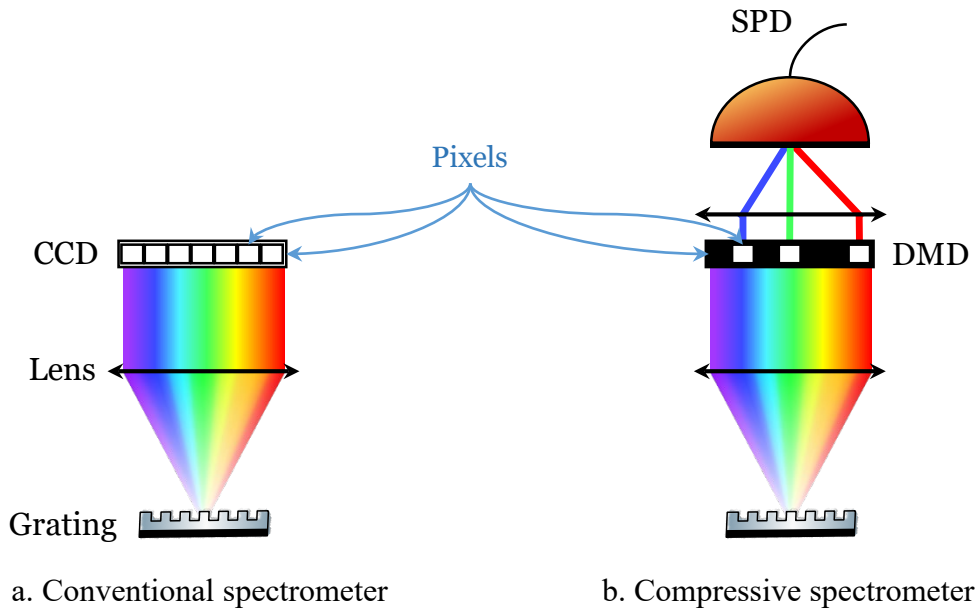

Figure 2.2: Comparison between **(a)** conventional and **(b)** compressive spectrometers. In compressive spectrometers, the CCD camera is replaced by a digital micromirror device (DMD) combined with a single pixel detector (SPD).

This association (DMD + SPD) offers a cheaper alternative (that represents a competitive advantage) over conventional cameras (multi-pixel counterpart) [43].

By definition, and basically, a single-pixel camera performs a type of scanning that can take many forms. With its single pixel, this camera weakly detects intensity information from many locations at once. This approach, compared to traditional point scanning-based methods, offers different advantages among which its ability to retrieve multipixel images faster [93]. Moreover, it can offer better performance, such as faster temporal response, improved detection efficiency, or even lower dark counts. Such advances may be of importance in situations where detected intensities are very low due to scattering or absorption losses, *e.g*. medical imaging or long-range 3D imaging [93] [43]. This is because the single pixel detector collects signal coming from a large number of points that would be address sequentially in conventional approaches.

Finally, single pixel camera is able to perform a compressive detection directly at the data acquisition stage. Hence, it is able to reduce storage and data transfer requirements in an optimized way. This is an important point concerning remote sensing studies or even, and especially, when the problem is of large dimension such as hyperspectral imaging [79] [94].

2.1.2 Origin and background of compressive Raman

Compressive Raman imaging was implemented for the first time at Prudue University by the work of Wilcox *et al.* in 2013, concerning supervised imaging [95]. Indeed, unlike CS which measures the image with M random filters to find the N information ($M < N$), compressive Raman implies a solid prior knowledge of the system under study and thus uses filters adapted to that prior spectral information. More precisely, in the context of spectroscopic imaging, "supervised imaging" means that the spectra of pure chemicals are known in advance to know whether a chemical is qualitatively or quantitatively present in an unknown mixed solution [96]. This is because each spectrum of a mixture can result from several pure chemical components.

In 2013 Wilcox *et al.* demonstrated that a spectral filter (or multivariate optical element), in this case a DMD, can exploited for estimation of the concentration and chemical compounds in a mixture. In 1995, a DMD was used for first time as a light modulator in a visible spectrometer and revealed with a contrast ratio equivalent to 60:1 [97]. Comparison with the same ratio today, which may be 30 times higher, illustrates the efforts to design a more efficient compressive Raman system. Several approaches to build binary filters for Raman systems involving the use of a DMD have been put forward to date in order to improve the performance of this system. Among them, the binary filters, developed by Scotté *et al.*, is based on maximizing the precision of the estimates of the proportions of the components [19] [18]. Another technique, developed in parallel by Buzzard and Lucier, aims to minimize the error in estimating the photon emission rates of the chemical species studied -OBCD strategy- ; [96] [98]. In this

thesis, we explore applications of this compressive Raman system while maintaining the theoretical approach initiated by Scotté and her collaborators. They used an algorithm statistical estimator using filters design using statistical estimation theory to minimize the Cramer-Rao lower bound to optimize the precision of concentration estimation of known chemical species with binary spectral filters which will be detailed later in this chapter [19].

2.1.3 Compressive Raman spectrometer

With a conventional Raman spectrometer (Fig. 2.3(a)), where classically a laser scans the sample and a CDD camera receives the entire Raman signal, the result is a hyperspectral data cube where each pixel (in x and y) contains a spectrum (in λ). In this case, each spectrum can result from the mixture of several pure chemical components. The entire Raman signal measured requires a long and complex post-processing step in order to sort the information assumed to be linear mixture and estimate the proportions of each chemical product, for each pixels [95] [18] [23].

Compressive Raman technology (CRT) belongs to the field of supervised imaging, *i.e.* the chemical species present within a sample are known *a priori*. The basic idea is as follow: if one measures the pure spectra of the complex mixture beforehand, one can estimate the unknown relative proportions of each species within the mixture.

In this case, a conventional spectrometer can be modified. The camera is replaced by a combination of a spectral filter and an SPD. These two elements make it possible to realize an optical scalar product in the spectral domain: the spectrally dispersed signal is filtered and summed on a SPD (Fig. 2.3(b)). This combination of spectral filter and SPD form the compressive Raman spectrometer and allow the signal to be directly spectrally filtered during the measurement. This directly provides the desired chemical information which can be extracted without recording a full spectrum. In other words, the pixels contained in the hyperspectral data will be identified as a mixture of a priori known pure species. This scheme drastically limits the data follow between the spectrometer and the computer.

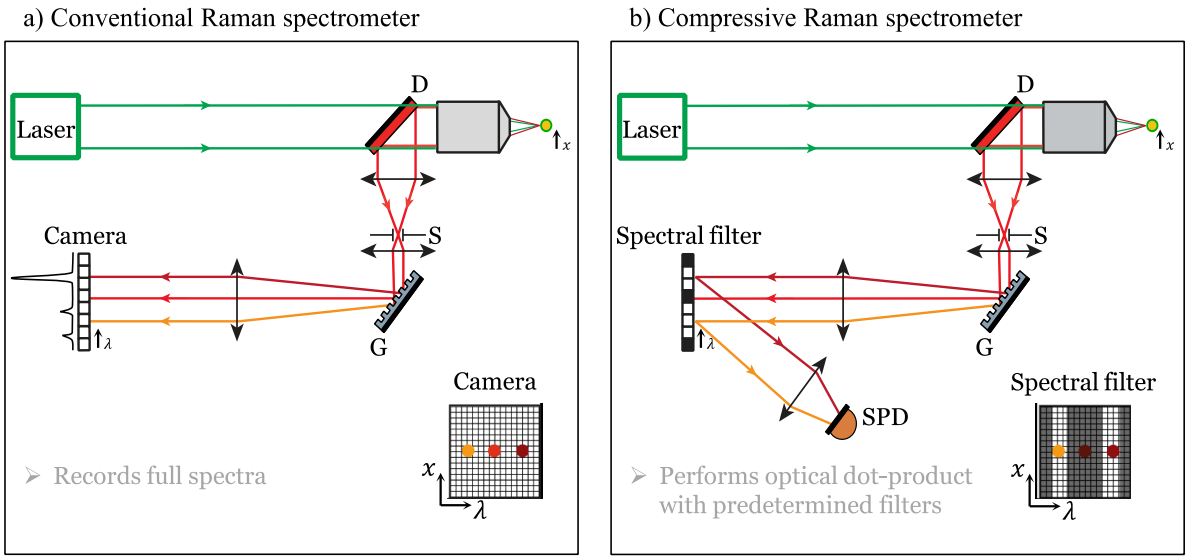

Figure 2.3: **(a)** of a conventional Raman spectrometer and in **(b)** of a compressive Raman spectrometer where the camera is replaced by an SPD combined with a spectral filter. D: dichroic mirror, S: slit, G: grating. While in **(a)** the species proportions are extracted from the Raman spectrum, in **(b)** the optimized spectral filter designs are made possible by the supervised imaging condition. An optical projection is carried out, making possible to extract proportion information without recording a spectrum. Image adapted from Scotté's thesis [23].

Technology potential

At the end of chapter 1, the main limitations of spontaneous Raman scattering and its association with conventional spectrometers have been presented. Regarding CRT, the starting conditions are quite different and the limits need to be redefined.

Indeed, having strong prior knowledge about the system under study allow us to optimize the spectrometer. This is an important consideration on improving the technology for Raman applications. Firstly, regarding the Raman signal, instead of being spectrally dispersed on an array detector (Fig. 2.3(a)), multiple wavelengths are multiplexed on an SPD (Fig. 2.3(b)), this gives more signal. In addition, the data generated are lower in dimensionally and require less post-processing (since most of the processing is done during optical measurement). Added to this is the rate of acquisitions in high signal regime, which is no longer limited by the reading speed of the cameras. Thanks to SPD short reading time (ns), CRT can potentially acquire Raman images at high speed. Last but not least SPD are limited by the quantum noise (shot noise) and achieve a high signal-noise-ratio (SNR) as good scientific cameras do this too compared to cameras.

However, it is important to clarify that the aforementioned advantages of this technology are only attainable after a learning (or calibration) step of the study to which it will be applied. *E.i.* once the spectral filters have been defined to optimize the acquisition. This is why compressive Raman is most useful for chemical analysis when a study involves several experiments with the same type of chemicals. Under optimal conditions, all these advantages, and in particular the increase in acquisition speed, can allow CRT to be used in fields such as in vivo imaging or to follow dynamic processes (For both

scientific and industry applications). It is an emerging imaging method already in the fields of chemistry [99] or more specifically pharmaceuticals [100] [101].
In this context, our aim is to apply this new CRT. In a way, we will prove the efficiency gain of the Raman spectrometer but also its ability to adapt to different problems and conditions allowing us to optimize the measurement time.
In the following part, the experimental scheme used for our measurements is detailed. The calibration of each element participating in the design of the compressive spectrometer, as well as the method of construction of our optimal filters, will be detailed in order to better understand the approach adopted during the application processes.

2.2 Experimental condition

Our motivation to use CRT has focused on biomedical and ecology studies such as the rapid analysis and identification polymorph and other substrates in pharmaceutical tablets, or microplastics. We described here the different elements used in CRT to make the technology functional. This thesis follows the work carried out by C. Scotté in 2018 [23].

2.2.1 Setup requirements and specifications

One of the main questions when choosing the most suitable Raman system is to determine what is the most suitable wavelength for the laser to be integrated into the equipment.
The Raman signal (the specific position of the peaks observed on the Raman spectrum of a material) is only dependent on the chemical structure of the material and is independent of the excitation wavelength. The Raman "spectral signature" will therefore not change depending on the choice of the wavelength of the laser used. However, each excitation wavelength has advantages and disadvantages for a given application and it is essential to choose the most suitable laser to optimize the measurements.
The most important difference is related to the excitation efficiency. The Raman scattering signal is proportional to λ^{-4}, where λ is the wavelength of the excitation laser. For example, Raman scattering at 532 nm is 4.7 times greater than at 785 nm and 16 times greater than at 1064 nm [102]. Therefore, at first sight the shorter laser wavelength is always the better option. Nevertheless, as we have already explained, the main challenge of Raman spectroscopy is its relatively weak signal strength compared to fluorescence, and most complex molecules exhibit autofluorescence when excited with ultraviolet light and/or visible. As a result, most organic and biological samples must be excited in the near infrared (NIR) to prevent the Raman signal from being drowned out by the fluorescence background. The strange

dichotomy created by these competing effects, where a decrease in wavelength will produce greater signal intensity while increasing background noise (autofluorescence) is the most important factor that explains the multiplicity of laser wavelengths used in Raman spectroscopy.
An excitation wavelength in the NIR is an often a good compromise. A standard wavelength of 785 nm was thus selected providing a Stokes-shifted Raman signal between about 800 nm and 1 μm. This corresponds to a low absorption spectral region [103].
Another advantage of being at this standard wavelength is that we can use a silicon-based detector allowing to stay in the shot-noise limited regime. For this same reason, we ruled out the possibility of a longer excitation wavelength (classically 1064nm) because silicon has no response above 1.1 μm. The use of a sensitive detector in the near infrared, generally an array of Indium gallium arsenide (InGaAs), will be necessary for dispersive instruments. In addition, in order to limit costs, the InGaAs arrays generally used have 512 pixels (vs. 2048 for most silicon detector-based systems). This leads to lower spectral resolution and/or a narrower measurement range in terms of the Raman shift. The 785 nm wavelength therefore presents for us the best signal / fluorescence / spectral resolution compromise and the widest range of applications (about 3000 Raman shift wavenumbers).
Overall, the CRT instrumentation is composed of optimized optical elements (to maximize the throughput of the instrument) since Raman applications generally exhibit few photons. A commercial microscope is included in the system. Regarding the scanning method over the x and y axes, it is based on the combination of galvanometric mirrors and scanning lenses which can achieve precision scanning down to about 1 μs per pixel. A stage combined with the microscope also ensures the scanning on these same axes in order to be able to make an assembly of several fields of view (mosaic) of the sample adjacent with each other.

2.2.2 Setup description

The experimental scheme is shown below in Figure 2.4. Two parts can be distinguished. The first part is the microscope and it is located the right side of the diagram. The excitation source comes from a continuous wave laser at 785 nm. This laser excitation source is scanned on the x and y axes of the sample using a system combining galvanometric mirrors (GM) and scanning lenses (L2). Once in the microscope, the laser beam is redirected by a prism (P) towards a tube lens (L1) and an objective (O) to focus the light and activate the Raman contrast. Once the backscattered Raman signal is collected from the sample, it travels back the same optical path to reach the entrance of the spectrometer where there is a confocal slit (S) to reject some of the out-of-focus light and provide spectral resolution. The system combining a dichroic mirror (D) and a notch filter ensures that only the Raman signal is retained at the spectrometer input.

The spectrometer represents the second part of our configuration. It is located on the left hand side in figure 2.4. After reaching the confocal slit, the grating (G) spatially disperses the different Raman wavelengths. The digital micromirror device (DMD) then filters these different wavelengths. Then, the spectral components selected by the "ON" segments of the DMD emerge. They are spatially recombined using a second grating positioned in negative dispersion, thus cancelling the dispersion of the first grating. Under these conditions, the signal can be collected on the small active area of a single photon avalanche photodiode (SPAD).

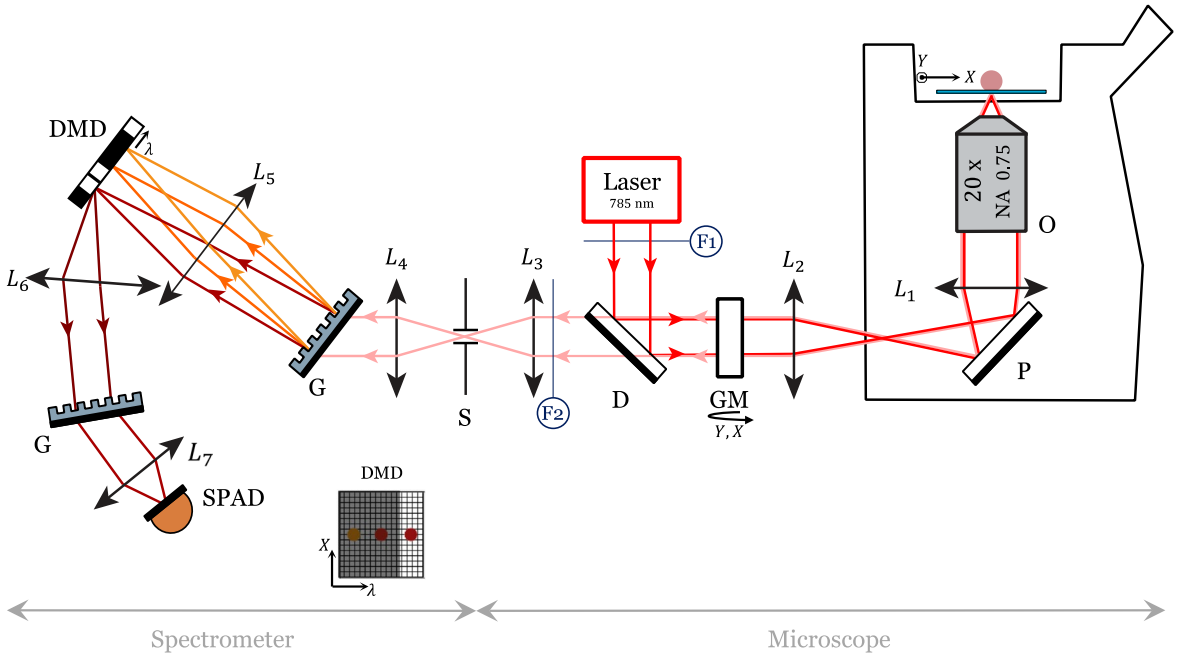

Figure 2.4: CRT experimental setup, built around a commercial microscope. O: objective, P: prism, GM: galvanometric mirrors, D: dichroic mirror, S: slit, G: grating, DMD: digital micromirror device: SPAD: single-photon avalanche photodiode, F1: laser line filter, F2: notch filter. L1: tube lens (200 mm), L2: scanning lens (50 mm), L3 − L7: achromatic doublets of focal lengths 100, 125, 100, 100, 75 mm, respectively. Illustration adapted from Scotté's thesis [23].

Laser

In our configuration, the light excitation source that was selected is a laser diode module (L2K0785SD0090B-IS-TH-L - IPS). This laser operates at a wavelength of 785 nm with an output power of 100 mW (with a possible power variation of less than 1%). This power is fixed at 60 mW at the sample level.

Both robustness and stability (vibrations, temperature changes, etc.) were adapted to the conditions required by the conditions of Raman spectroscopy. A laser line filter integrated into the latter makes it possible to reduces the bandwidth down to 0.3 cm^{-1}. Polarized vertically, this laser beam has only one spatial mode [104]. The diameter of the laser spot is 1.5 mm and the quality of the laser beam is poor with a shape that is close to a square. Finally, the laser is attached to a controller module of the same brand (L-type Controller module) [105].

Scanning system

The scanning system combined a pair of galvanometric mirrors (GM) and a scanning lens. These two elements allow scanning over the x and y axes of the sample. A program (Labview in our case) controls the pair of silver galvanometric mirrors (Cambridge Technology) so that their positioning is constantly of high precision. They are conjugated with the back focal plane of the objective with a four magnification. The GM image of is reimaged at the back focal plane of the objective. This will be detailed in the next paragraph.

Scanning lens (L2) are a pair of achromatic of 2 inches diameter. They are placed so that their glass crown are face to face, approaching a system similar to that of Plösse [106]. This allows the scanning system to be telecentric. The focal length of this scanning lens is 50 mm so that the field of view (FOV) around 120 μm at the plane of the sample.

Finally, a platform combined with the Nikon microscope (where the sample is deposited) allows us to control the location of the sample (in x and y). The aim is to have several FOVs of the sample and to combine them to obtain a large field of view mosaic image. This platform is connected to a Controller (Tango2: 00-76-125-1802 - TANGO), that can be controlled by the user [107].

Microscope system

A commercial microscope from Nikon (Eclipse TE2000U) is used. A prism (P) redirected the light towards the sample while passing through the objective. The transmission efficiency of this part was found to be 91% and 83% once the tube lens (L1) was added. Figure 2.6, illustrates this transmission efficiency, as well as those of all the other elements making our setup, measured and shaped during the work of Scotté [23].

Objective lens

The objective lens is a Nikon air lens (CFI Plan Apochromat Lambda) with ×20 magnification. Its numerical aperture (NA), is 0.75, and its transmission in the NIR region, greater than 80% between 800 nm and 1000 nm. This is relatively high and this justifies its use in our case.

Notch filter & dichroic mirror

A long-pass filter reflecting the exciting light source (more than 94% for a light of 785 nm) and transmitting the Stokes-shifted Raman signal (more than 93% above 795.2 nm with a sharp transition) was combined to the dichroic mirror (Fig. 2.6).

The system ensuring that only the Raman signal is retained at the entrance of the spectrometer is firstly composed of a dichroic mirror (D) (Semrock – LPD02-785RU) [108].

A holographic notch filter (F2) (HSPF785.0 - Kaiser) of optical density ≥ 6 and with a spectral bandwidth ≤ 10 nm (162 cm^{-1}) was placed at the entrance of the spectrometer, at normal incidence. The goal is to reject most of the remaining excitation and Rayleigh light at 785 nm.

Grating

An optical grating diffracts or transmits (depending on the type) light into several beams of different diffraction or transmission angles. In our case, we use two (identical) transmission grating (T-1200-850s - LightSmythTM) [109]. Their groove density is 1200 mm^{-1} and their transmission efficiency is ≥ 94% for polarization parallel to grating lines. However, this same efficiency decreases drastically for the opposite polarization, leading to an average transmission efficiency of ≈ 85% at 850 nm (Fig 2.6).

The first scattering grating was arranged to be at the same angle of incidence and diffraction at 850 nm (Littrow configuration). This way we should get the highest diffraction efficiency [110]. The second grating was careful placed after DMD in order to correctly cancel the dispersion effect applied by the first grating.

Spectral filter: DMD

Spectral filters, also called "multivariate optical elements", can take the form of interference filters such as a DMD. The latter works as a spatial light modulator (SLM) to direct NIR light, thereby selecting the different wavelengths to be detected and generating high-speed patterns for advanced imaging.

During Scotté's work [23], a DMD (V-7001, Vialux, 0.7" XGA resolution, with V4395 controller board) with a total reflection efficiency of 60% was used. In this thesis, a new DMD (V-650LNIR, Vialux, 0.65" WXGA resolution, with V4395 controller board), whose design is more suitable for NIR light, was installed on our setup. Optically, it is organized in 1280 columns by 800 rows of micro-mirrors. The size of each micro-mirror is 10.8 × 10.8 μm. We bin 10 pixels (mirrors) together, thus having a macropixel size slightly lower than the spectral resolution of the spectrometer. An aluminum coating ensures a reflection efficiency of 85% at the wavelengths of interest [111]. Combining this efficiency with the other losses established previously, the total efficiency of DMD in this window is approximately ≥ 69% (Fig. 2.6).

Each of these micro-mirrors is switchable between two discrete angular positions: – 12° and + 12°. The angular positions are measured relative to a flat state at 0°, which is parallel to the plane of the mirror array. The tilt direction is perpendicular to the hinge axis, which is positioned diagonally to the entire array. Thus, our DMD is arranged so as to have an offset of 45° in our configuration so that the mirrors can correctly diffract the light on one side (ON: towards the detector) or on the other (OFF: towards the absorber). Finally, the DMD is installed

on a mount with adjustment of the x, y and z axes in order to select the wavelength region of interest (λ) and adjust its (x, y) position relative to the focus.

Detector: SPAD

The signal from the DMD is routed through an avalanche photodiode operating in the photons counting mode. The single-photon avalanche diode is a highly sensitive semiconductor electronic device that exploits the photoelectric effect (Figure 2.5) to convert light into electricity. The specificity is its ability to detect signals of very low intensity (down to single photons).

Here we use the single-photon avalanche photodiode (ID120-IDQ) with an active surface diameter of 500 μm and a theoretical quantum efficiency of 80% [112]. This single-photon detection module is based on a silicon avalanche photodiode. Its efficiency value of 75% is reached at 800 nm but decreases drastically to reach 5% at 1050 nm (Fig. 2.6). This drop in efficiency is (simply) explained by our choice of 785 nm excitation wavelength involving our Raman signal at the limit of the sensitive region of silicon-based detectors (between ≈ 800 nm and 1100 nm).

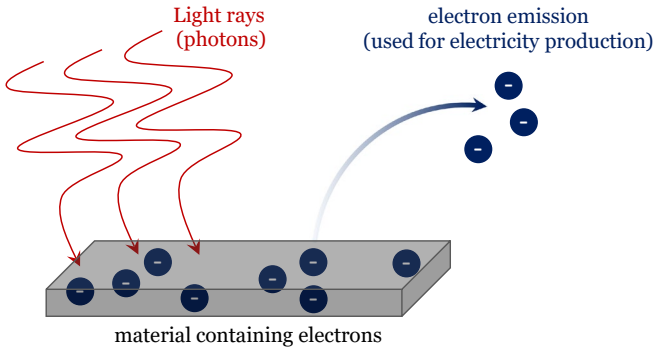

Figure 2.5: Simple illustration of photoelectric effect

System alignment

In order to align the spectrometer at the correct wavelength, which is different from the excitation wavelength, a laser diode operating at 846.8 nm (CPS850 - Thorlabs), falling into the Raman photon detection range, is used for the alignment mimicking a Raman signal of 927 cm^{-1} (in the middle of the fingerprint region).

Finally, in order to allow for a correct alignment and adjust certain characterizations of the setup, the microscope is equipped with a CMOS camera (DCC1545M - Thorlabs) and an NIR LED.

2.2.3 Set up properties

This section illustrates the features of our CRT instrument such as the transmission efficiency of the key elements or their spectral and spatial properties. We will then conclude this chapter by demonstrating our CRT instrument capability on a sample.

Transmission efficiency

Figure 2.6 below illustrates the different efficiency details of each of the elements of our configuration. Thus, this figure represents, from emission to detection, the transmissions of the main optical elements allowing us to detect the Raman signal. Ultimately, all of these different transmissions led our setup to have a maximum Raman signal efficiency of ≥ 18% around 800 nm.

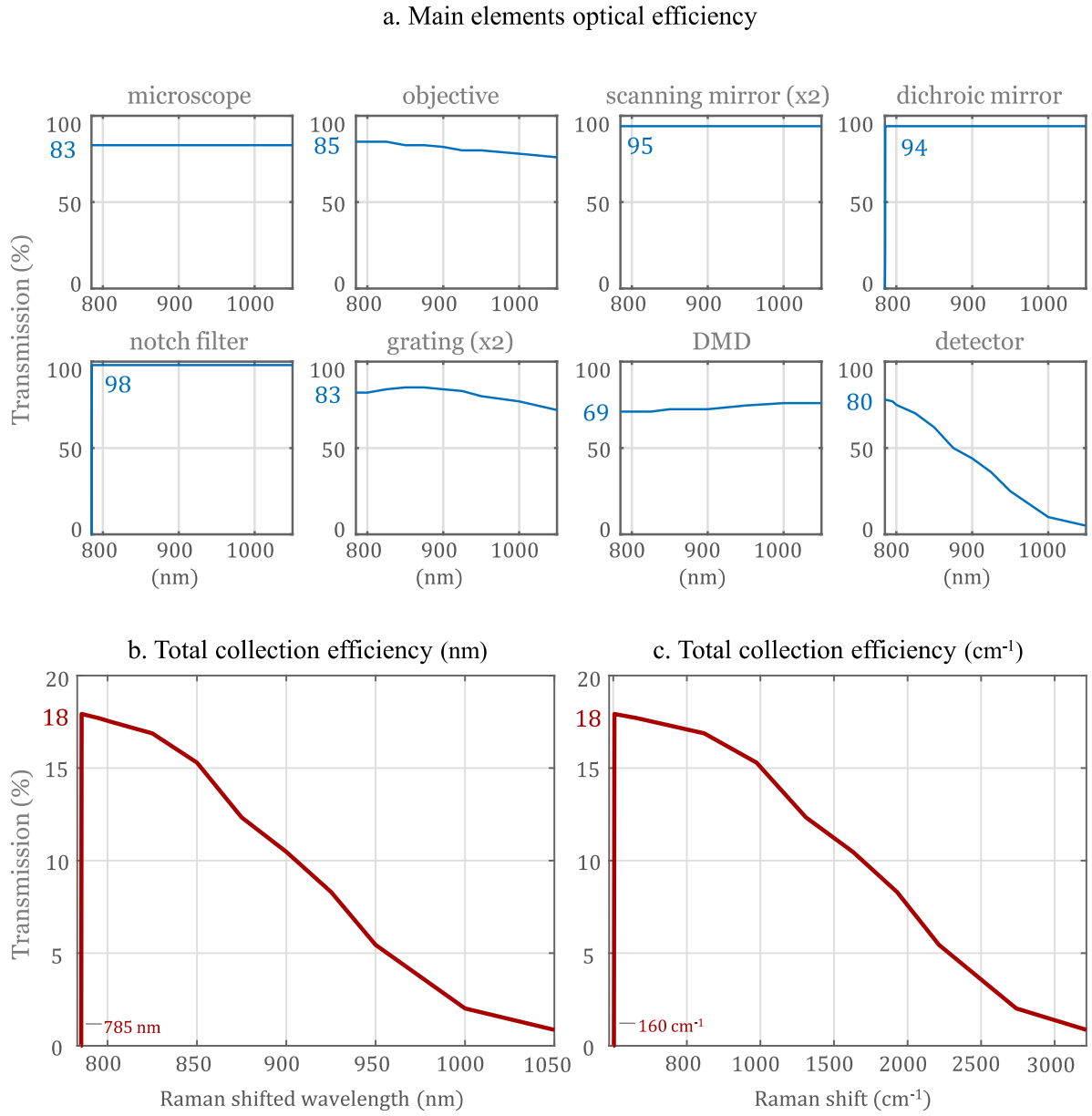

Figure 2.6: **(a)** Transmission of the main assembly elements. "× **2**" is specified when one of the elements of the configuration is crossed twice by the signal. Yields are relatively constant across the spectrum, except for the detector. Simulated total collection efficiency of the Raman signal to **(b)** wavelength (nm) and **(c)** Raman shift (cm^{-1}). Figure adapted from Scotté's thesis **[23]**.

Spectral properties

Spectral resolution is one of the most essential characteristics of a spectrometer. It refers to the bandwidth and sampling rate over which the sensor collects information about the scene. In other words, it determines the maximum number of spectral peaks that can be resolved by the spectrometer over a given frequency range.

The calculation of the latter is specific to the optical configuration used. In our specific case, the calculation of the spectral resolution is be done according to the approach of W. Demtröder [8]. Thus, we have:

$$\delta\lambda = f_5 \left(\frac{\lambda}{a} + \frac{b}{f_4}\right)\left(\frac{\partial}{\partial\lambda}\right)^{-1} \tag{2.1}$$

Where $\delta\lambda$ is the spatial resolution, $f_5$the focal length of the lens of the same name in our configuration, similarly for f_4, a represents the size of our laser beam and b the slit aperture ($\geq$ 100 μm). The second term $\frac{\partial}{\partial\lambda}$ is the linear angular dispersion given by:

$$\frac{\partial}{\partial\lambda} = \frac{f_5}{k.\cos(D)} \tag{2.2}$$

With $k = \frac{1}{l}$, where l is the groove density of the optical grating (1200 cm^{-1}) and $D \approx 30.7°$ which is the diffraction angle at a wavelength of 850 nm. Thus, the inverse linear dispersion $\left(\frac{\partial}{\partial\lambda}\right)^{-1}$ reaches a rounded value estimated at 7.2 nm/mm corresponding approximately to 0.078 nm ($\approx$ 1.08 cm^{-1}) for each mirror of the DMD. By combining the linear dispersion with the first term of equation (2.1), we obtain a spectral resolution $\delta\lambda \approx$ 0.68 nm ($\approx$12 cm^{-1}). As mentioned above in the DMD section, our macropixels, formed by grouping 10 micromirrors on the DMD, have a slightly lower spectral resolution than the spectrometer.

Note that other commercial Raman spectrometers exist with a higher spectral resolution (few cm^{-1}). However, possible improvement would involve modifications of the configuration such as the installation of longer focal length (*i.e.*). By keeping our settings, we keep a good balance with spectral range and compactness.

Spatial properties

The spatial resolution corresponds to a measure of the microscope's ability to resolve the details present in the original specimen, and is related to the quality of the optics, sensor, and electronics in addition to the spatial density (the number of pixels in the digital image).

In our specific case, knowing that how our laser beam enters the back focal plane of our lens allows us to theoretically calculate the point spread function (PSF) of our system $\mathcal{R}$, in (x,y) and (z) with the following relation, but also according to the approach of [113] and well summarized on this website [114]:

$$\mathcal{R}_{x,y} = \frac{\lambda}{2\,[\eta\ \times \sin(\alpha)\,]} \qquad \mathcal{R}_z = \frac{2\lambda}{2\,[\eta\ \times \sin(\alpha)\,]} \tag{2.3}$$

Where λ is the wavelength of the light, η represents the refractive index of the imaging support (or immersion medium) used between the objective and the coverslip protecting the sample ($\eta = 1$ for the air; $\eta = 1.51$ for oil or glass). The combined term $\eta\ \times \sin(\alpha)$ is known as the objective numerical aperture (NA). Thereby:

$$\mathcal{R}_{x,y} = \frac{\lambda}{2\,(NA)} \qquad \mathcal{R}_z = \frac{2\lambda}{2\,(NA)^2} \tag{2.4}$$

We therefore obtain a spatial resolution of the image on the x and y axes of approximately of 1.1 μm. On the z axis, our spatial resolution $\mathcal{R}_z$ is around 1.5 μm.

In order to verify the veracity of this theoretical data, Horiba Scientifique™ provided us with a modulation transfer function (MTF) test pattern acting as a "resolution target" for our Raman configuration. This pattern consists of fine gold patterns on a silicon background. The principle is to be able to image areas where the distances of the lines and spaces between the lines are close to our theoretical spatial resolution on the x and y axes. The images made for this purpose were acquired by designing a spectral filter displayed on the DMD, specific to silicon. This filter only selects the characteristic wavelengths of the silicon raman spectrum, thus rejecting any light reflected by the gold surfaces. This is illustrated in figure 2.7: spacing and line have the same measurements and the distance varies by section. Here we can see four distinct sections where the line/space distances are indicated at the top of the figure: 2 μm, 1.5 μm, 1 μm and 0.5 μm (Figure 2.7 (a)). If we look at the related sections in (b), we very clearly resolve the lines in the 2 and 1.5 μm sections. In the area of the 1 μm lines, the lines are hardly discriminated due to a clear loss of the periodicity of our peaks. Finally, we do not resolve lines in the 0.5 μm area. Thus, our initial estimate of 1.1 μm is confirmed with an experimental trend suggesting that it could be slightly larger.

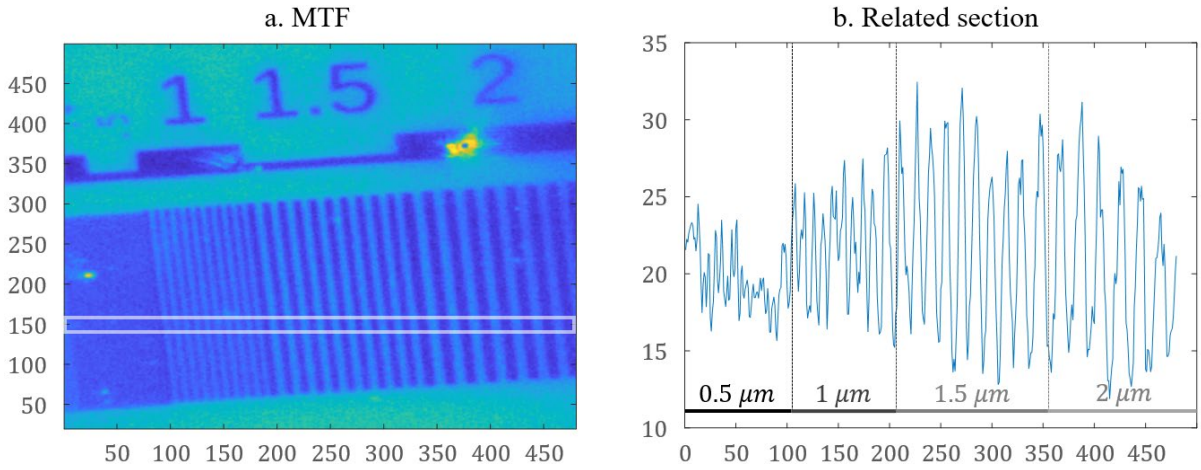

Figure 2.7: Spatial resolution measurement **(a)** image (480 × 480 pixels) of the MTF pattern with different target areas, where spacing width = line width, and **(b)** the section associated with each area.

Regarding our spatial resolution $\mathcal{R}_z$, we gradually varied our objective on the z axis, from a polystyrene ball with a diameter of 1 μm, in order to recover a variable Raman signal on the different scales. Measurements from these data provided us with an experimental $\mathcal{R}_z$ of ≈ 3 μm, which is twice what we expected in theory. The PSF of the microscope governs this and we will assume that our $\mathcal{R}_z \approx 3$ μm.

To finish, a completely homogeneous silicon area is used to estimate our experimental FOV from the Raman signal (Fig. 2.8). The FOV is then evaluated at around 150 μm, which is slightly higher than what was estimated according to our optical configuration in the "scanning system" section. We will however use during all our manipulations a default FOV of 100 μm.

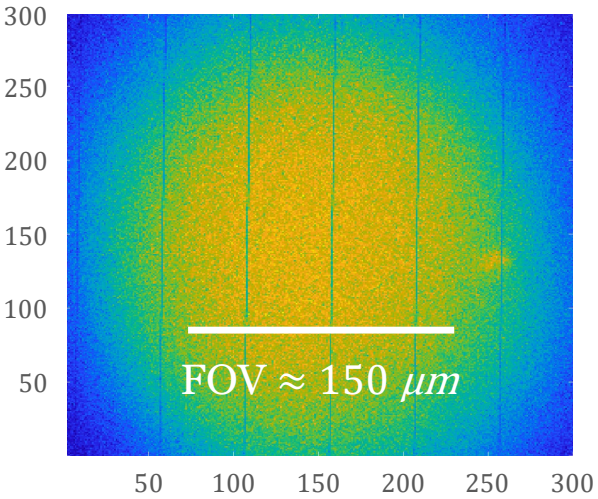

Figure 2.8: FOV estimation via the signal (in yellow) coming from a scanned homogeneous silicon area.

2.2.4 Validation on a test sample

In this section, an applicative example illustrate the concept of CRT. Both the design of optimal filters and the characteristics of the compressive method will be described. This will also allow us to present the mathematical basis on which our results are derived. In this section, we aim to understand the classic experimental analysis schemes used by the CRT that we will find in our following chapters dedicated to specific applications.

Application concept

In order to set up a simple example of the application, CRT images of latex beads are presented. Two different types of beads (Sigma Aldrich) are used: they are of polystyrene (PS) type with a diameter of 30 μm or poly(methyl methacrylate) (PMMA) type with a diameter of 20 μm. A Calcium fluorite (CaF2) slide is used as a support to minimise the background (Fig. 2.9). This background is considered a species in our analysis.

Regarding some characteristics of our configuration, our laser has a power of 60 mW at the sample level. The slit at the entrance of the spectrometer has an opening ≤ 100 μm. Finally, the macromirrors of our DMD represent a bin of 10 by 10 micromirrors along the λ axis and the whole (=128 mirrors) is grouped on the x axis.

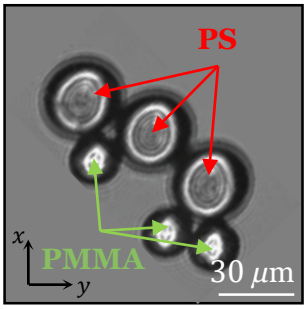

Figure 2.9: FOV taken from a microscope of a sample of mixed PS and PMMA beads. In this specific case, each of the beads can be identified beforehand by their size because the PS beads (30 μm) are of larger diameter than the PMMA beads (20 μm). The background of the image is a CaF2 slide.

Since our CRT approach requires the a priori knowledge of the pure species Raman spectra, we have conducted recording presented in figure 2.10(a). Each spectrum represents the average of 10 spectra measured at five different spatial positions with an integration time of 100 ms per pixel.

This prior knowledge of the system allows the design of optimal binary spectral combinations that are specific to each spectrum of each species. Still in (a), above the spectra are displayed these three binary filters (in black and white, one above the other) associated with the spectra of PS, PMMA and CaF_2. In order to be visually clearer, a grey/white area zone is extended on the spectra in (a) representing the extension of the binary filter adapted for the spectrum of the PS (the lowest filter of the 3). By extending

this filter, a trend shows that only certain peaks of the red spectrum are selected in the white parts and that all the rest are in the gray part.

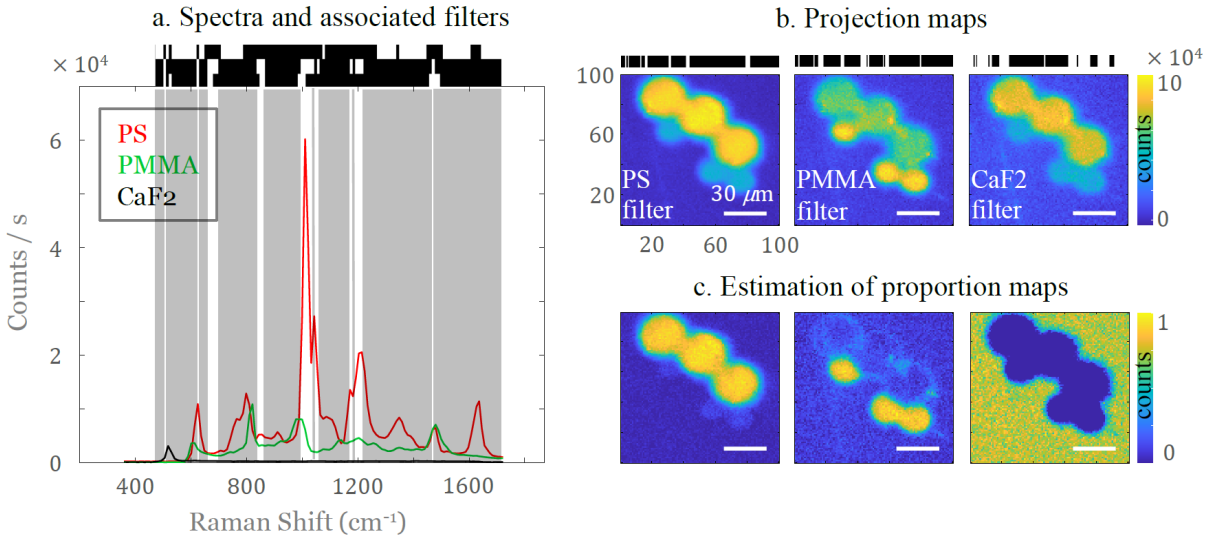

Figure 2.10: (a) Reference spectrum of PS, PMMA and CaF2, with the three associated spectral filters above and where the last of them is extended by gray bands on the reference spectra. **(b)** Projection maps of the three different spectral filters, from the image seen in figure 2.9, where the exposure time is 250 μs/pixel for each applied filter. **(c)** Maps re-evaluated from the projection maps in b., via normalization, thus representing the estimated proportions of each species. For each image, the scale bar is 30 μm.

Mechanically, on the DMD, the dark parts of our spectral combinations represent the OFF part of the DMD, *i.e.* the mirrors which reflect the wavelengths at this location towards an absorber. The white parts thus represent the ON part of the DMD where the mirrors reflect the Raman signal towards the detector.

Thus, the concept of a spectral filter is the discrimination of spectral signatures of one species among others. The spectral filters formed are specific to the set of spectra provided. In other words, the PS filter (*e.g.*) will be modified if the latter is found in another different spectral combination. Indeed the filter is based both on the spectral characteristics of the species it must filter, but also on those of others so that the differentiation is more effective. More details on the design of spectral filters will be given in the next subsection.

Once the spectral combinations have been constructed and adapted to the spectral identities of the three elements present in this sample (PS, PMMA, CaF2), each of them is projected onto the surface of the DMD in order to obtain the images of figure 2.10(b). The images are 100 μm² (where 1 μm = 1 pixel) and the unit corresponds to the number of counts per pixel. These are raw data images, obtained immediately after applying the various filters. After normalizing the data to make the three images consistent with one another, the proportion estimation maps are obtained and shown in Figure 2.10(c). It is then possible to distinguish the different species much more clearly.

Precision on the design of the optimized filters

The work concerning this section is mainly part of a collaboration with P. Réfrégier, F. Galland and T. Justel (Fresnel Institute) and is also based on the past work of C. Scotté [23]. Their works are available in the form of reviews and scientific articles summarize to provide a much more complete and detailed description than those given here [19] [115] [20] [21].

Here is detailed, the design of the spectral filters whose role is major in the CRT. Two conditions are set at the start of each new analysis: (i) the measured sample is assumed to contain a mixture of several pure chemical species (ii) the Raman spectral identity of each species is known (supervised imaging condition). The purpose of using these filters is to be able to identify and estimate the proportion of species that are mixed as accurately as possible.

In figure 2.10(a), we have deliberately visually simulated the effect that the binary filter adapted to the PS spectrum could have directly on the other spectra (PMMA and CaF_2). We could suggest that the construction of these filters is essentially based on the frequencies where the most important spectral peaks of a species are present. Nevertheless, the question of being able to discriminate such spectral data is often much more complex than such a simple model based only on spectral peaks. As already mentioned, our construction model for an optimal binary filter is based on the data set that can be extracted from the sample. Thus the model will take into account certain spectral peaks and their frequencies, but also the variances. All this on all the spectra available to obtain an optimal and effective filter for each species. This is why a binary spectral combination built from our model, and dedicated to filtering the spectral identity of a particular species, will not only depend on the characteristics of this single species.

Still with a simple and visual point of view, we represent our prior knowledge of the system, *i.e.* the reference spectra of each species, by a matrix S (Fig. 2.11(a)). This matrix allows us to simplify the model because we have incorporated for each species N both the data that can be associated with it and the variables relevant to the model (system transfer function, quantum efficiency, etc.).

These data already acquired allow the construction of M optimal binary filters for each N species ($N = M$) whose data will be contained in a matrix F (Fig. 2.11(b)). This construction is based on the Cramer-Rao bound (CRB). CRB is a lower bound, given by [19] with a minimum variance that, given the regularisation conditions, an estimator of a parameter can achieve. We are here looking for the closest variance to this lower limit to find the best estimator according to the properties of unbiasedness on the one hand, and efficiency on the other.

The mean-square-error (MSE) is the main criterion to minimise in order to optimise the variance of this quantitative estimator. It indicates the error between the estimate and reality. We note that various estimators can be used to minimise MSE. However, in my thesis, the variables of interest are the positive intensities and the photon number measurements. With these criteria, estimators that take into account the positivity constraints, although they may add bias, are necessary and can reduce this MSE as desired.

Thus, we use the *Non-negative Least-square* method represented by the simplified function *lsqnonneg* in Matlab. This method takes into account the positivity of the object (with mathematical constraints on positivity). For more details about this estimator, please refer to[19] [23].

If we want our results to be conclusive, we must require (at a minimum) that the estimator be unbiased and have the smallest possible variance among all unbiased estimators (= efficiency). By choosing to minimize CRB, our spectral filters can be calculated correctly to best maximize the accuracy of our estimator. Moreover, under the conditions where the Raman measurements are based on a Poisson noise model and where $M = N$ (the number of mask equals the number of species). The model based on CRB seems to be a good model on which to rely in order to model our optimal binary filters [19].

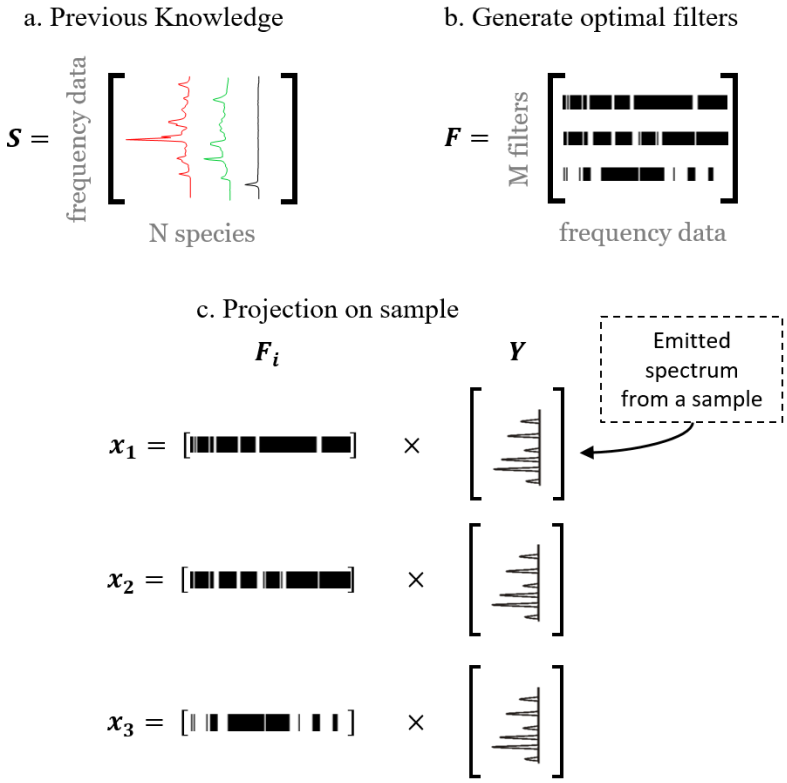

Figure 2.11: **(a)** Under supervised imaging conditions, we know the pure spectra of each species present in the sample, represented by our matrix $\boldsymbol{S}$. From these data, in **(b)** optimal filters, specific to each species and contained in the matrix $\boldsymbol{F}$, can be modeled based on the CRB. In **(c)** the $\boldsymbol{x_N}$ value equations representing the stage of projection of the filters (displayed by the DMD) on the sample.

Different filters are then projected (*via* the DMD) onto the sample. In compressive Raman, the combination of N species, previously selected by M filters, is summed by a SAPD giving the measure x_N (Fig. 2.11(c)). This value x_N thus allows the direct calculation of the vector C_N and allows to estimate the proportions from the following equation:

$$\boldsymbol{c_N = (F \times S)^{-1} x_N} \qquad \textbf{(2.6)}$$

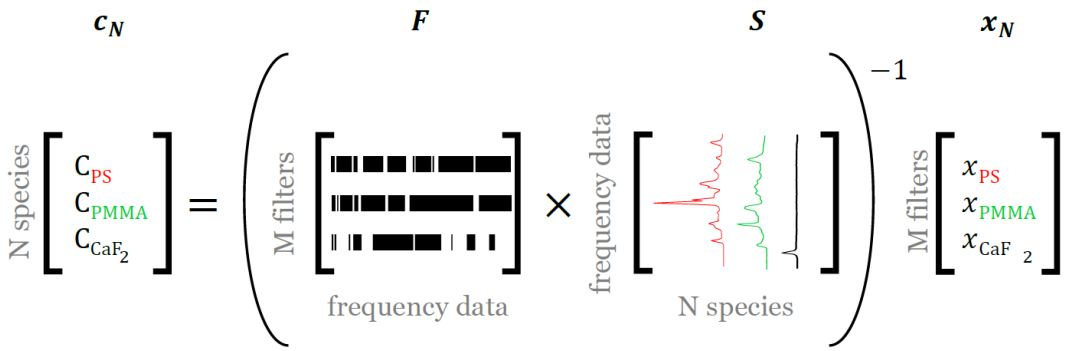

Figure 2.12: Visual and simplified representation of equation (2.6) of the application example treated in this section, with three chemical species: PS, PMMA, CaF_2.

Construction of the image, 1st method: Estimation of proportions

The combination species of the proportion estimation maps (Fig. 2.13(a)), according to the different filter projections, with a simple RGB filter application (Fig. 2.13(b)) and a common normalization to the brightest pixel leads to a final image (Fig. 2.13(c)). As indicated the scan speed is 250 μm/px, for each species (250 μs × 3 = 750 μs per pixel in total).

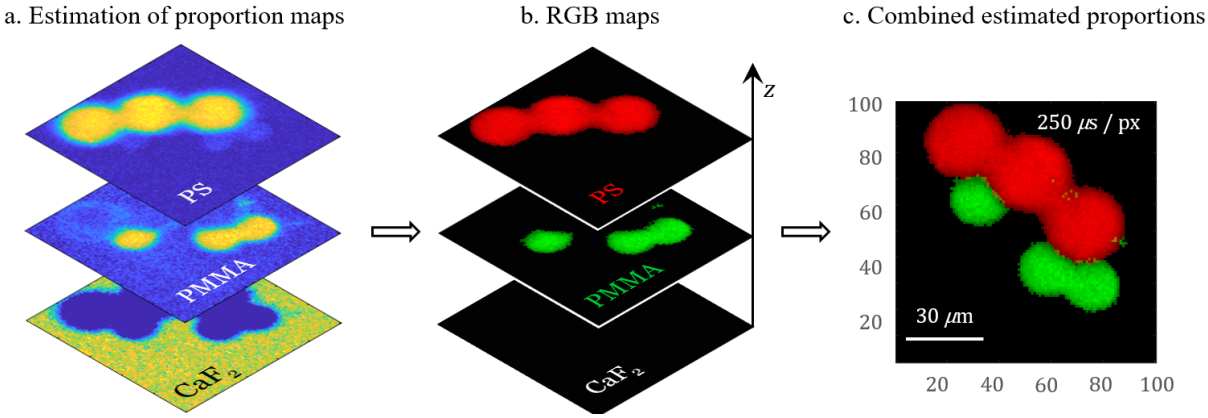

Figure 2.13: **(a)** estimates of proportions of each species seen in Figure 2.10 where **(b)** a different RGB filter has been added for each species map; CaF2 in black, PMMA in green and PS in red. In **(c)** we observe the combined image of the three different species with their estimated proportion and where the counts per pixel have been averaged. The FOV of each image is 100 x 100 μm (1 μm = 1 pixel) and the speed is 250 μm/pixel/species.

On the final image in (c), each of the species is detected and spatially identified using color filters. But what exactly is the meaning of a red, green or black colored pixel?

With the method used here (estimating proportions), an average number of photons counts of the three species is present in each spatial pixel in order to have an estimate of their proportion (≠ concentration). In a pixel is contained the data for each species. From these three different proportions contained in a pixel, a species identification (or classification) can be carried out.
In this specific case, we assume that there is indeed a single pure species at each point of the image by representing the color of the species which is the majority according to our estimator. Nevertheless, it must be understood that our estimate, although it can be effective, is paradoxical. Indeed, our starting hypothesis assumes the presence of pure species at each point. Only, a black point (*e.g.*) could have proportions of the type [0.1; 0.1; 0.8] where the majority species here is the CaF_2.
If proportions of the type [0; 0; 1] are not obtained, it is because our estimator has a certain variance. It is this variance that can sometimes cause classification errors when doing the classification with the estimation of proportion. We note that other estimators could help reduce the variance of the estimate (at the cost of possible bias). Further details are provided in [23] [19].
Although there may be sources of improvement, this estimator of proportions was used in a pharmaceutical study, where CRT was successfully implemented experimentally, in Chapter 3.

Construction of the image, 2nd method: Classification

An alternative to the estimation method (see chapter 4) is to directly classify the species from the numbers of photons recovered on the detector by filter applied. This is an approach that is unlikely to increase performance much, but the physical sense is closer to reality, thus providing consistent results. In the case of the estimation method, each point of the final image can display a superposition of the colors corresponding to each species, revealing the majority, weighted by the proportion of the species at each point. In this case we display proportions of each species at each pixel. If we weight each pixel by the total number of photons received, then we display the intensities by species. This is why we cannot speak of concentrations, because the multiplicative coefficients specific to each species are still missing which, combined with the measurement time, will allow us to go from the number of photons per second to the chemical concentration.
In the case of classification, it is assumed that there is a single species per pixel. A probability of error must be taken into consideration here. It will be limited by the bound of Bhattacharyya (BB). This bound is calculated from the reference spectra and the matched filters. The BB is greater than the probability of misclassification. Its limits lead to a simple expression of a minimum number of photons necessary to increase the probability of error. A detailed analysis of the BB bound in CRT classification can be found in [20].

The color corresponding to the class of the pixel can be displayed directly in each pixel, but this is far from a "physical" image since the intensities do not appear. Since we assume that there is a single species, we can weight the color of each pixel by the total number of photons received on the pixel. Indeed since in this case, all the photons are supposed to come from the unique species of the pixel.
This second method of analysis could not be used in chapter 3 during the pharmaceutical study because it was not developed yet at that time. However, it was developed for the environmental study (micro-plastics) that Chapter 4 presents, where it proved to be more adapted and coherent to the situation.

2.3 Conclusion

Through the explanation of several basic concepts, the main principles of compressive Raman have been introduced. The hyperspectral data cube was the first concept presented whose data recording process still raises storage, transmission and processing difficulties today. One solution, in order to directly study the information of interest without generating a highly dimensional data cube, is multiplexed measurement in the single-pixel imaging framework. A signal is mixed, detected by a multi-channel or even single-channel sensor, and not mixed by calculation. It is on this method that the CRT is based.
Compared to conventional Raman imaging, compressive imaging thus promises decisive advantages in terms of optimization of measurement time without losing quality. Simply because the compressive analysis allows the elimination of the post-processing imposed by the conventional measurement, as well as the time that this implies. Indeed, by its method, the CRT directly filters the spectral data during the measurement, without requiring more analysis time and directly detecting the desired information. We will not necessarily speak of increased speed but rather of optimization of the measurement time. On the other hand, the CRT imposes solid prior knowledge of the system studied in order to be used properly.
A long description of our compressive Raman configuration, oriented for application in different fields, has been made. In addition, justified choices of the implementation of certain elements in our configuration have been advanced as well as many key characteristics of the set up have been provided.
To end this chapter, we note that we have introduce compressive Raman and our that configuration of the latter presented, an applicative example seemed necessary in order to complete the explanation of the method.
Now that CRT has been fully explained application studies using CRT will be presented in the next chapter.

Chapter 3

Compressive Raman imaging for the analysis of pharmaceutical tablets

Contents

In the pharmaceutical industries, the legislation on medicines is more or less strict, depending on the geographical areas where it is applied, for health safety reasons. New medicines (just like vaccines) go through a long process in order to obtain market authorizations.

As a general rule, a pharmaceutical company wishing to bring a new drug on the market must submit an authorization file to the competent health authorities, *e.g.* in Europe it would be the European medicines agency (EMA). This file includes the results of numerous research studies and preliminary clinical and preclinical trials. As part of this research study, the file in question must guarantee the pharmaceutical quality, which includes the analysis of the chemical composition of the product.

Thus, pharmaceutical control is essential for the industry. Different techniques are used for this purpose, such as thermal analysis, differential scanning calorimetry, X-ray powder diffraction or electron microscopy.

Due to its non-destructive testing, vibrational spectroscopy has become an attractive alternative method for pharmaceutical control [116] [117]. This is why spontaneous Raman spectroscopy is a widely recognized analytical technique that extends from research laboratories to industrial process lines [118]. It has thus found interests into the analysis and quantification of active pharmaceutical ingredients [119] but also in pharmaceutical monitoring processes and online quality control [120] and would also benefit

from faster imaging capabilities [116]. Recent works have reported the use of SRS to assess polymorph distributions in tablets [121] [122].
The mapping of the distribution of pharmaceutical compounds thus seems to be an area which, in our opinion, could benefit from all the advantages CRT can offer. In this third chapter, we present our first applicative results on a pharmaceutical study in collaboration with the pharmaceutical company Sanofi.

Sanofi (Sanofi Research Development, Montpellier - France) provided all pharmaceutical samples for this research study in Chapter 3.

3.1 Experimental approach

3.1.1 Pharmaceutical compounds

The analyses are based on real pharmaceutical tablets, synthesized and marketed by the company Sanofi, as well as powders of the pure species that the basic constituents of these tablets. The different elements that make up these specific tablets are five chemical species. First there is the active compound - Clopidogrel - known to have two polymorphic forms [116] [123], which we called C1 and C2. The three other components are functional excipients which ensure the integrity of the tablet, the taste, the stabilization… They represent the major part of the volume of the tablet (as the active compound is generally only present in low concentration). These excipients are polyethylene glycol (PEG), corn starch (STA) and mannitol (MAN).
The commercial drug, which has the same name as its active compound -Clopidogrel-, is marketed to prevent platelet aggregation and reduce the risk of heart disease and stroke [124].

Our first experiments focused on measuring the reference spectra of each element. To do this, a small quantity of pure chemical powder of each species was deposited on a CaF_2 slide. The integration time per spectral base (10 grouped DMD mirrors) was 100 ms. The laser power at the plane of the sample was fixed at 60mW.
For each species, we averaged 50 spectra over five different spatial locations which were also averaged between them to finally obtain the reference spectra (Fig. 3.1).

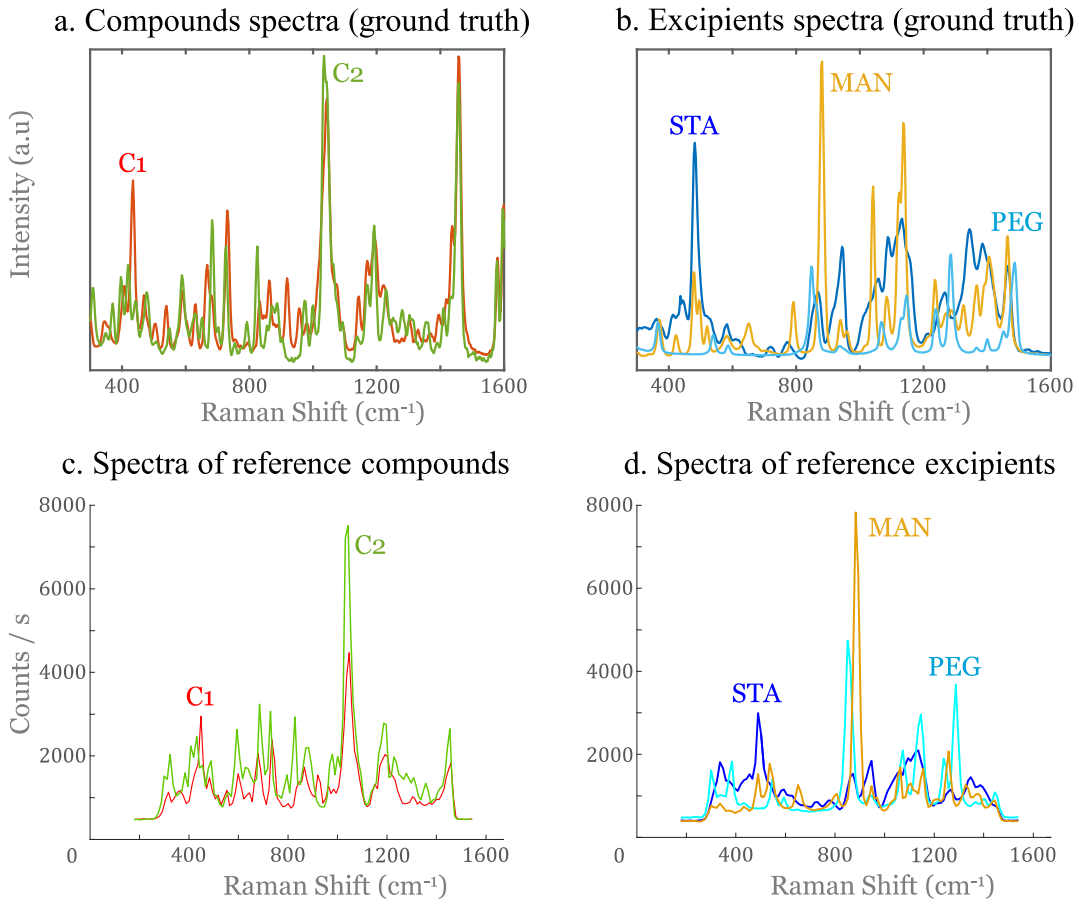

Figure 3.1: **(a-b)** Raman spectra of pharmaceutical compounds and excipients measured by Sanofi (considered as the ground truth) and **(c-d)** measured by compressive Raman.

A good match could be found between the Raman measurements provided by Sanofi (Figure 3.1(a-b)) and those measured with the CRT (Figure 3.1(c-d)) for the excipients and the two forms of Clopidogrel. It is not difficult to observe that the reference spectra of the excipients (Figure 3.1(b-d)) are much easier to discriminate than the reference spectra of the forms of the active polymorph compound C1 and C2 (Figure 3.1(a-c)).

3.1.2 Special case of C1 and C2 polymorphic forms

In the pharmaceutical industry, it is common that the drug production process leads to the formation of pharmaceutical compounds in different polymorphic forms [116] [123]. The word polymorphism refers to the ability of a compound to crystallize in more than one form [125] [126].

Among the plethora of pharmaceutical applications of Raman spectroscopy, the detection and quantification of polymorphic molecules plays a central role. Indeed, they often present very different pharmaceutical efficiencies [127]. This can be explained because the polymorphs have the same chemical composition but their arrangement and/or their conformation differ [128]. This leads to

differences in their physicochemical properties and many parameters such as solubility, dissolution kinetics, thermodynamic stability and bioavailability have been reported to be altered from one polymorph to another [123] [129].

Spectral analysis and construction of binary filters

The spectral characteristics of the C1 and C2 polymorphs can be compared from the figure 3.2 Although they have an identical molecular composition and a relatively close configuration [116] [123], these two polymorphs have very similar but not identical vibrational signatures, visible by the two Raman spectra measured in the fingerprint spectral region (Figure 3.1(c)).

As our CRT is based precisely on the differences between the specific vibrational modes (and therefore the spectral identity) to correctly discriminate the different chemical elements, this case of polymorphism would represent a real challenge for our system. Thus, before analysing the drug in its marketed form, we carried out initial analyses on the two polymorphic forms of Clopidogrel only. The aim was to verify whether a binary filter construction based on our method could be effective in this case.

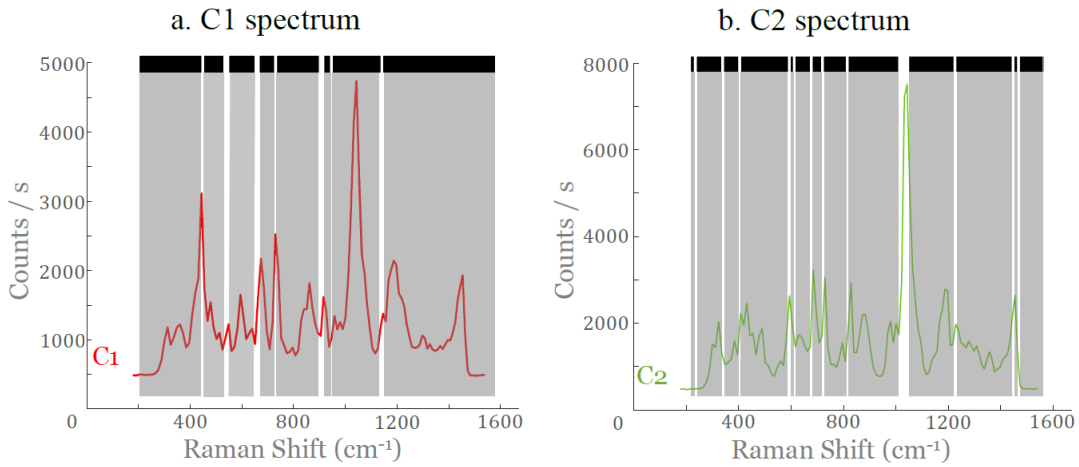

Figure 3.2: The Raman spectra of the two polymorphic forms of **Clopidogrel (a)** C1 in red and **(b)** C2 in green with their respective designed filter above each of them. Each filter is extended to observe which part of the DMD is OFF (grey part) = towards the absorber or ON (white part) = selected towards the detector.

The Raman spectra of C1 and C2 are once again represented in figure 3.2. These known spectra are used to design binary filters that minimize the variance of the estimated proportions of C1 and C2 following [19] [18]. The designed binary filters are displayed in Fig. 3.2 for the spectra of the two polymorphic forms C1 and C2, respectively. As explained in 2.2.4, the spectral filters are extended in order to simulate the display on the DMD where Raman photons falling into the white bands are retained while photons falling into the grey bands are rejected. Note that these two spectral filters were built with a third filter, that of CaF_2 (not shown in the figure). Thus, it is a combination of three binary spectral filters that was built in order to be able to discriminate between our three species (C1, C2, CaF_2). Moreover, these filters

are non-orthogonal, *i.e.* the same spectral region can be active (reflected towards the detector) on several filters. This choice was justified by the high similarity of the C1 and C2 spectra, in order to have a larger number of possible combinations of three filters.

An analysis on the C1 and C2 powders was first performed. We deposited a small quantity of mixed powder of the two polymorphic forms of clopidogrel on a CaF_2 slide. This mixed powder was derived from pure powder of each of the C1 and C2 species. The mixing was done randomly (concentration of C1 and C2 unknown). Figure 3.3 illustrates our first analysis.

Note that all the images shown in this chapter have a full pixel size (*i.e.* all pixels of the image size are exploited where 1 pixel = 1 μm). Moreover, no other image processing (smoothing, etc.) has been performed to improve the rendering of these images.

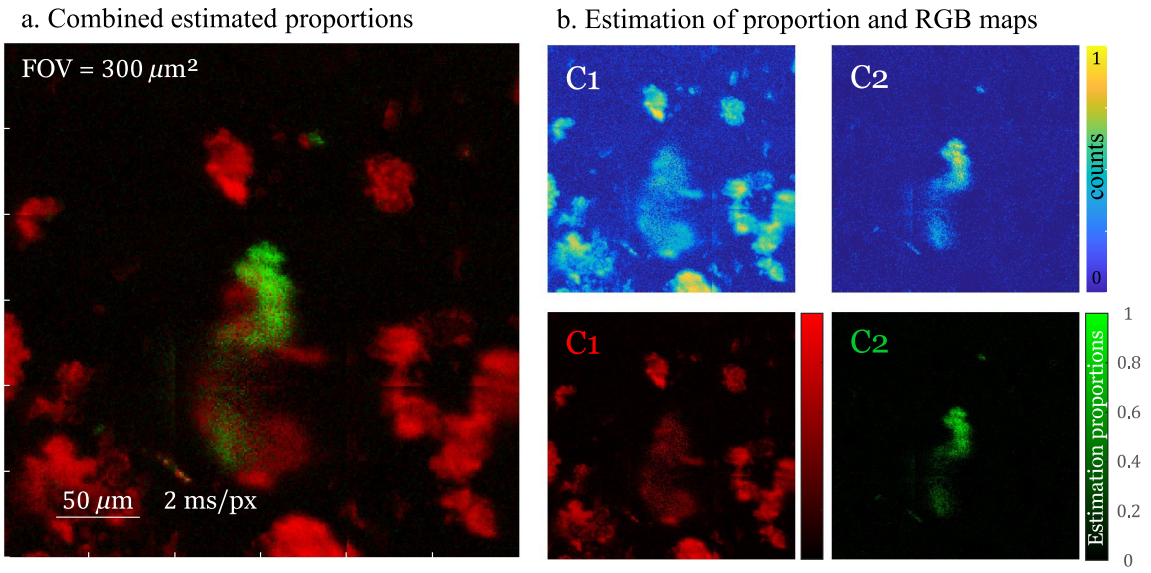

Figure 3.3: Illustration of the powder analyses of the two polymorphic forms of Clopidogrel. In **(a)** Combining C1 and C2 proportion maps. Pixel transit times are given per applied spectral filter (or species number). The scale bar is 50 μm. In **(b)** Maps of proportion estimates after thresholding and normalization (top), and with associated RGB filters (bottom). The background is a CaF_2 thin slide, shown in black.

We first show the proportion estimation maps associated with C1 and C2 (Fig. 3.3(b)) after thresholding and normalization (top), and associated with an RGB filter (bottom). The background (a CaF_2 coverslip) is also considered as a species but its estimation maps are not shown. When colored in red (C1), green (C2), and black (CaF_2) and combined (Fig. 3.3(a)), they provide a colored chemical picture of two polymorphic distributions in the measured powder mixture. From the three proportions of species (C1, C2 and CaF_2) present at each pixel, a classification is made out according to our CRT estimator [19] [18]: at each pixel, a single color is displayed which corresponds to the dominant species. This classification is justified because the mixture analysed was made from pure C1 and C2 compounds.

A first trend could suggest that our CRT system works to discriminate between the two polymorphic forms of Clopidogrel. Let us note that at certain places of the image, notably in the central part, the C1 and C2 superposition is not completely identified spatially.

This same analysis was repeated on a specific tablet (compact) synthesised by Sanofi (specially designed for this study), composed only of the two forms C1 and C2. Note that all the studies that involved pharmaceutical tablets were carried out without using a CaF_2 slide. These pharmaceutical tablets were directly placed on a metal support with a hole in the middle (Fig. 3.4). In this way, the pharmaceutical sample (larger than the central hole) could be deposited (in pieces or entirely) and observed directly through the objective lens.

Figure 3.4: Picture of a piece of pharmaceutical tablet on the microscope stage. The sample is placed on a metal support with a hole in the center and is visible directly from the objective lens.

To illustrate the relevance of CRT, the estimation of the CRT proportion of C1 and C2 mixed in a test pharmaceutical tablet was combined with an RGB filter and shown in Figure 3.5(b). The background (= the void in black) is always considered as a species (data not shown). When colored in red (C1), green (C2) and black (background) and combined (Fig. 3.5(a)), they provide a colored chemical picture of the two polymorphic distributions in the measured tablet. Note that we have chosen to image the rim of the tablet for clarity.

a. Combined estimated proportions b. RGB proportion estimation maps

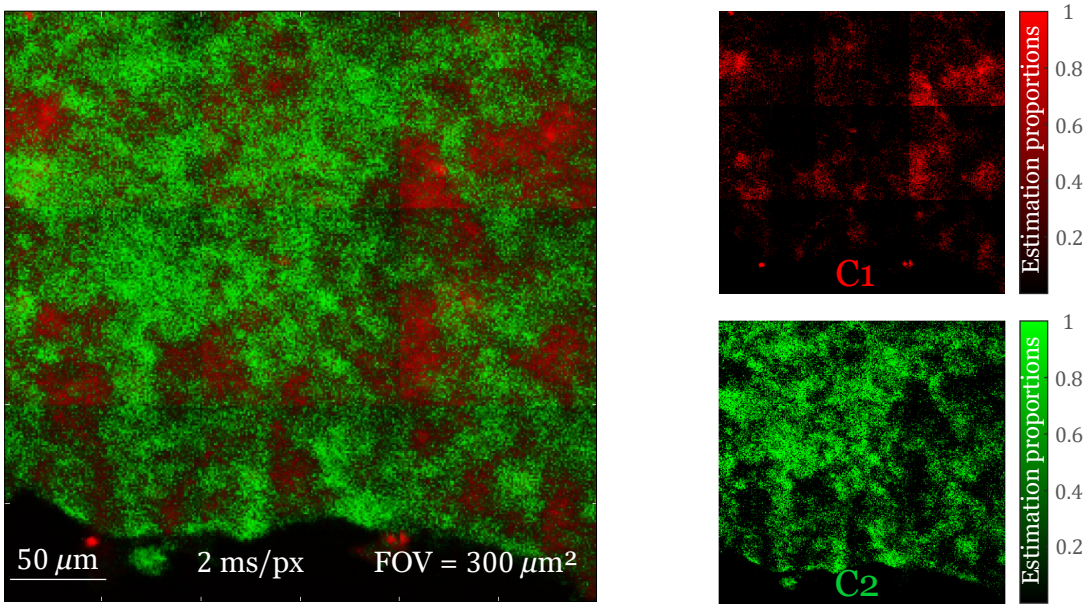

Figure 3.5: **(a)** Combination of C1 (red) and C2 (green) proportion maps in a compact tablet. Pixel dwell times are given per spectral filter applied (or species number). The scale bars are 50 μm. **(b)** Maps of proportion estimates after thresholding and normalization and with associated RGB filter. The background is the void (in black).

The same trend shows that CRT works to discriminate both C1 and C2 forms but this time for a solid tablet form. The C1 and C2 superposition in figure 3.5(a) is still difficult to identify spatially. This suggests that at these points a larger photons number (and therefore a longer acquisition time) would have been required to perfectly discriminate these two spectrally very close species.

CRT has demonstrated its ability to effectively discriminate between C1 and C2 despite their spectral proximity. Even if we noted a certain bias on areas where C1 and C2 was spatially superimposed.
The drug in its more complex form, with the two polymorphs of Clopidogrel and the three excipients, can thus be analysed in the following section. The same experimental approach will be retained. *e.g.,* a powder analysis will be done before that of the pharmaceutical tablet.

3.2 Study on complex pharmaceutical composition

3.2.1 Analysis of pure powders

This powder analysis considered all the chemical species of the pharmaceutical model marketed by Sanofi. It involved the two polymorphic forms of Clopidogrel (C1 and C2) mixed with the three excipients (PEG, MAN, STA). The powdered chemical compounds were deposited on a CaF_2 substrate without further preparation and directly imaged with the compressive Raman microscope. Their calculated reference spectra were used to numerically create a combination of six matched spectral filters (top rows - white pixels correspond to selected wavenumbers while black pixels correspond to rejected wavenumbers) (Fig. 3.6(a)).

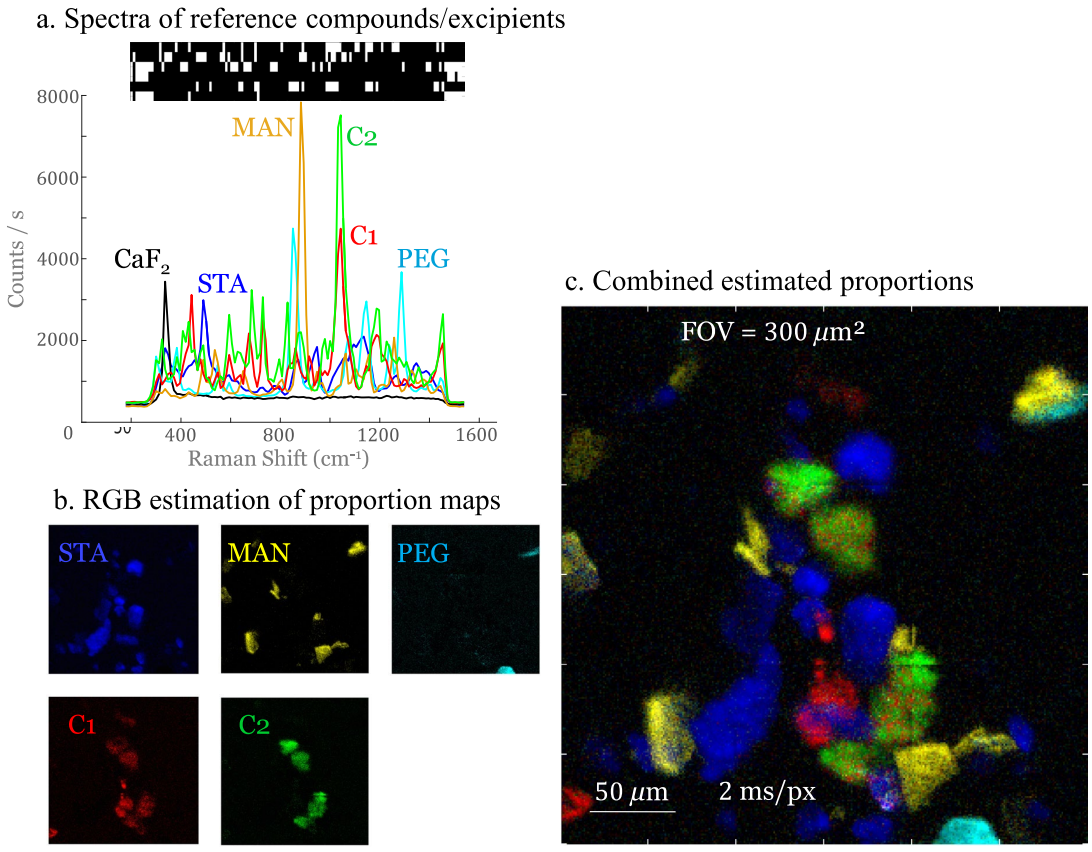

Figure 3.6: Powder analysis of six species: PEG, STA, MAN, C1, C2 and CaF_2. **(a)** Reference spectra and associated binary filters. **(b)** Proportion estimation maps with RGB filter. **(c)** Combining of the proportion maps of the six species. Pixel dwell times are given per spectral filter applied (or number of species). The scale bars are 50 μm.

Figure 3.6(b) shows the estimated proportion results (which have been color filtered) for each of the chemical components. These results are combined on the same image in Fig. 3.6(c). All species could be correctly identified and the proportion algorithms could recover the pure nature of the powder samples (each pixel is a pure chemical species). Note that in some areas of the image, the C1 and C2 superposition would not allow a complete spatial identification of these respective elements. The initial hypothesis (concerning the previous parts) requiring a larger photons number to be able to perfectly discriminate these two species is still assumed.

3.2.2 Complex pharmaceutical tablet

CRT Imaging

The compact tablet is 1.5 cm in diameter and ~2 mm thick. It is composed of the two polymorphs of clopidogrel and the three excipients in the relative proportion 10% C1, 40% C2, 40% STA, 5% MAN and 5% PEG. The five binary filters used for CRT imaging of the tablet (Fig. 3.7) were the same as those in Figure 3.6 and demonstrate the ability of CRT to operate with binary filters that were designed once (Fig. 3.6(a)) and kept the same for further measurements.

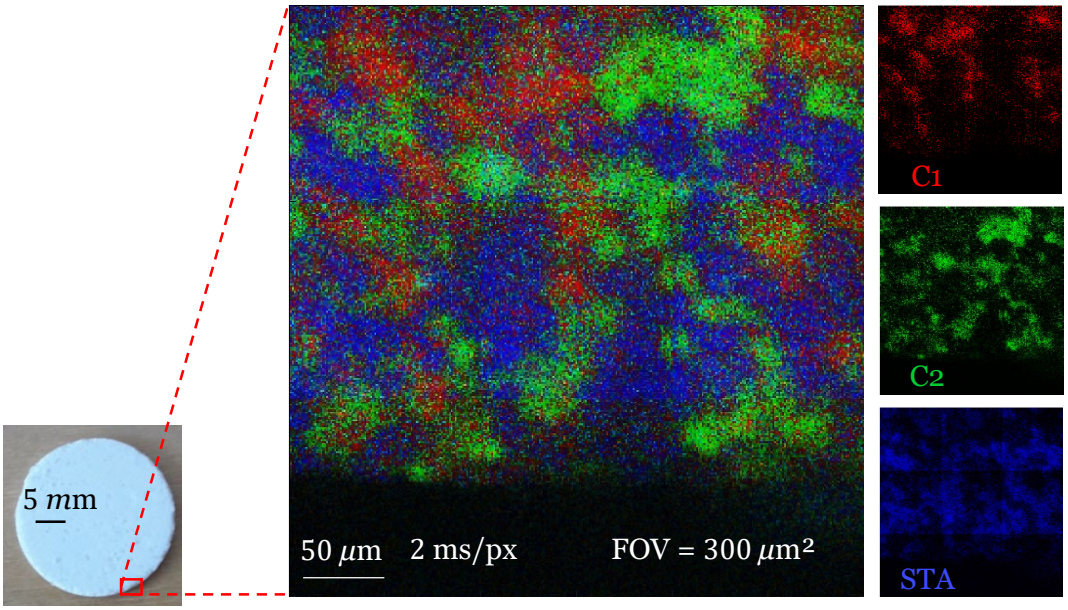

Figure 3.7: Complex pharmaceutical tablet composed of 10% C1, 40% C2, 40% STA, 5% MAN and 5% PEG as imaged by CRT. Only C1, C2 and STA could be recovered in this region of interest located near the tablet edge. Scale bar 50 μm, pixel dwell time for each species image is 2 ms and FOV is 300 μm².

Figure 3.7 shows the estimated proportion of the three most concentrated chemical compounds (C1, C2 and STA) on a 300 × 300 μm region of interest located near of the tablet edge. Note that the chemical species MAN and PEG could not be found in this region and several others due to their low percentage in the tablet.

High speed CRT Imaging

To investigate the ability of our CRT setup to perform fast imaging of complex pharmaceutical tablets, Figure 3.8 compares the CRT image quality achieved with pixel dwell time ranging from 0.5 ms/pix to 10 ms/pix. The chemical compound sample considered and the region of interest are the same as in Figure 3.7 (complex tablet).

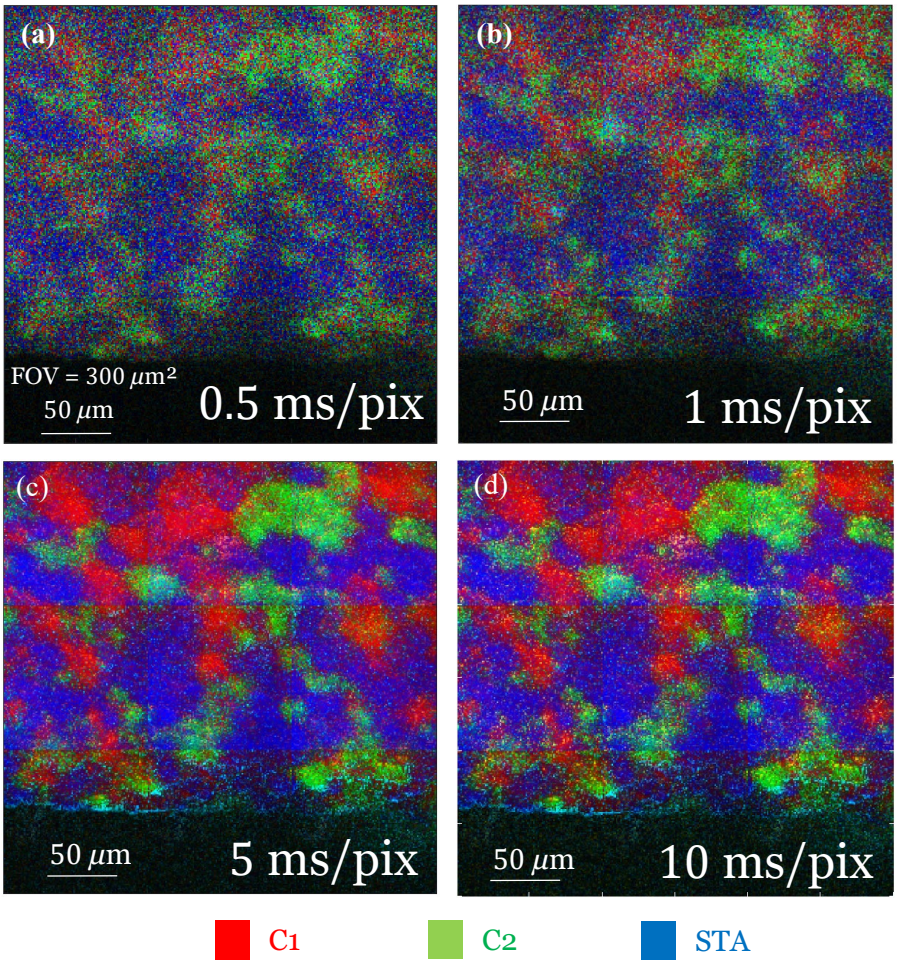

Figure 3.8: CRT imaging performed at different pixel dwell times. **(a)** 0.5 ms/pixel/species, **(b)** 1 ms/pixel/species, **(c)** 5 ms/pixel/species and **(d)** 10 ms/pixel/species. C1 and C2: polymorphs of clopidogrel, STA: starch. FOV is 300 × 300 μm.

At 0.5 ms/pixel/species it is still possible to distinguish the three chemical species C1, C2 and STA. This probably defines the speed limit on this type of sample to access a decent SNR for the detection of pharmaceutical chemical elements. Note that as the pixel dwell times increases, the probability of error decreases and the estimator reveals the precise chemical species at each pixel. Consequently, with increasing pixel dwell time, more and more pixels take on the same color on macroscopic zones that correspond to a pure chemical compound.

3.2.3 CRT and conventional Raman imaging

Ideally, Raman analysis should provide spatially resolved maps for active pharmaceutical ingredients, including polymorphs, and the associated excipients needed to ensure their bioavailability. However, Raman spectroscopy is often preferred over Raman imaging [130] because the acquisition of the full Raman spectrum for each sample spatial pixel, coupled with the low Raman scattering cross section and detector array noise, requires long acquisition time and generates large data sets.
Typically, spontaneous Raman imaging requires 0.1 s per pixel. This quickly results in an overnight acquisition time (>25 hours) to image a mm² pharmaceutical tablet area (including all image data pixels) with a spatial resolution similar to ours - around 1 μm – [131]. In particular, acquiring full Raman spectra at each sample pixel is a very inefficient and non-optimized way to map the spatial distribution of already known pharmaceutical compounds.
CRT is a more suitable and therefore more effective method in this specific field since it takes advantage of the knowledge of the molecular compounds (supervised imaging condition) present in a sample [19] [100] [99] [95] [101].

For comparison, CRT was used to map a pharmaceutical tablet with a FOV of 1 mm². This tablet is the same as previously analysed, with the same relative proportions: 10% C1, 40% C2, 40% STA, 5% MAN and 5% PEG. The result is shown in Figure 3.9. A scan speed of 2 ms/px was chosen since it seemed to be a very good compromise to demonstrate the performance of the CRT with good image quality.
As in the previous figures, no other image processing has been done to improve the rendering of the image and the entire pixel data is used (image of 1000 x 1000 pixels).

a. CRT imaging of a pharmaceutical tablet b. RGB estimation of proportion maps

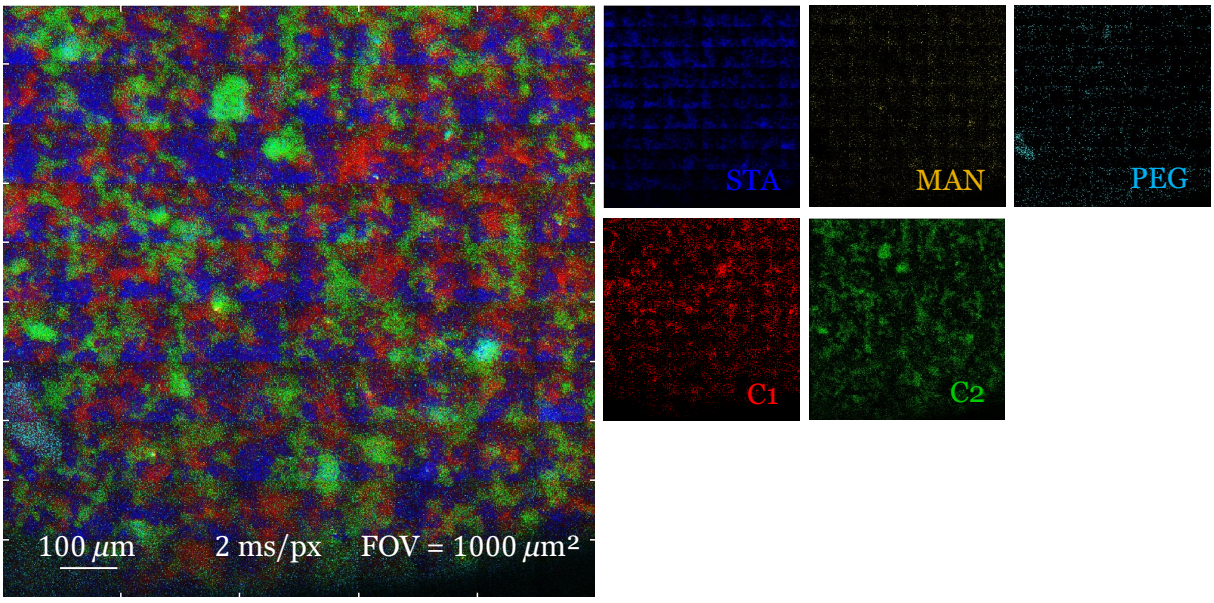

Figure 3.9: (a) CRT imaging of a pharmaceutical tablet composed of five molecular compounds. The image was obtained by **(b)** combining of proportion estimates of each compound where an RGB filter was applied. Each image species is taken with a pixel dwell time of 2 ms/px and on a FOV = 1 mm².

With a speed of 2 ms/px per filter applied (Fig. 3.9(b)) and a resolution of 1 μm, our current CRT system can image a 1 mm² tablet area in ≥ 35 minutes (for one species) with very good imaging quality. The superposition of each of these filter projections is visible in Figure 3.9(a). It was obtained after a total time of ~2 hours and 55 minutes. In the literature, these same measurement conditions impose, for a conventional Raman spectrometer, a total analysis time of > 27 hours [131].

3.2.4 Veracity of results

We finish this chapter by validating the identification step from the estimator performed by our CRT system on the different pharmaceutical elements. This is possible by recording the full Raman spectra contained at each pixel (λ) (Figure3.10(a)). These data were obtained by performing a fast spectral scan, using the DMD, for each estimated pure chemical species.

From a pharmaceutical tablet FOV of 100 μm², we were able to compare the averages of the full Raman spectra from pixels of the same color (Fig. 3.10(b)) with the reference spectra measured and shown in Fig. 3.6(a) (Fig. 3.10(c)).

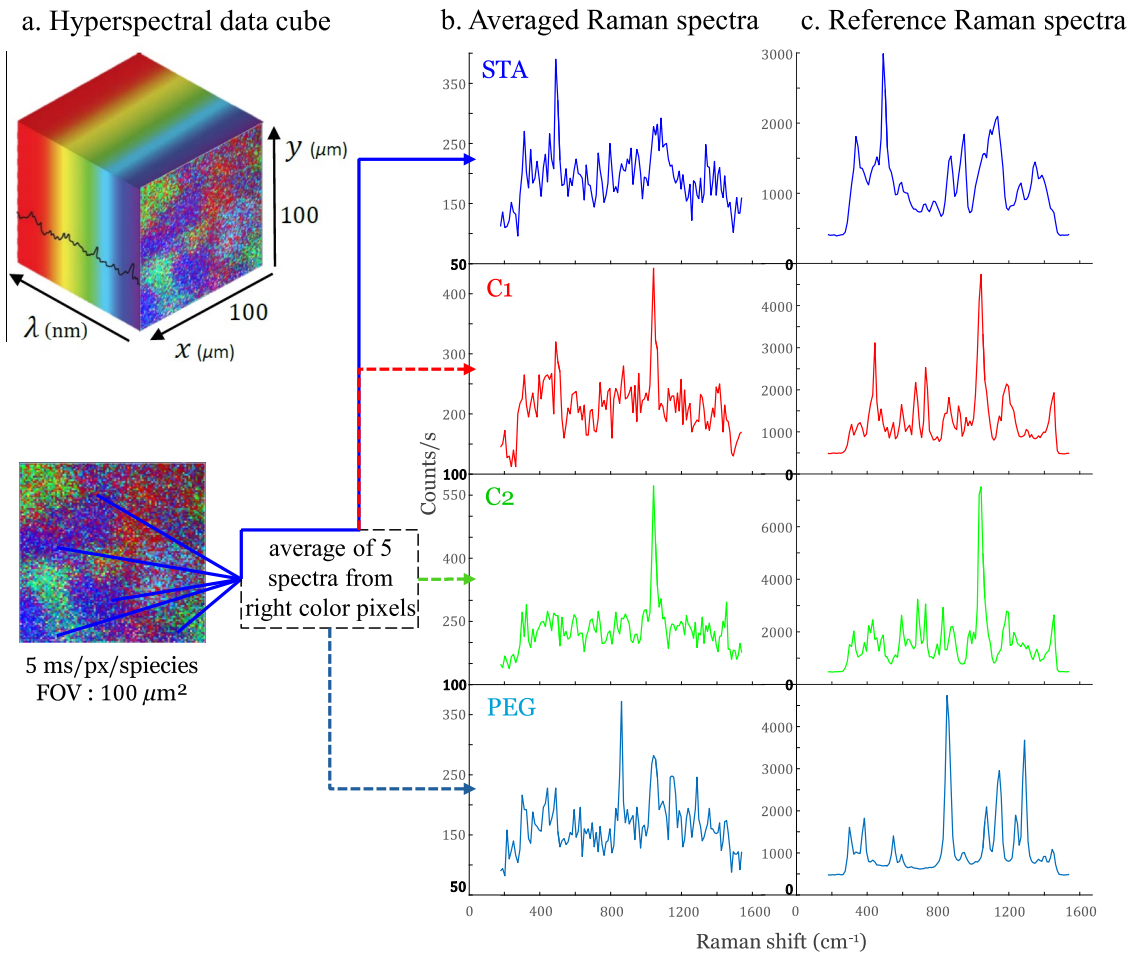

Figure 3.10 : **(a)** Acquisition of a hyperspectral image with the DMD with a speed of 5 ms/pixel/species and a FOV = 100 μm^2. **(b)** For better SNR, we averaged the full Raman spectra over five pixels from five locations of the same color in the CRT image. The full Raman spectra obtained in this region of interest (STA, C1, C2 and PEG) are compared **(c)** to the reference spectra of the pure sample (Fig. 3.6 (a)) obtained with an integration time of 100 ms.

Clearly, CRT is able to recover the correct chemical species for each pixel. We have successfully demonstrated the ability of CRT to estimate the chemical proportion of each polymorph and excipient at each pixel.

3.3 Conclusion

We have used CRT to map chemical compounds in compact pharmaceutical tablets among which two polymorphs show very similar Raman spectra (Fig. 3.1(a-c)). Due to the similarity of the Raman spectra of these two polymorphs, this represented a major challenge for our system based on binary filters.
The ability of CRT to estimate the chemical proportion of each polymorph and excipient at each pixel was successfully demonstrated. This is possible using the DMD, where a fast spectral scan at each frequency was performed to certify that our estimates (colour code displayed) were correct (on a hyperspectral data cube - Fig. 3.10)
We demonstrated that the imaging speed can be pushed up to 0.5 ms/pixel/species (2.5 ms total for 5 species) (Fig. 3.8(a)) to map a mixture of complex active pharmaceutical ingredients such as polymorphs and excipient in tablets. This leads to image a region of interest of 300 × 300 μm in 45 s per species (≤ 4 minutes for 5 chemical species).
By stitching together the FOV (combination of images forming a mosaic with a larger FOV), our current CRT system should be able to image a 1 mm² tablet area in ≤ 45 minutes with a speed of 0.5 ms/pixel/species and a resolution of 1 μm. Even though our Figure 3.9 is based on a speed of 2 ms/pixel/species to show superior image quality, it still proves the efficiency and speed of CRT.
An accurate comparison between CRT and SRS is difficult due to the drastic technological complexity and cost of on SRS system [122] [132]. But these latest results could be compared to recent results obtained with SRS in [122], which required a total pixel dwell time of 4 ms per species to obtain similar images on identical tablets.

Some improvement could be made to improve the CRT speed. For instance, all the analysis performed in this chapter were based on an estimation model. This is clearly not optimal as each pixel considers a mixture and only displays the color of the dominant species when it is possible that the pixel is composed of only one pure chemical species. This is why an analysis based on a classifier should improve CRT imaging speed [115] [20].
Furthermore, we presented images with a full pixel dataset only (*i.e.* for an image where 1 pixel = 1 μm, a 100 x 100 μm image implies 100 x 100 pixels). This characteristic thus gives us the possibility to present images with a faster acquisition time by adjusting the sampling ratio (number of measurements / number of total pixels) [133]. This method will be implemented in Chapter 4, on another application.

Obviously, for this type of application where the compounds are known *a priori*, CRT is advantageous over conventional Raman imaging, as it exploits prior information and leverages that information in the measurements strategy. Thus, taken together, our results proved that CRT is a valuable and attractive alternative technology to spontaneous Raman for mapping active pharmaceutical ingredients, with potential application in rapid quality control.

Chapter 4

Compressive Raman imaging for the analysis of microplastics

Contents

The increase in plastic use and the limited ability of recycling efforts are leading to a huge accumulation of plastic on our planet. Since 2000, the world has produced as much plastic as all previous years combined [134]. Virgin plastic production has increased 200 times since 1950 and has grown at a rate of 4% per year from 2000 to present. If the total planned plastic production capacity in the world is already reached, production could increase by 40% by 2030 [135]. A third of the plastic waste produced ends up in nature, *i.e.* 100 million tonnes in 2016 [136].

Plastic has been found all the way to the bottom of the Mariana Trough [137] and in the Arctic sea ice [138]. This pollution alters soil conditions by increasing the risk of infiltration of harmful chemicals, which can have an impact on the health of fauna and flora [136]. It is also present in coastal ecosystems and accumulates in ocean gyres around the world.

When left in the environment, plastics degrade according to kinetics that depend on abiotic (ultraviolet rays, oxygen, water, etc.) and biotic (microorganisms) factors. The degradation of plastics results in their fragmentation into small particles. When these are smaller than 5 mm, they are called microplastics (MPs). Nanoplastics (between 1 nm and 1 μm in size) are also released as plastics age. This ageing can be caused by erosion of their surface, which is altered over its first few micrometers, particularly under the effect of oxidation. From visible pollution, plastic pollution thus becomes invisible.

As a result, animal species likely ingest large quantities of plastic of various sizes, which their digestive systems cannot absorb, resulting to internal burns, digestive obstructions, and even death [139]. Additionally, toxins from ingested plastic have been shown to harm reproduction and weaken the immune system of animals [139].

The human species is of course not spared: "*It is estimated that a person could ingest an average of 5 grams of plastic per week*" - the equivalent of a credit card. This new study from the University of Newcastle (Australia) took a closer look at the lack of data on the impact of plastic pollution on human diets [140]. The study aimed to estimate the average amount of plastic ingested by humans. The results confirm concerns about the large amount of plastic we ingest every day and the effects this could have in the long term.

Solutions to plastic pollution must be a priority in areas such as health, food and of course the environment. However, potential solutions are complex, cross-border/multilateral. In addition, the sources of plastic are varied and modified by additives, ranging from textiles and tire dust to bottles and packaging. In order to know *how* and *where* intervene effectively, whatever the area concerned, a realistic assessment based on representative data on the quality and quantity of responsible plastics must be known.

Conventional Raman spectroscopy is one of the main methods used for the identification of very small MPs (< 20 μm) [1], together with FTIR (Fourier transform IR spectroscopy) [141] [142] and GC/MS (Gas chromatography-mass spectrometry). Raman spectroscopy would nevertheless seem to be the best candidate to effectively detect/identify the full range of MPs [143]. Identifications of plastic families have already been carried out by Raman spectroscopy, whether in sediments [144], in the oceans [145] [146] or in marine organisms [147] [148] [149]. MPs identification by stimulated Raman scattering (SRS) has recently demonstrated acquisition speeds >100 times faster (a few μs per spatial pixel) than conventional Raman mapping on samples of the same type [150]. This presents SRS as a good candidate for monitoring MPs in the environment. However, its use is an advantage that comes at the cost of a drastic increase in technological complexity (ultra-fast lasers, lock-in amplifier detection, etc.) [122] [132] as well as its financial burden and more extensive training to operate. Fieldwork, such as the study of MPs, can benefit from a less expensive and easier to use tool.

It is in this context that we propose to use CRT in order to perform fast detection, fast identification and quantification of MPs. During this thesis, we could collaborate with IFREMER Brest who provided samples from the sea that contain MPs.

4.1 Experimental approach

4.1.1 New classification method

Until now, to map different elements of a sample, we have used the classifier based on the estimation of proportions. In this chapter, we make use of a direct classification algorithm, that was already mentioned at the end of chapter 2. This new approach is used to directly classify the up species from the photons numbers recorded by the detector for each different applied filter, without going through an estimation step (Fig. 4.1). This new approach allows us to perform faster detection and identification.

With the classification strategy, our starting hypothesis is that there is a unique species at each pixel (Fig. 4.1(b2)). The estimator, on the other hand, assumed from the outset to have a mixture in a pixel, *i.e.* to contain the proportions of each species (where only the dominant species was displayed) (Fig. 4.1(b1)).

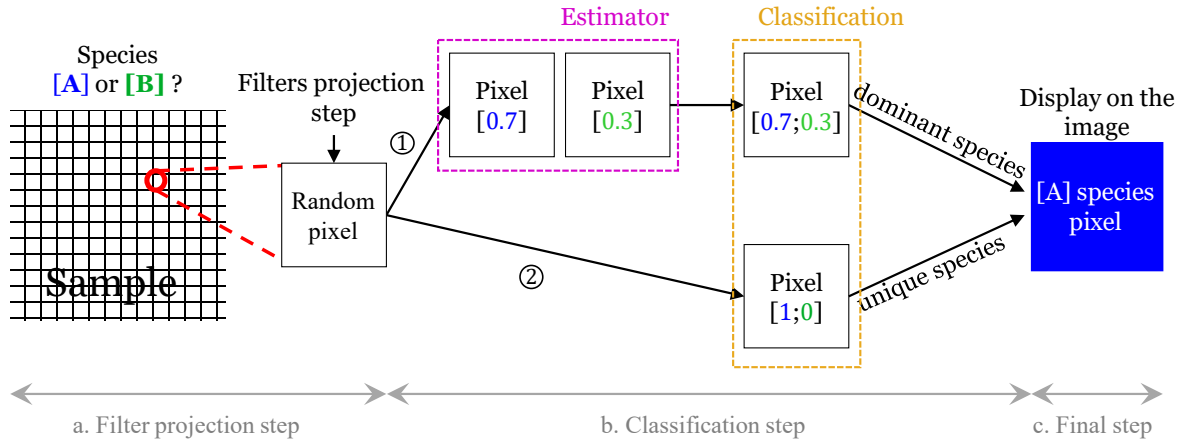

Figure 4.1: Simplified illustration of the two classification methods used in this thesis. **(a)** Represent a random pixel on which several filters will be projected to know which color (species) it will represent. **(b)** Is the classification step applied **(1)** with an estimator or **(2)** directly. **(c)** Is the display step of the color selected by the classification.

From Fig. 4.1, we saw that a direct application of the classifier allows us to skip the estimation step (Fig. 4.1(b2)). This classifier is based on the different Raman signal returns (number of photons: x_1, x_2) obtained after the application of the different spectral filters depending on the species A and B. The probability of species A or B for each pixel in the sample is then compared. The classifier then chooses the species to be displayed in each pixel of the sample according to the highest probability of identification (equation 4.1). Therefore, for a single pixel, we now have one and only one data corresponding to the species whose associated color is displayed.

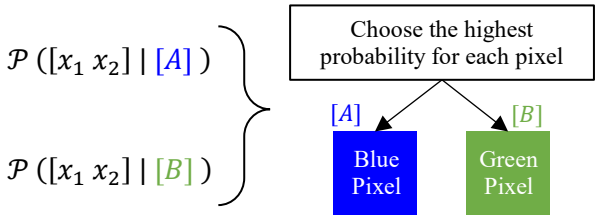

(4.1)

The variance of this classification will be directly limited by the Bhattacharyya bound (BB). As a reminder, BB is an upper bound which is calculated from the reference spectra and the matched filters. It is therefore greater than the probability of error of the classification method. Its limits lead to a simple expression of a minimum number of photons necessary to increase the probability of error. Our colleagues from the PhyTI team in Fresnel have recently proposed a classification scheme based on the BB bound that we will use in this chapter [20].
In this direct classification scheme, we assume that there is only a single species at each pixel and we display the results by weighting the color by the total number of photons received on the pixel. This enable to have a color scale that is representative of the amount of MP at each pixel.

It should be noted that the use of combinations of non-orthogonal binary filters represented results much less convincing than that of orthogonal binary filters. We won't go into more detail here but a quick comparison of some results is shown in Appendix 1. For these experiments, the laser power at the plane of the sample was around 60 mW.

4.1.2 First try: artificial and colorless MPs

Before the analysis of plastics from the natural environment with various colors and sizes, our preliminary tests were carried out on Polyester (PS) and poly-methyl methacrylate (PMMA) beads. A fairly simple analysis was shown as an example application at the end of Chapter 2.

The following tests were carried out on colorless artificial polymer powders. They were provided by L. Zada (VU Amsterdam, The Netherlands) who works on the SRS for the identification of MPs [150]. The powders were obtained by grinding each type of polymer with sandpaper (high production volume polymers).
Simple and rapid experiments were carried out on powders of polypropylene (PP), polyethylene (PE) and polyethylene terephthalate (PET), Nylon (PA) and beads (20 μm diameter) of Polyester (PS). The sizes of the different plastic particles were relatively unequal, ranging between a few tens and hundreds of μm.
For the calibration step, a small amount of pure powder and beads of each plastic polymer was placed on a separate area of a CaF_2 slide to record their reference spectra and construct the associated spectral filters (Fig. 4.2(a)). This step turned out to be complicated because a lot of background noise came from many particles of the different polymers. We therefore took this background (photons) into account in each reference spectral model of our polymers. Note that all reference spectra of each polymer are shown individually in the next part in Figure 4.5. We blended these five plastic polymers to make an image from the microscope view shown in Figure 4.2(b).

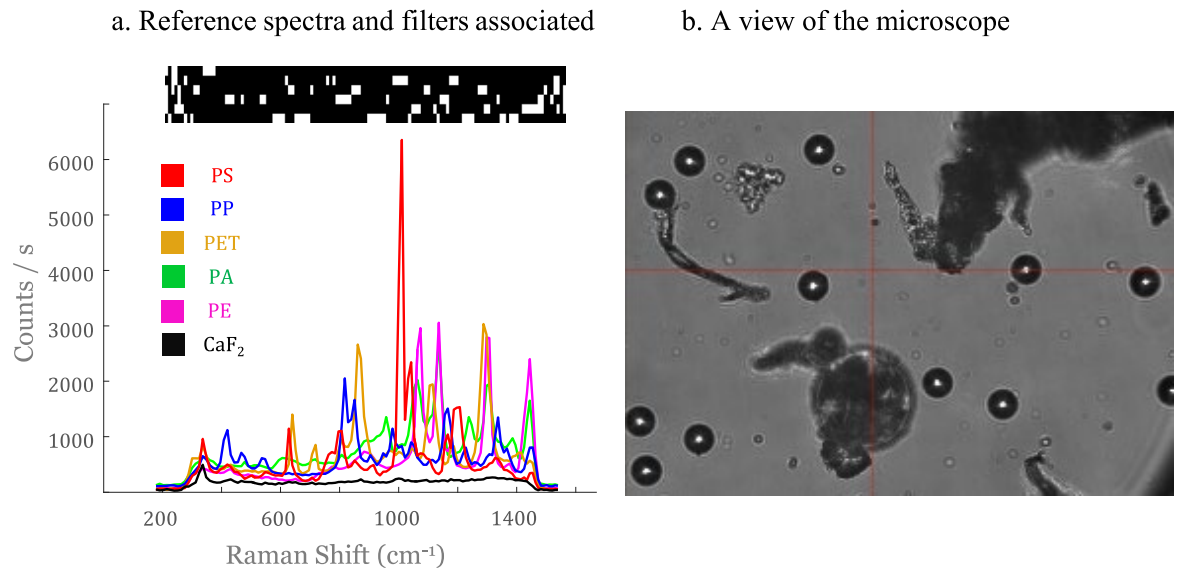

Figure 4.2: **(a)** reference spectrum of MPs and associated optimal filters. **(b)** FOV of the optical microscope selected to image a mixture of different colorless plastic polymers.

We have generated two classification map images from the FOV in the white light transmission seen in Fig. 4.2(b) with imaging speeds of 0.5 and 1 ms/px by projection of the five different spectral filters (Fig. 4.3(a)). The different filter projections for the spectra of PS, PET, PE, PA and PP are shown in Fig. 4.3(b) with the speed of 1 ms/px each. The CaF_2 projection map has not been displayed.

As previously mentioned, to obtain these images we retrieve the photons number data acquired directly by our detector without going through an estimation step. Since our direct classification assumes a single species per pixel, the signal at each pixel is the sum of all measured photons for all projection maps.

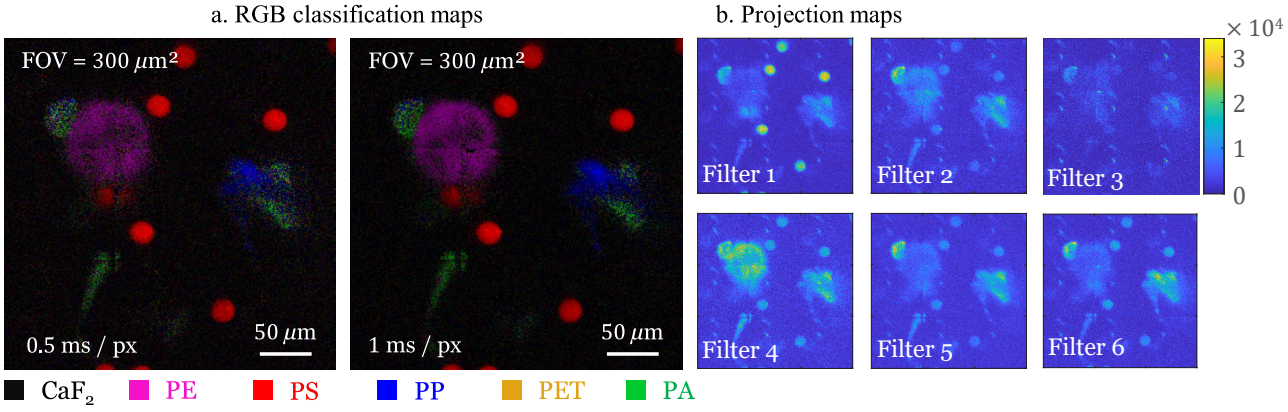

Figure 4.3: **(a)** Classification maps, associated with RGB filters for filter projection speeds of 0.5 and 1 ms/px, obtained from the classification algorithm applied to **(b)** filter projection maps for the speed of 1 ms/px – FOV is 300 × 300 μm and the scale bar is 50 μm.

This FOV was taken randomly in a place where all the MPs were mixed on the surface of the coverslip. The five filters were applied to detect and identify the possible presence of these five different plastic polymers. PET seems to be absent from this analysis area.

Concerning the projection maps (Fig. 4.3(b)), as in the drugs application in Chapter 3, these raw data (photons number received) cannot each be attributed specifically to a species of polymer unlike the maps of proportions. Simply because we recall that a filter is not built specifically for a species but rather for all known spectra (Fig. 4.2(a)). This is also why visually, in figure 4.3(b), it is difficult to visually assign a type of polymer for each pixel. The only exception in this case remains the PS, not being a powder but uncolored homogeneous beads, it is easier to see visually where its filtering is carried out (first map at the top left). Once the direct classification algorithm is applied, the various MPs are clearly distinguishable.
On the classification maps (Fig. 4.3(a)), the pixels identifying PA (green) and PE (blue) to overlap in certain areas and, therefore, not being correctly identified. This misidentification is more noticeable on the image with an acquisition speed of 0.5 ms / px. When we switch to a speed of 1 ms/px, where more photons can be collected per pixel, this superposition disappears and a more homogeneous color appears on each MPs.

These first results on pure and colorless plastics allowed us to introduce MP mapping with CRT. Working with more realistic MPs is challenging because of the possible presence of a specific background noise as we will see in the next section and as often discussed in the literature [1] [151].

4.2 Study on MPs collected from environment

4.2.1 Field data recording

All MP samples were provided by the marine ecology study office IFREMER (Institut Français de Recherche pour l'Exploitation de la Mer, LDCM - Laboratoire Détection, Capteurs et Mesures - Brest - France).

The samples provided by IFREMER came from natural environments (sea, beaches, etc.). They were macroplastics with sizes ranging from a few mm to a few cm. These raw samples have undergone initial treatments before their analysis with Raman spectroscopy. These treatments consisted in filtering the plastics of such as present in the harvest samples. Next, the filtered plastics were cleaned to be finally crushed (by cryo-crusher: act of cooling a material and then reducing it into a small particle size) to produce plastic microparticles of different types (and colors) and different sizes. The samples are placed in several Eppendorf tubes. Each tube has a different type of plastic polymer (Fig. 4.4). Each type of plastic polymer has a different color caused by its own (unknown) additives that were originally added to it during its manufacture.

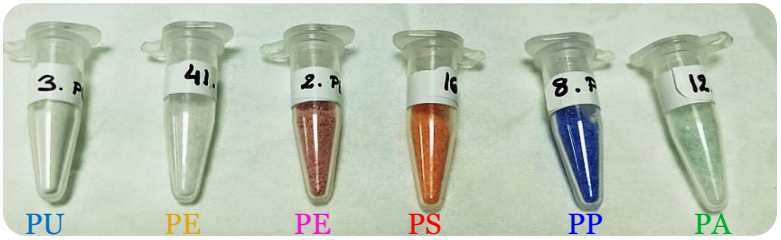

Figure 4.4: MPs samples provided by IFREMER arranged by type of plastic polymer.

In figure 4.4 from left to right, we have a sample of polyurethane (PU, in white), polyethylene terephthalate (PET, no colored), polyethylene (PE, in pink), polystyrene (PS, orange), polypropylene (PP, in blue) and Nylon (PA, in light green). It should be noted that the sample concerning polyvinyl chloride (PVC) was excluded from the study because its additives (complementary component such as dyes) give to the PVC samples a black color. During the measurements, the black color of the PVC samples induced a strong background noise and the PVC microparticles began to burn due to their interaction with the IR (785nm) excitation light (Appendix 1). Further analysis is required to determine whether the colour is directly related to the reactions observed in Appendix 1 and how to remedy them. For recording reference spectra, each polymer was placed on a separate area of a CaF_2 coverslip. Several spectra were acquired in each area for an integration time of 100 ms per spectral base: 50 spectra are averaged over five different spatial locations. The averaged spectra from each area are also averaged to finally obtain the reference spectra (Fig. 4.5(b)). As mentioned earlier in this manuscript, the reference spectra are acquired by the sequential activation of the binned spectral pixels on the DMD and the subsequent recording of the Raman signal by the photo-detector. For these experiments, the laser power at the specimen plane was always set at around 60 mW.

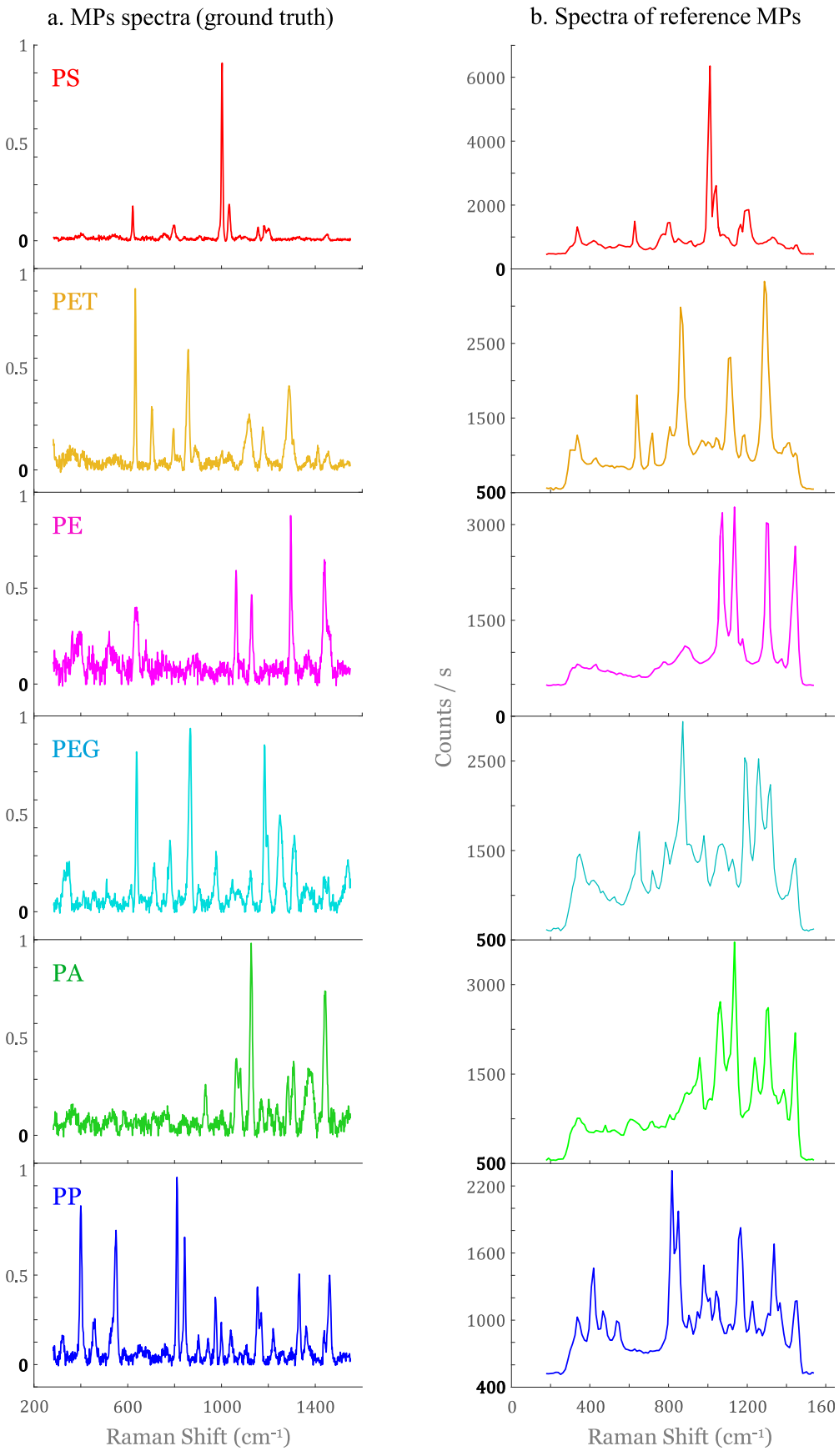

Figure 4.5: **(a)** Raman spectra of plastic polymers measured by IFREMER and **(b)** measured by our compressive Raman spectrometer for an integration time of 100 ms per spectral base.

We can compare our reference spectra (Fig. 4.5(b)) with the spectra measured by Raman spectrometry from the IFREMER laboratory ((MPs spectra - ground truth, Fig. 4.5(a)). The background noise specific to this type of this sample (fluorescence [1] [151]) is clearly visible in our spectra (Fig. 4.5(b)). This same noise was removed numerically in Fig. 4.5(a): polynomial subtraction of the background noise on the ground truth IFREMER spectra. Note that our CRT optima filter will work with this background. Beside this noise contribution, there is a good agreement between our reference spectra measurement and the IFREMER ground truth.

4.2.2 Analysis of a mixed sample of MPs

CRT Imaging

Following the recording of the reference spectra (Fig. 4.5(b)), the construction of orthogonal binary filters was carried out optimally for all the spectra of the six plastic polymers (Fig. 4.6(a)). Indeed, the use of non-orthogonal binary filters in combination with each other has shown much less convincing results than orthogonal binary filters. We will not go into more detail here but a quick comparison of some results is shown in Appendix 1.

These different filters were projected onto a sample where all the different MPs polymers (PS, PP, PET, PU, PA, and PE) were mixed on a CaF_2 coverslip. The chosen imaging area corresponds to a FOV of 300 μm^2 where we wanted to find a maximum of these different polymers (Fig. 4.6(b)). To do this we checked the spectra of each MP piece present in the imaging region.

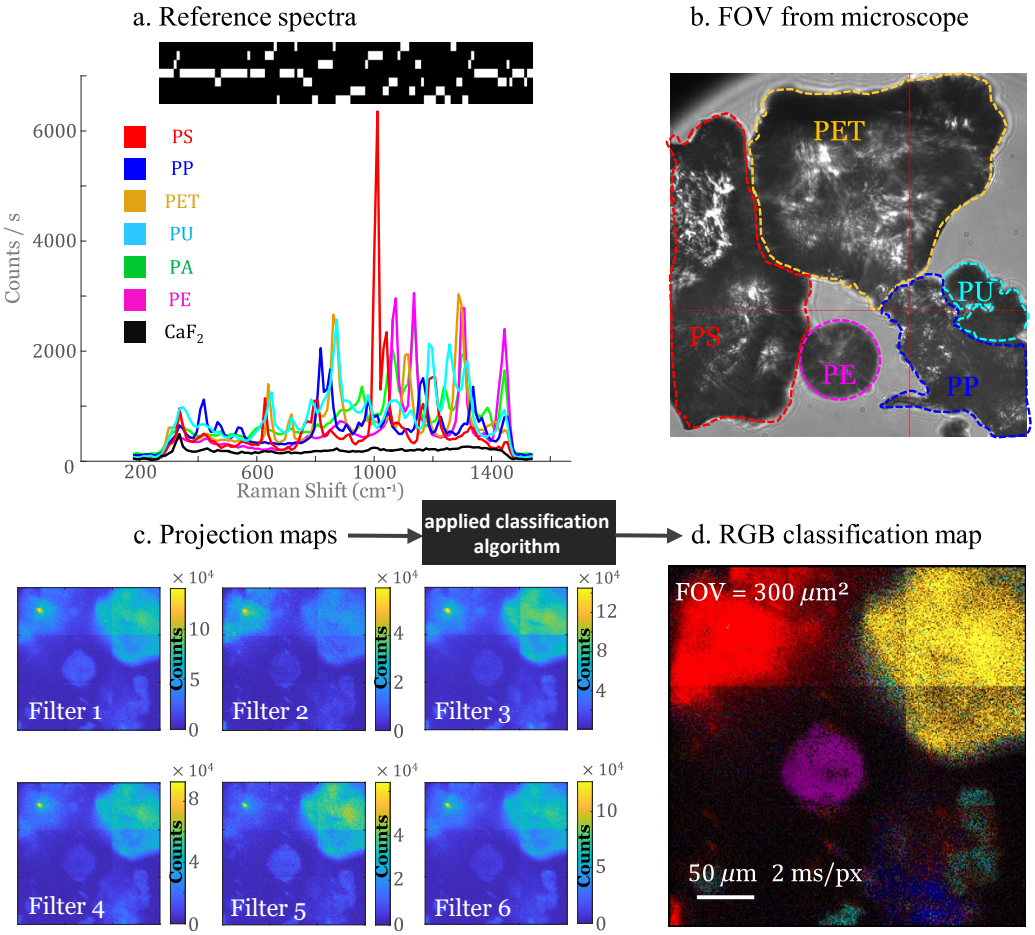

Figure 4.6 : **(a)** Reference spectra and filters associated. **(b)** FOV seen from the microscope where the different polymers of plastics are known. **(c)** Projection maps. (d) CRT imaging with an acquisition speed of 2 ms/px by filters applied – FOV is 300 × 300 μm and the scale bar is 50 μm.

After the projection of each filter on the chosen imaging region, we obtain our different raw data, *i.e.* the photons number received per pixel (Fig. 4.6(c)). The photons number per pixel received was 4× time larger compared to the colorless synthetic plastic samples (section 4.1.2). The increased photon count can be explained by a background noise resulting from the additives that have been linked to the composition of these plastic samples [1] [151].

We produced an image after classification of each pixel for a plastic polymer type where an RGB filter is applied (Fig. 4.6(d)). A clear spatial identification of MPs is observable. We can discriminate the different color zones, which well agree to our predictions (figure 4.6(b)), with PET in yellow, PS in red, PE in purple, PU in light blue, PP in dark blue and CaF_2 in black. No PA could be found in this FOV.

Nevertheless we notice that the image taken from figure 4.6(b), is not fully represented in fig. 4.6(d). The part corresponding to the PS (red) is in contact with the PET (in yellow) as far as we can see in (figure 4.6(b)). However, on the final classified image (Fig. 4.6(d)), we observe a blurred area between the yellow and red parts. This can be explained by the rough surface of the MP that would require to acquire the signal over different z plane to obtained a full colored pixel area.

High-speed CRT Imaging

To investigate the ability of our CRT setup to perform fast mapping in the detection and classification domain of MPs, Figure 4.7 compares the CRT image quality obtained with a pixel dwell time ranging from 0.1 ms/px at 2ms/px. The sample used and the 300 μm^2 FOV region of interest are the same as in Figure 4.5 (mixture of MPs).

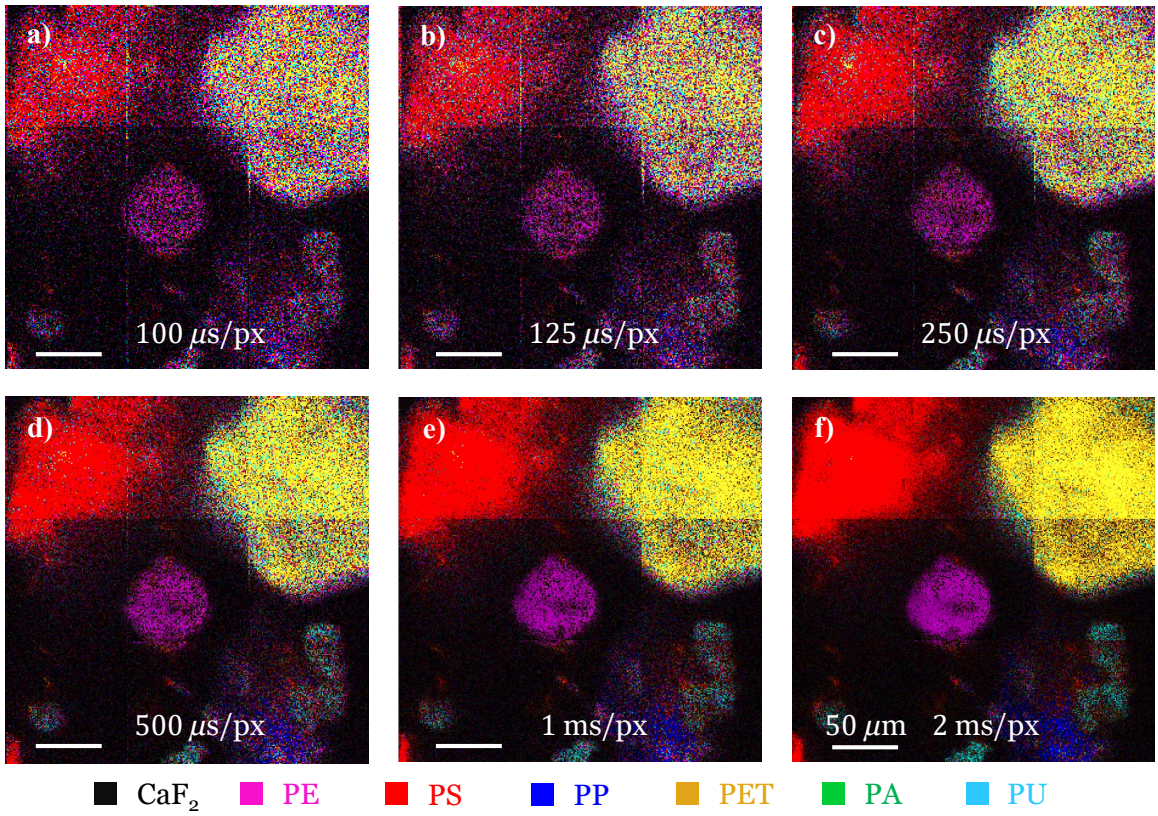

Figure 4.7: CRT image taken at different pixel dwell times. **(a)** 0.100, **(b)** 0.125, **(c)** 0.250, **(d)** 0.5, **(e)** 1 and **(f)** 2 ms/pixel/filter. FOV is 300 × 300 μm and scale bar at 50 μm.

In the six cases of figure 4.7, we can detect the different MPs. At a speed of 250 μs/px for each filter applied (Fig. 4.6(c)), it is still possible to classify the five MP species present in the imaging region. This would probably set the speed limit for this type of natural sample to access a decent signal-to-noise ratio (SNR).

Note that all the images shown in this chapter have a pixel size of 1 μm (*i.e.* all the data of each pixel of the image is exploited and where 1 pixel = 1 μm). Moreover, no other image processing (smoothing, etc.) was performed to improve the rendering of these post-processing images.

The CRT ability to map MPs at different speeds has been verified. The veracity of our results will be demonstrated in the next section, by comparing MPs displayed by CRT and the spectral information previously recorded.

4.2.3 Veracity of results

In this section, we validate the classification step performed by our CRT system on the different MPs analysed. This is possible by recording the full Raman spectra contained in each pixel (λ) (Fig. 4.8(a)). These data were obtained by performing a rapid spectral scan, using the DMD, for each estimated pure chemical species.

From the same FOV of interest (300 μm^2) and from the same sample as in figure 4.7, we were able to compare the means of the complete Raman spectra coming from pixels belonging to the same MP (i.e. having the same color) (Fig. 4.8(b)) with the reference spectra measured and shown in Figure 3.6(a) (Fig. 3.10(c)).

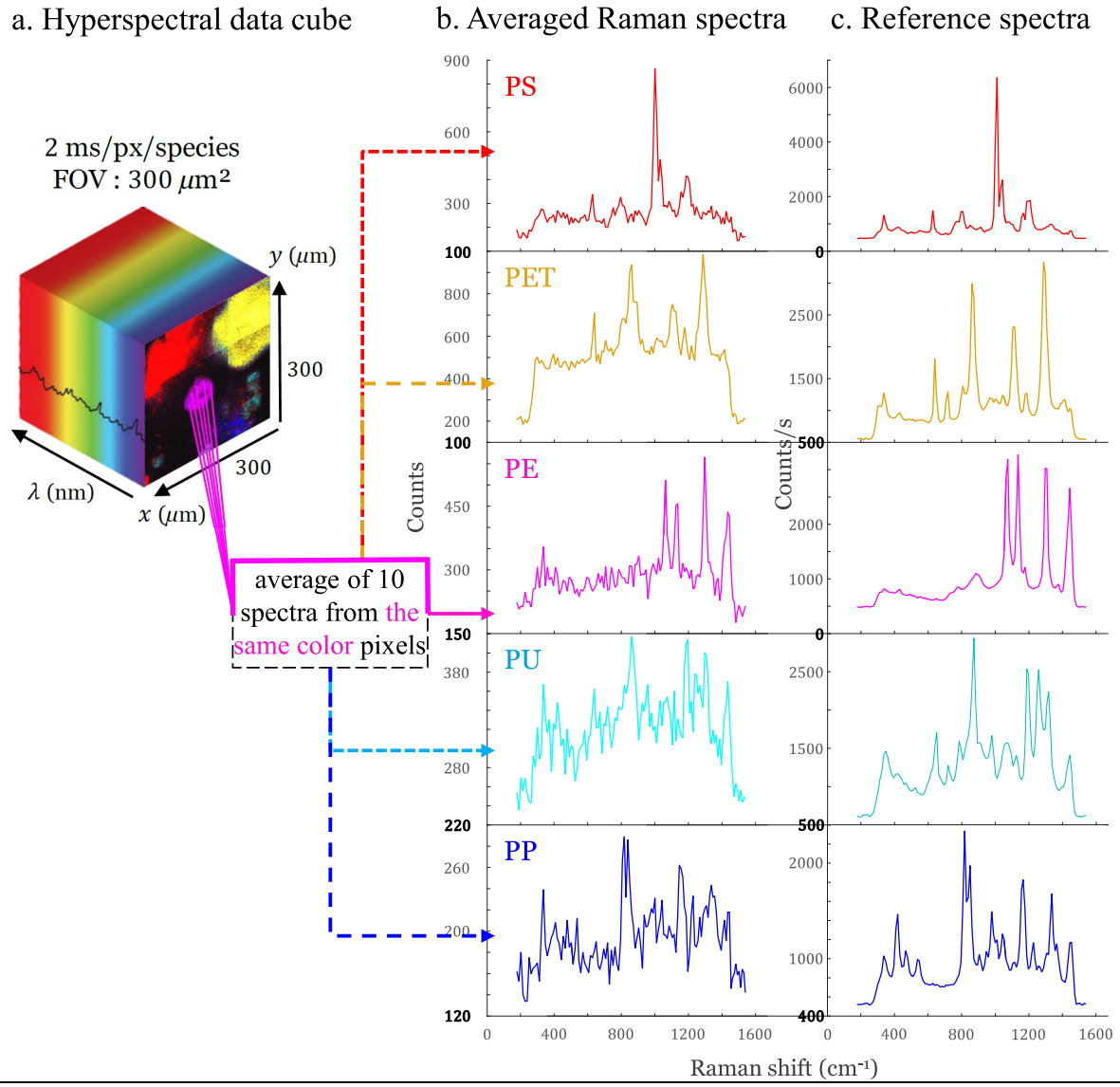

Figure 4.8: (a) Acquisition of a hyperspectral image with the DMD with a speed of 2 ms/px/species and FOV = 300 μm^2. **(b)** Averaged full Raman spectra (PS, PET, PE, PU, PP) which are obtained from ten pixels belonging to the same MP and compared **(c)** to the pure sample reference spectra (from Fig. 4.5 (b)) obtained with an integration time of 100 ms.

The acquisition of a hyperspectral image with the DMD allowed us to obtain the Raman spectra for each pixel (Fig. 4.8(a)). For better SNR and better readability, we averaged the full Raman spectra from ten pixels belonging to the same MP (*i.e.* same color) on the CRT, for each species present (Fig. 4.8(b)). The averaged Raman spectra are then compared to our reference spectra obtained with an integration time of 100 ms from pure samples.
Nicely, the classification carried out by CRT shows that the colors displayed on our images correspond to the desired species. CRT is thus able to recover the correct species of polymer from MP for each pixel.

4.2.4 CRT and conventional Raman imaging

Reference CRT image of one mm²

We used CRT to map the natural MPs on a large 1 mm² area. This surface is used as a time reference and the results obtained from it will then be used for comparison with other technologies.

To make this comparison, the same region of interest of 300 × 300 μm was kept (recognized in the white dotted square) and extended to 1 mm² (Fig. 4.9). This figure compares the CRT image quality obtained with a pixel dwell time of (a) 250, (b) 500 μs/px and (c) 1 ms/px over a 1 mm² FOV. The samples are always the same, containing a mixture of the six different mixed plastic polymers: PS, PA, PP, PE, PET and PU on a CaF_2 coverslip. A table in Fig. 4.9 gives the acquisition times for CRT imaging over 1 mm² (1) by filter applied and (2) after the application of all the filters M (where M equal to the number of species N =7). The acquisition times indicated are those obtained experimentally. Still in the table in (3), we introduce an essential parameter : the *Sampling Ratio* (SR) $\eta = {}^{A}/_{F}$ where A and F represent the number of measurements and the number of total pixels of an image, respectively [133]. This parameter introduced here will be useful to us in the following sections.

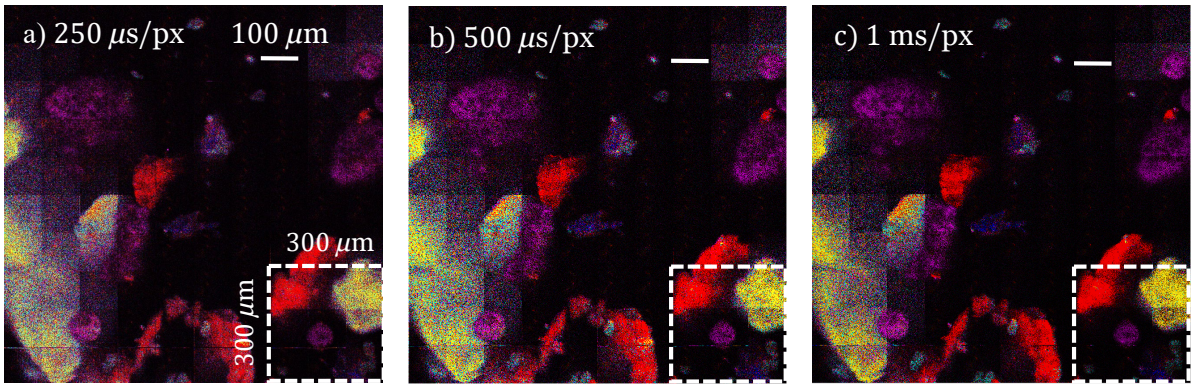

Timing / px	(1) Timing / filter	(2) $M = 7$	(3) Sampling ratio η
a) 250 μs	4 min	30 min	1
b) 500 μs	8 min	1 h 01 min	
c) 1 ms	17 min	2 h 03 min	

PET PA
PE PU
PS PP
CaF_2

Figure 4.9: CRT imaging of MPs performed on a CaF_2 coverslip, at different pixel dwell times. **(a)** 250, **(b)** 500 μs/px and **(c)** 1 ms/px for each of the seven filters applied. The scale bar is 100 μm and the FOV = 1 mm². The table below indicates according to pixel dwell time **(1)** the scan time for a filter, **(2)** the total time spent after applying all filters and **(3)** the sampling ratio (η): number measurement (1000^2) / the total number of pixels in the image (1000^2).

With a speed of ≥ 250 μs/px per filter applied and a resolution of 1 μm, our current CRT system can image 1 mm² in 4 min (for one filter). The final image is obtained after a total time of ~30 min, when all filters have been applied (Fig. 4.9(a)), with sufficient imaging quality to be able to correctly detect and identify MPs. Indeed, even if the quality of the image is not optimal with a pixel dwell time of 250 μs per applied filter, the information delivered is still readable as compared with CRT images acquired with a longer time (Fig. 4.9 (b-c)). This corroborates our results seen in figure 4.7.

Six species of MPs were expected during this mapping. However, PA was still not present in the chosen 1 mm² scan area. Despite careful mixing with unknown quantities, it remains complicated to have a FOV bringing together all the different species present in the sample.

We note that unclear areas (blurred areas, not very well drawn/characterized) are present on the three images of figure 4.9, in particular on the left part concerning the yellow part (PET). A disruptive effect had been underlined in the previous part in figure 4.6 where certain "large" MPs piece could not be fully mapped on a single z plane. This was explained by their size but also their random and non-homogeneous shape and surface roughness. This effect is also noticeable on this 1 mm² image MPs with quite large sizes (as compared to the image size) are present. We also suspect a possible superposition of this MP with another (should be PE, according to the colors displayed) on the lower z axes inducing a variation from yellow to purple color. The background noise can also explain this blurred effect since PET was found to be very noisy when recording its reference spectrum.

Finally, we have included in our table the index η which finally allows us to say that the data used on these images (Fig. 4.9) come from all the pixels present on this image (1000×1000 pixels, where 1 pixel = 1 μm).

CRT image on silicon filter

We made similar images to the previous section on the same sample composed of six different MPs polymers. However, instead of using a CaF_2 coverslip, we used a silicon filter (131675 W14 - SmartMembranes) [152]. This support has holes with a diameter of 5 μm, a depth of 463 μm and a pore spacing of 12 μm. This type of filter would be the main approach of interest in order to filter MPs in a context of micro or nano pollution analysis. Indeed, due to its material, this type of filter would guarantee sufficient transparency for the wide mid-IR of 4000 to 600 cm^{-1} [153]. Its characteristics would make it a good candidate for field application.

In order to use this new silicon support in our analysis, we measured new binary spectral filters adapted to all of our measured reference spectra including the spectrum of silicon instead of CaF_2 (Fig. 4.10(a)). Instead of directly depositing the MPs on the silicon support, we incorporated them directly into pure water. We then dragged the silicon filter directly through the aqueous medium concentrated six different MPs polymers (PE, PET, PA, PS, PU, and PP). Once the silicon filter was dragged though the sample, we left it dry in open air and the MPs found themselves naturally attached to its wall (Fig. 4.10(b)).

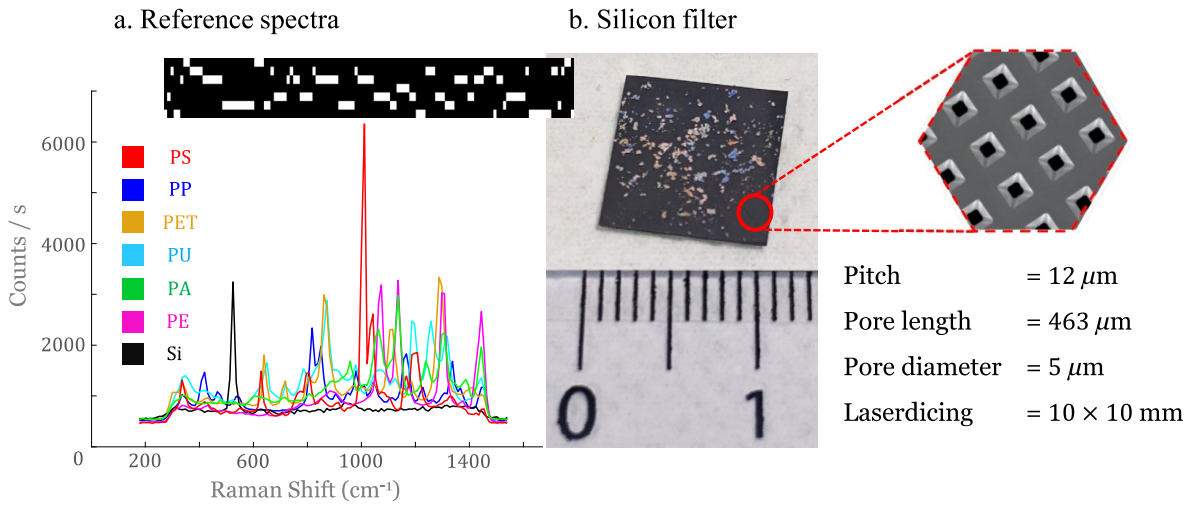

Figure 4.10: (a) Reference spectra of the different MPs polymers with that of Silicon (Si. in black) where the adapted spectral filters have been constructed. **(b)** Characteristics and picture of the silicon filter after passing it through an aqueous medium mixed with MPs.

Before discussing the CRT images of this sample, we collected and displayed two color images from the microscope camera (Fig. 4.11). Fortunately, some MPs can be discriminated by their color.
These two images were taken with two different magnification objective lenses. We zoomed from the figure 4.11(a), in the region of interest (white frame), to obtain the image Figure 4.11(b).

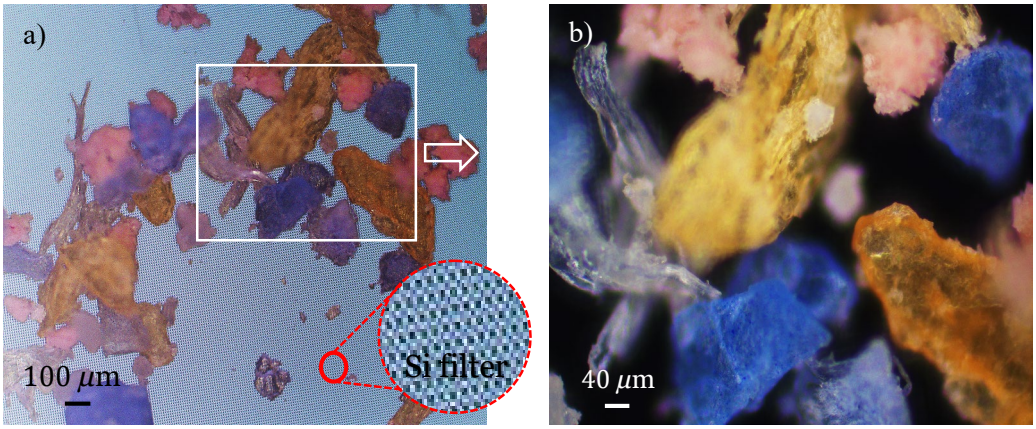

Figure 4.11: View from the microscope camera a FOV of the different MP polymers collected by a silicon substrate. In **(a)** a magnification is performed on the region of interest (white frame) to obtain **(b).**

Note that a MP analysis problem mentioned in previous sections is all the more explicit in this figure. From Fig. 4.11 it is clear that the MP samples have rough shapes and are stack on the top of each other. As noted before, imaging a single z plane with our confocal CRT setup might generate blurred areas coming from the sample surface roughness or the superposition of two MPs.

We performed CRT imaging of the Si substrate with the collected MPs. (Fig. 4.10(b)). Figure 4.12 compares the CRT image quality obtained with a pixel dwell time ranging from (a) 1 and (b) 2 ms/px for each of the seven filters applied, on 1 mm² FOV. The imaging times are indicated as well as the SR η (always equal to 1 in this case). For these experiments, the laser power was always fixed to about 60 mW at the sample plane. We present below the raw images.

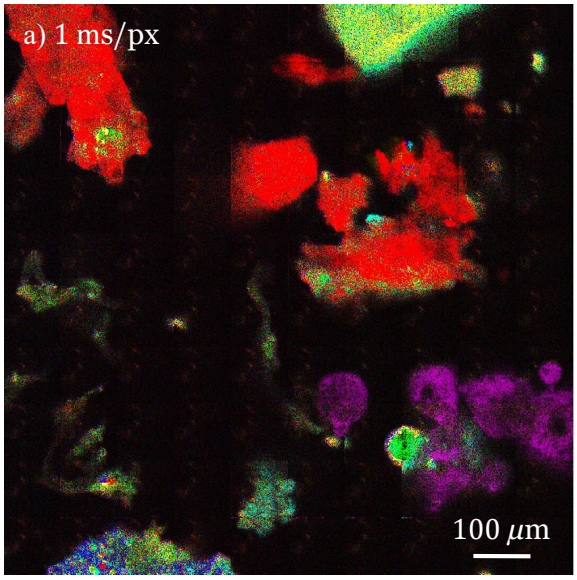

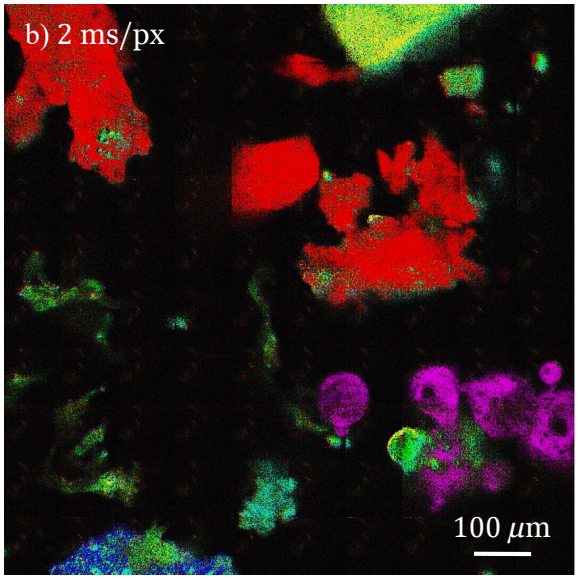

Timing / px	(1) Timing / filter	(2) $M = 7$	(3) Sampling ratio η
a) 1 ms	17 min	2 h 10 min	1
b) 2 ms	35 min	4 h 32 min	

PET PA
PE PU
PS PP
Si

Figure 4.12: CRT imaging of MPs performed on a silicon substrate, at different pixel dwell times. **(a)** 1 and **(b)** 2 ms/px for each of the seven spectral filters applied. The scale bar is 100 μm and the FOV = 1 × 1 mm. The table below indicates according to pixel dwell time **(1)** the scan time for a spectral filter, **(2)** the total time spent after applying all spectral filters and (3) the sampling ratio (η)

In figure 4.12 we have selected the speeds of 1 and 2 ms/px/filter to have superior image qualities as compared to those obtained with faster scanning speeds. These images are obtained after total acquisition times of 2 h 10 min and 4 h 32 min, respectively.

Note that in this specific case, the images present the six different MPs polymers (PP, PE, PS, PET, PU and PA) over a 1 × 1 mm FOV. Even if we observe color overlaps in some places, the detection and identification of each MPs present is correct. Image (b) is of better quality, due to the longer acquisition time. However, the area that appears to be PET at the top right of the image is blurred in (a) and (b). As already mentioned above, PET samples were already noisy when recording the reference spectra. This may justify the difficulties in obtaining a clear classification. Further explanations about this background noise and the analysis of the spectra directly measured on the samples are provided in Appendix 1.

In conclusion, the presence of MPs, their size, their identification can be analysed using CRT imaging.

Discussion

Our CRT imaging scheme is based on the mapping of an area point by point, where each point represents a pixel with a size of 1 μm (for 1 × 1 mm, 1000² of pixels and therefore 1000² of measurements, $\eta = 1$). Images with scan speeds ranging from 250 μs/pix to 2 ms/pix were shown in this chapter, reaching a total acquisition time of 30 min to 4 h 32 min for a 1 mm² total area, respectively. Detection and identification of MPs at these acquisition speeds were correctly performed.

It is interesting to compare our CRT with results reported in the literature to perform Raman imaging of MPs. To scan an 1 mm² area of a MPs sample, a time of 38 h was required by Kappler *et al.* and this despite using a distance between each scan point of 10 μm with an integration time of 10 s per point [153]. A long acquisition time but necessary for the type of sample that are MPs.
In the same paper, they reduced the integration time to 0.5 s per point (still with 10 μm spacing) and improved the focus using a topographic imaging tool. The total measurement time was reduced from 38 h to 90 min, but the increase in speed came at the expense of the detection success rate [153]. Another way to save time would be to guide the laser directly towards the microparticles of interest and perform the necessary measurements on each of them. Indeed, the major drawback of point-by-point mapping for the MPs is the time lost in scanning areas with no MP samples (CaF_2 coverslips or silicon substrates in our case). This approach was used to compare several technologies in the MP analysis embedded in an artificial soil [154]. It consists of preselected the MPs visually under the microscope in order to adjust the scanning area to each particle to be analysed in the area of interest. A pre-scan is then performed to obtain a spectral image of each particle. A sorting retains only the points of interest where the spectra have the highest resolution for each particle (and avoid fluorescent spots). This procedure enabled better results, with a time of 15 h per mm² (20 ms of integration time per point) with a much better compromise between acquisition time and detection success rate [1].

CRT is subject to the disadvantages of supervised imaging conditions. This means that we need prior information about the sample to be analysed. It is also limited by the number of species to be detected and identified. Nevertheless, concerning the problem of plastic pollution, these MPs can be diverse but there are only about ten plastic polymers. Moreover, the spectral information about these most common polymers is known. This is why CRT appears to be an optimized method for analysing MPs.
A total time ≥ 30 min of analysis would already be sufficient to have a correct detection and a correct identification of MPs on 1 mm². This time can be increased to have a higher image quality, but the desired information remains the same according to our aims "*Are MPs present ?*", "*what type are they ?*". In comparison, times of 38 h or even 15 h reported in the literature seem considerably long.

Scope for improvement

Scan area preselection can improve the scan time per frame in CRT. The scan area preselection can be performed by taking a white light image of the FOV and selecting the regions of interest (*i.e.* the MPs) where the point scanning process is launched. This would be motivated in view of the large areas without samples that are scanned without bringing any information. However, this is not part of our long-term plans because this improvement process is an undesirable practice for environmental studies but appropriate for comparison purposes [1]. Indeed, we can be interested in this approach only in the context of studying MPs on still images where we are sure to find the selected particle at the same place following the scan are preselection. In our case, we would like to push CRT to analyses of MPs directly in moving aqueous media where a pre-detection of MPs is not possible. This is part of a collaborative project with the IFREMER that will be detailed in chapter 5 of this manuscript.

Another important point should be emphasized. We have introduced from figure 4.9 a notion of Sampling Ratio (SR) note η:

$$\eta = \frac{A}{F} \tag{4.1}$$

Where A represents the number of measurements and F the total number of pixels of an image [133]. For one of our 1 mm² images (*e.g.*), where 1 pixel = 1 μm, we have $F = 1000^2$ and since a measurement is made for each pixel $A = 1000^2$, hence $\eta = 1$. This point is important because most often this SR is not indicated, in scientific papers or commercial Raman machine scanning speed.

We have varied on this index η in order to improve the measurement time on CRT images. To better understand how this sampling ratio is exploited, we used as an example the same area of interest of 1 mm² shown in the previous figure 4.14(a) shows an image with η = 1 whereas figure 4.14(b) was obtained with η = 0.5.

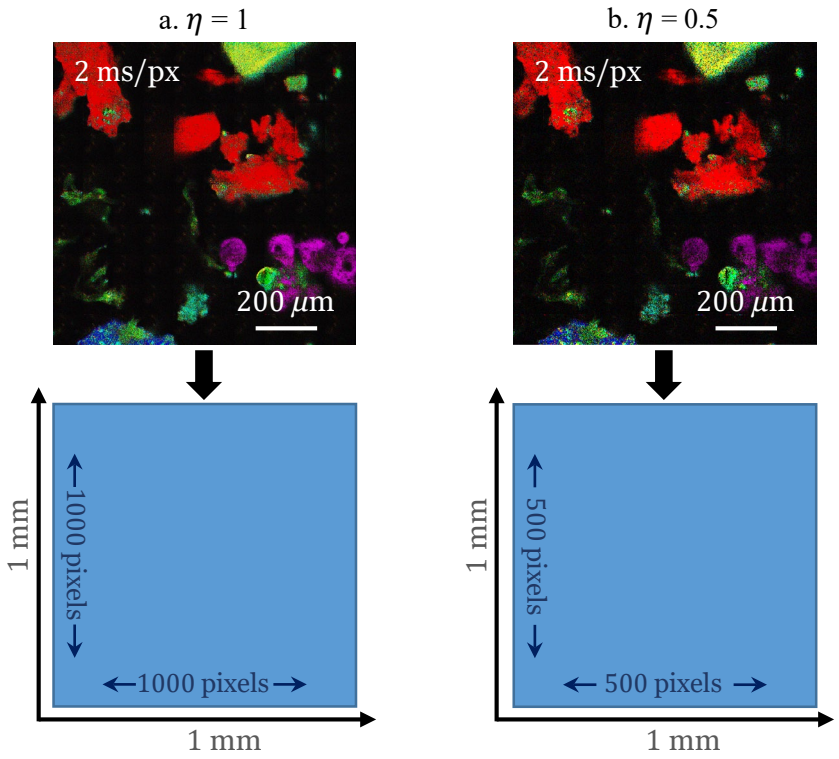

Figure 4.13: CRT image with a pixel dwell time of 2 ms/px for each filter on 1 mm² where **(a)** the measurements are made on each pixel of the image (η = 1), **(b)** the measurements are made for 1 pixel out of 2 of the image, thus collecting a total of 500² data (η = 0.5). The scale bar is 200 μm.

We can compare our different CRT images with different η (Fig. 4.14). We kept the as base speed constant at 2 ms/px on the same 1 mm² area where our six different MPs were deposited.

Figure 4.14 shows different images acquired with (1) different η, (2) the measurement corresponding time taken when applying a single spectral filter, (3) the total time needed to obtain the final image after application of all the spectral filters, (4) the pixel dwell time common to each of the images.

Note that there was no post-processing of the images shown here that the times given in the table are approximately those recorded experimentally.

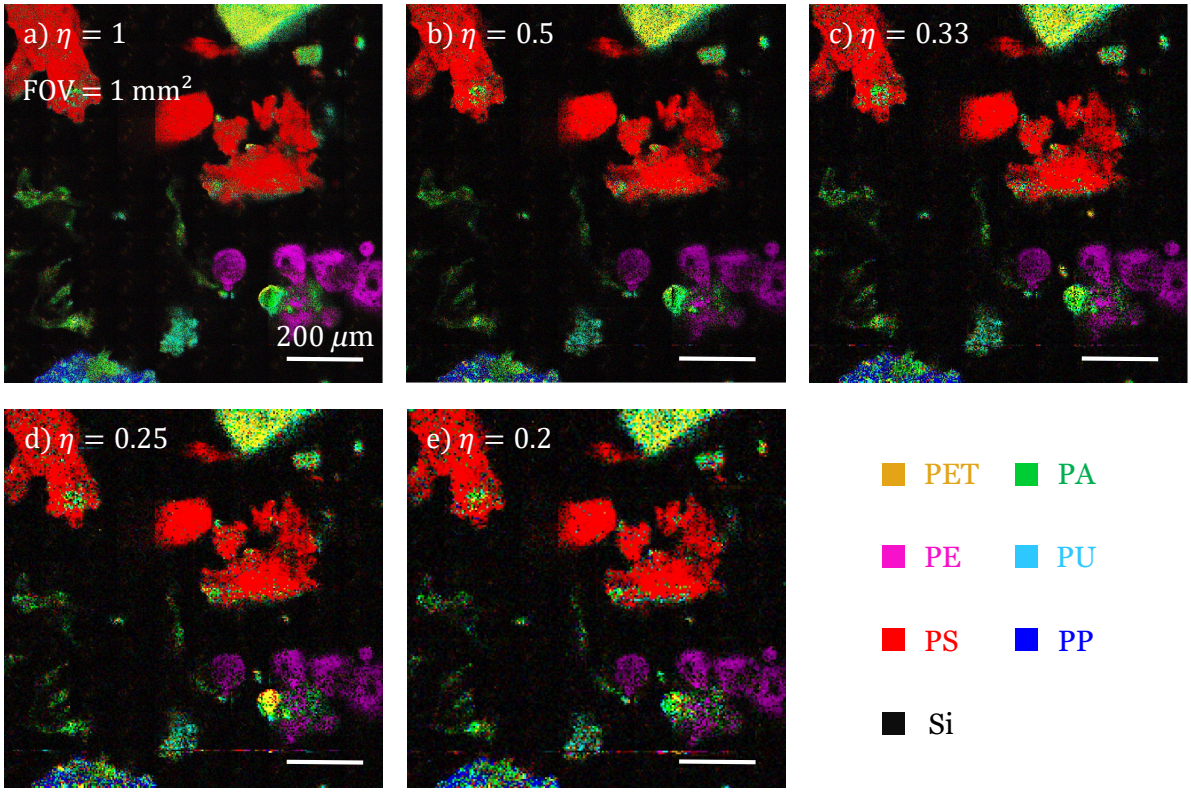

(1) Sampling ratio η	(2) Timing / filter	(3) M = 7	(4) Timing / px
a) 1	35 min	4 h 32 min	2 ms/px
b) 1/2	7 min	51 min	
c) 1/3	4 min	30 min	
d) 1/4	3 min	23 min	
e) 1/5	2 min	15 min	

Figure 4.14: CRT imaging of MPs performed on a silicon filter. The scale bar is 100 μm and the FOV = 1 × 1 mm. Each image represents a sampling ratio η of **(a)** 1, **(b)** 0.5, **(c)** 0.33, **(d)** 0.25, **(e)** 0.2. The table shows **(2)** the scan time for a filter, (3) the total time spent after applying all filters as a function of the parameters of **(1)** η and **(4)** identical pixel dwell time for each image.

For η = 1 the total image acquisition took 4 h and 32 min, the MPs are well resolved and identified Fig. 4.14(a). When we simply divide by two the number of measurements performed (η = 0.5), we gain a factor of four on the total measurement time (Fig. 4.14(b)) and the MP identification is still very good. Smaller sampling ratios were used in order to observe a limit to this approach in our case (Fig. 4.14(c-d-e-f)). Even with a η = 0.2 we observe, to a certain extent, an image where each of the MPs is correctly detected and classified. Nevertheless, we must remain cautious because we are in a case where the MPs volumes are large. We note the reducing η comes at the expense of losing the identification on the small MPs. This is all the truer is we would like to detect very small MPs with nanometric dimensions.

We have shown that the SR η is an interesting parameter to speed up CRT with a factor up to 8 (η = 0.33). This makes CRT attractive for the rapid detection of MPs in environmental studies.
In the next section, we will describe a recently funded project using CRT to detect MPs in aqueous solutions.

4.3 Conclusion

Problems encountered

The analysis of the MPs showed several obstacles. First of all, it turned out that plastic combined with additives could provide more or less noisy spectral information. Especially because these additives can color certain plastics and possibly generate a strong noise (this was the case for the black PVC).
Even if our reference spectra were correctly recorded (Fig. 4.5), and could be correctly used to designed the spectral filters there are situations where this calibration can be difficult or even impossible. This is when the samples chosen for the calibration are too different from the samples collected in the field. The literature often reports clear differences between the reference spectra of pure materials and the Raman spectra measured on MPs [1] [151]. These differences would often be due to fluorescence (or more simply to background) coming from impurities such as additives, organic particles, etc. [1].

In our study, we have taken this fluorescence background into account in our measurements and this background is part of the spectral signature for the various MPs. This was manageable and the CRT results showed that the various MPs could be nicely identified and spatially resolved, however there might be more difficult scenarios where this fluorescence background should be removed. In this case, the adoption of methods to attenuate this fluorescence background is necessary.
One method would be to look at the lifetime. Given that the lifetime of the florescence emission is longer (a few nanoseconds) than that of the Raman scattering (a few picoseconds), it is possible to perform time-gating measurements to remove part of the fluorescence [49] [50] [51]. Further information on fluorescence suppression method in Raman spectroscopy can be found in [48] .
Another simpler method, which is part of a future project, is to do further analysis on the effect that water might have the MPs fluorescent background. Indeed, analysing MPs (colored or not) directly in an aqueous medium may reduce the background noise and allow a less restrictive observation of MPs by Raman spectroscopy [155].

Another obstacle was revealed when mapping MPs. The images that have been presented in this chapter were acquired for a single z plane. In addition, MPs are not spatially homogeneous and present unpredictable shapes depending on their positioning during the measurement. A simple solution would

be to take several planes along the z axis and integrate the results to generate a single image. Such a method would minimized the imperfections attributed to the MPs surface roughnesses and shapes.
Another way, which interests us a lot, is to develop an image post-processing program that would group pixel belonging to the same MP in "macro-zones". Thus, the images could be more homogeneous and would appear of better quality.

Summary of the achievements

We have shown conclusive preliminary results of CRT for the study of MPs. The recording of the reference spectra (Fig. 4.5) allowed us to build spectral filters (Fig. 4.6(a)). These spectral filters were able to detect and identify a certain number of MPs combined with unknown additives and different colors, despite the background noise included in our measurements (Fig. 4.6(d)). We explored the CRT detection limits by scanning the MPs at different speeds and subjectively determined a scan speed limit of 250 μs/px where the MPs could still be detected and identified correctly (Fig. 4.7). The veracity of all these data could be checked on figure 4.8 where hyperspectral data showed good correlations between spectral data and MPs detected by CRT. The assigned colors were well associated with each of the spectra of the desired polymers.
These first results allowed the construction of images with a large FOV, of 1 mm² with CaF_2 coverslip (Fig. 4.9) and with silicon filters (Fig. 4.12). This step was the most important because we could show that CRT outperforms all conventional Raman technologies and can image 1mm² areas in few tens of minutes only. In addition, the use of silicon filters brings us closer to field conditions. These filters being used to concentrate the MPs in diluted liquid samples.

With similar samples and a scanning method identical to ours (point scanning), an analysis from a conventional Raman spectrometer required ≥ 15 h [1] [153]. SRS achieves an approximate scan time of 27 min per mm² [150].
Our first scan times ranged from 4 h 32 min for the longest to 30 min for the shortest to obtain a complete image over 1 mm² depending on the pixel dwell. Our results indicate that CRT appears to be a strong candidate for the detection and classification of PMs. They can be compared to the SRS speeds obtained on similar samples [150].
We then introduced the notion of sampling ratio η in our CRT imaging results (Fig. 4.13). When this parameter is modified, we achieve a x4 speed improvement and image a 1mm² MP sample in 50 min (Fig. 4.14). This major improvement will bring Raman imaging into live imaging.
Obviously, the issue of MP pollution is one where our CRT exploits all its advantages and is considered suitable and optimised.
That is to say that despite the countless difference that can exist between each type of plastic due to their added additive, there are only about ten microplastic polymers. This is perfectly suited to our CRT, which is limited by the number of species to be detected. Indeed, too many species (>20) would make

CRT non-optimal as compared to a conventional Raman spectrometer. In addition, we have enough information on the MPs system *a priori* to correctly construct our spectral filters. This further supports the advantages of CRT under supervised imaging conditions.

The results that have been demonstrated here could make CRT a serious player in the field of MP detection and identification. In addition, its low cost and simplicity, make it all the more attractive among other technologies, especially for real time field applications.

Chapter 5

Compressive Raman perspective

Contents

This fifth and final chapter shows the projects dedicated to the future use of CRT. These projects are either already underway or just being discussed.

First, they concern improvements to the technology itself for a better efficiency of application and more optimal use. Then, the use of CRT in the analysis of microplastics (MPs) proved to be very promising application and led to a joint project with IFREMER, that has just been funded. This collaborative project is a continuation of the results that were presented in the previous chapter.

5.1 Experimental technological improvement

5.1.1 Using dual detectors

In 2017, D.S. Wilcox's research group, which put forward the design of a Raman spectrometer called "OB-CD" (Optimized Binary Compressive Detection) [156] [99] [95], set out to develop a technique involving two single-pixel detectors (Fig. 5.1) [101] [96]. This is to count all the Raman photons transmitted by two optimized binary filters - the OB-CD2 strategy - allowing a more accurate and rapid estimation of the Raman scattering rates of each chemical component [101]. This was a remarkable achievement and demonstration, resulting in extremely fast Raman imaging (up to $\sqrt{2}\times$ faster, shot noice limit) rates using few photons in this supervised imaging framework [96].

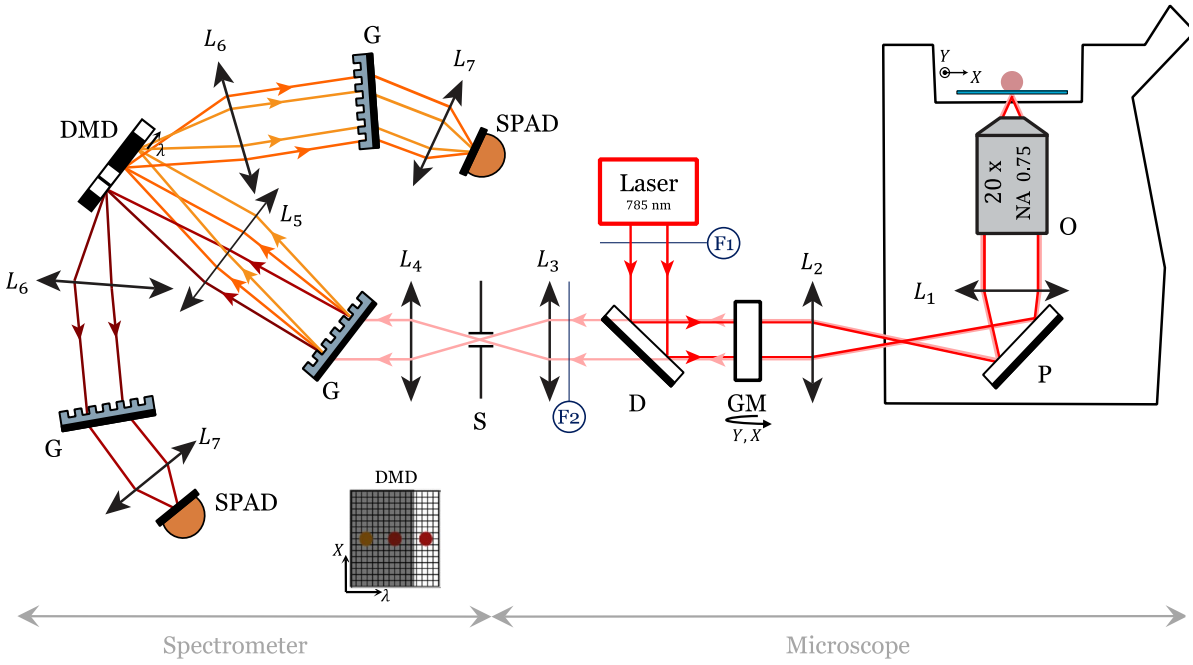

Figure 5.1: CRT experimental setup, built around a commercial microscope. O: objective, P: prism, GM: galvanometric mirrors, D: dichroic mirror, S: slit, G: grating, DMD: digital micromirror device, SPAD: single-photon avalanche photodiode, F1: laser line filter, F2: notch filter. L1: tube lens (200 mm), L2: scanning lens (50 mm), L3 − L7: achromatic doublets of focal lengths 100, 125, 100, 100, 75 mm, respectively. Illustration adapted from Scotté's thesis [23].

The use of two detectors could be an interesting way to optimise CRT. Indeed, two detectors can simultaneously collect the signal corresponding the Raman spectral filter and its complementary filter. This is because the DMD technology encodes each mirror position in only two positions +12° or -12°. Up to now we have only used the +12° position, also called ON position, to send the selected Raman photon onto the detector. At the same time and ON position is displayed on the DMD there is and OFF position (i.e. DMD mirrors at -12°) that send the complementary spectral filter in another direction. These complementary photons can be detected and their strength accounts for the total Raman signal. It

has been shown by Scotté [23] that taking into account simultaneously of the ON and OFF position photons using two detectors, increases the speed by a factor of $\sqrt{2}$ (as the speed limit to detect/identify a chemical species is ultimately limited by the detected photon number).

5.1.2 Spectral filters number optimisation

In the previous section, we discussed the possibility of using two single-channel detectors. This would reduce the measurement time by a factor of $\sqrt{2}$.

In the previous chapters, the number of spectral filters M was equal to the number of species N. Our colleagues from the Fresnel PhyTI team have recently proposed a classification scheme based on the Bhattacharya bound that we presented and used in Chapter 4 on MPs analysis [20]. This analysis method is able to work with $M < N$ since the spectral filters are not built to be optimal for a spectral species but for a combination of spectra [20]. Thus, although not demonstrated in this thesis, CRT can use fewer spectral filters than the number of species to be analysed if the direct classification method is adopted. This approach should be investigated to see to what extent we can decrease this number M in order to optimise the CRT measurement. Another method proposed by PhyTi collaborators, more ambitious and not yet put into practice, is initiated here [21] and allows to retrieve the chemical species that are not initially reference species. This is possible by using a diversity of spectral filters that are optimize to detect one single species but their diversity is large enough such that they provide all together sufficient information to retrieve an unknown chemical species. We plan to explore this interesting scheme.

5.1.3 Compact and portable CRT

We initiated the concept of making our CRT compact and easy to carry. For this purpose, we have applied this action only to our spectrometer (Fig. 5.2).

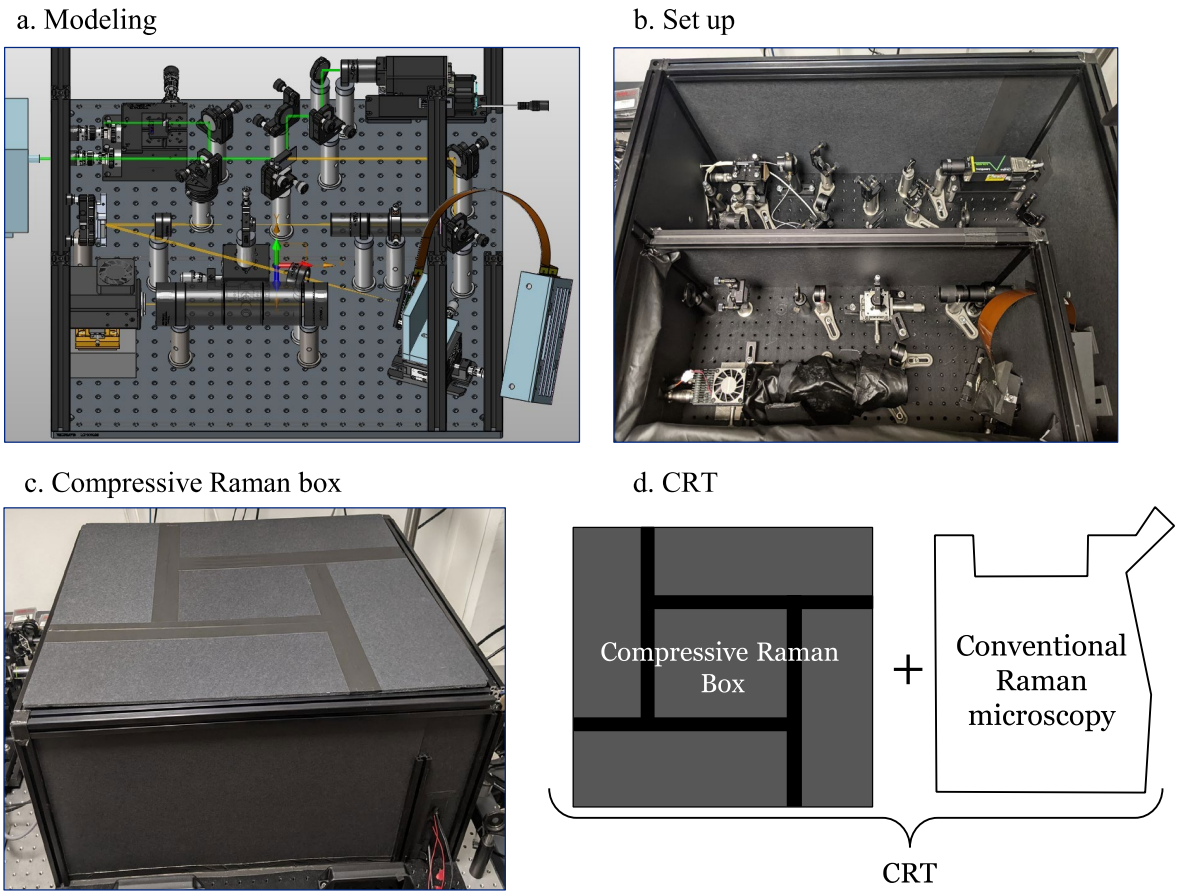

Figure 5.2: CRT experimental setup **(a)** modelled, **(b)** in its compact version, **(c)** seen from the box when closed and **(d)** diagram of the combination of a compressive Raman spectrometer with a conventional Raman microscope.

The aim is to include the CRT technology into a single box. This box could be easily added to a conventional point scanning microscope and could readily perform CRT. Figure 5.2 shows the results of our effort to develop a CRT compact system. The CRT box includes the excitation laser and the CRT spectrometer. This project has been supported by CNRS innovation as a first step towards a possible CRT commercialisation.

5.1.4 CRT using an endoscope probe

The concept of using CRT with an endoscope probe would be very interesting (Fig. 5.3). An endoscope probe would allow us to measure samples that cannot be placed under a microscope or that are simply difficult to reach. In the literature most of the Raman probes are able to work on a single point only and provide spectroscopic information but imaging is not possible. This is because the integration time is too long to get a viable Raman signal (several s). Because CRT provides more photons on the single pixel detector, it could potentially be implemented in endoscopy. Recently, the Fresnel Institute has developed a scanning endoscope probe that allows imaging at few frames per second and over a field of view of several hundreds of microns [157]. The endoscope probe is formed by a double-cladding negative curvature optical fiber. The single-mode hollow core guides the excitation laser from the proximal end of the probe up to its distal end, where the sample is located, while preserving the beam quality [158] [159].

The hollow-core mitigates the generation of parasitic Raman signal while the excitation laser is being delivered to the sample [160]. The Raman signal generated by the excitation laser in the sample plane is collected by the multimode cladding of the probe and delivered at the proximal end of the probe. A dichroic mirror splits the excitation laser that is coupled into the probe from the back propagated Raman signal that is routed towards the detectors.

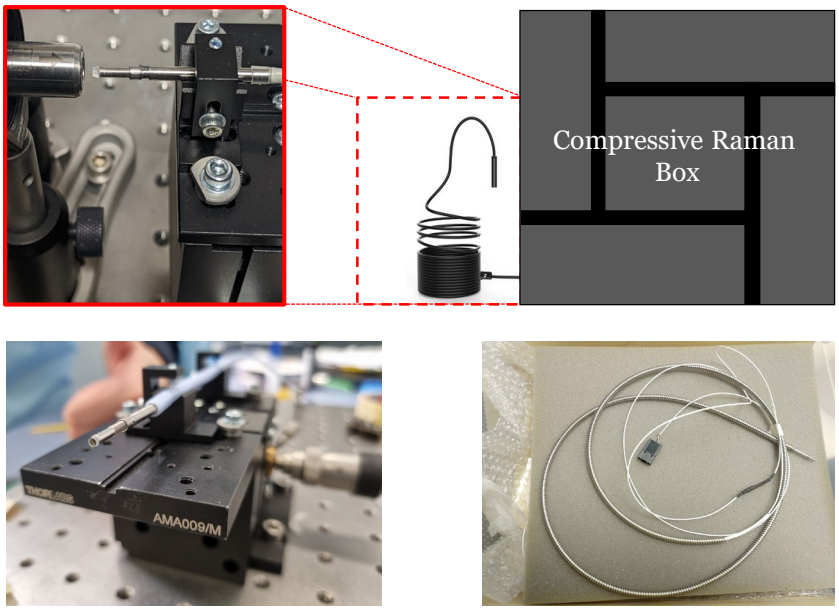

Figure 5.3: Experimental CRT box with fiber optic system

This CRT endoscope has been initiated. However, it was not possible to developed further this technology because of lack of time. The aim is to carry similar measurements as those presented in this thesis. The fiber noise (background spectral signal) will have to be separated or taken into account in our analyses according to its relation to the measured Raman signal. We will then be able to compare

the efficiency of the CRT optical fiber analysis and propose this analysis strategy from concrete results. Such technology would allow to reach samples that conventional microscopy cannot reach (e.g. such as the study of MPs in narrow water conduits, or in animal organisms).

5.2 Project M.A.R.D.I : long-term project on MPs

The Flow Analysis of Microplastics by Raman and Dielectrophoresis (MARDI) project was set up in September 2022 by the IFREMER marine ecology laboratory (LDCM - Laboratoire Détection, Capteurs et Mesures - Brest, France). It coordinates the project with our team from the Fresnel Institute as collaborators. It is in this context that we propose to use CRT to carry out rapid detection, identification and quantification of microplastics (MPs).

5.2.1 Project description

Pollution by MPs has become a major scientific and societal issue with consequences for both the environment and human health. The need to characterise and monitor this pollution requires methods that allow the counting and identification of MPs in the various matrices in order to better understand its extent. Currently, these studies remain laborious and time-consuming to implement due to the absence of an automated analysis process. In addition, the multiplication of sample handling is a potential source of contamination. The MARDI project aims to develop an innovative method for the handling and flow analysis of MPs smaller than 100 μm and will rely on knowledge in MPs characterisation and on skills in microfabrication, dielectrophoresis [161] and CRT. The objective of the project is the design of a fluidic module allowing sorting and focusing in specific areas of MPs by dielectrophoresis (DEP). The coupling with compressive Raman spectroscopy (already carried out in the IFREMER laboratory) will serve as a reference for the identification of six main polymers (PE, PET, PA, PP, PS, PVC). The use of CRT will allow a high rate of analysis. Indeed, the innovative CRT technique allows for a reduction in acquisition times by a factor of 10 to 100 (from 10 ms to several hundred μs per pixel) compared to conventional Raman spectrometers [23]. The prototypes will first be validated on bottled mineral water samples (PE, PET) before being applied to the analysis of more complex samples (seawater).

Dielectrophoresis (DEP):

The DEP technique allows the manipulation of dielectric particles with non-uniform alternating electric fields. These first induce a dipole moment in the particles, which then become sensitive to local electric field gradients [162] [163] [164].

In the first case, dielectric particles will be repelled by areas of strong electric gradient, while in the second case they will be attracted to these same areas. Typically, these areas of strong electric field gradient are located on the edges of the electrodes. Thus, by applying the right frequency under the right experimental conditions, it is possible to control the movement of even complex dielectric particles in terms of shape and structure [163] [164].

Technology development

The technological development consists in its first phase in the design of microfluidic modules allowing the circulation and the focusing in specific zones of MPs by DEP.

The dimensions of the microchannels of interest will depend on the size range of the particles to be analysed. These microfluidic devices will include electrodes around the central channel allowing the particles to be grouped together by DEP, allowing the objective lenses of the spectrometer to be focused on the areas of interest. At least one side of the microfluidic chip will be made of glass or CaF_2, a material suitable for Raman spectroscopy measurements.

The injection rates, the dimensions of the device (size of the electrodes, inter-electrode distances) as well as the frequencies and voltages to be applied will be optimised in order to concentrate the microbeads in the finest possible area without inducing too much aggregation of the particles.

The DEP module will then be coupled to a CRT spectrometer to achieve a high analysis rate (Fig. 5.4). The particle flow (a few μm/s) will be optimised so that the particle travel speed is less than the minimum spectral acquisition time.

A specific support will be designed to have a surface perpendicular to the working objective where the flow will pass in order to allow the injection of fluids into the module. The spatial scanning system of the sample (galvanometric mirrors - point by point) will allow us to collect the Raman signal at several points of the sample as it moves through the fluid channel. This will allow us to map the sample to access the shape and size of the MPs it contains, in addition to the desired spectral information.

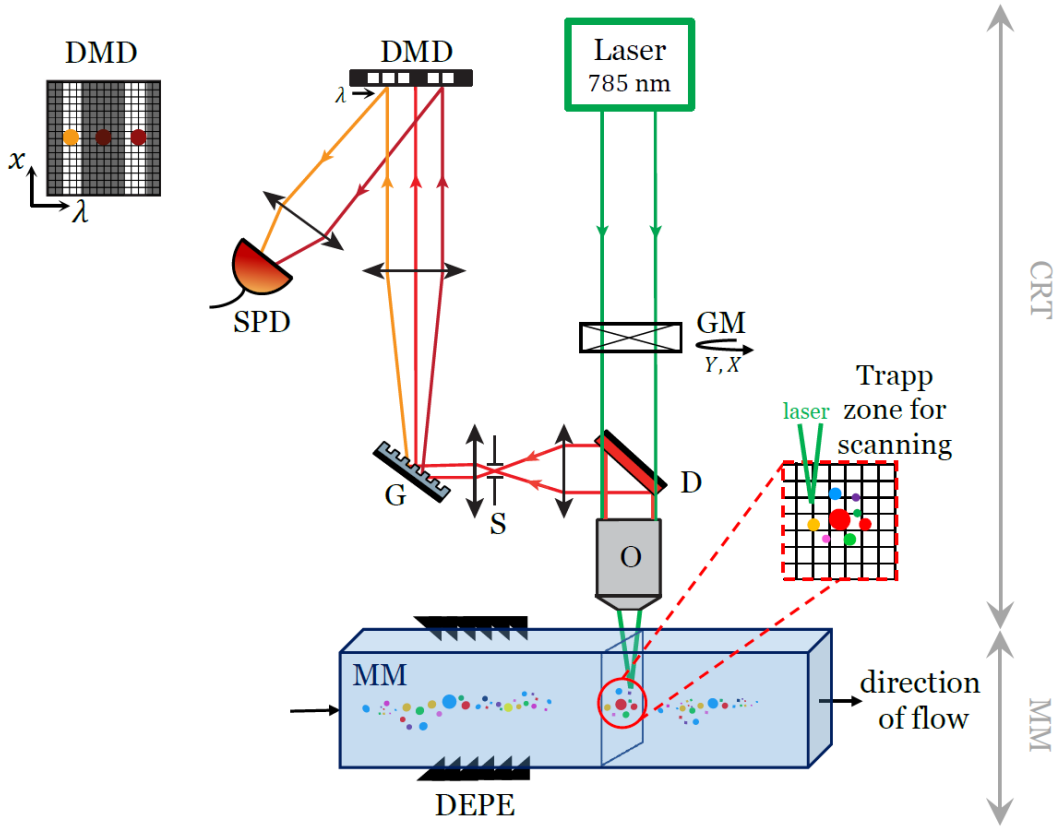

Figure 5.4: Coupling of the fluidics module with CRT for the mapping of MPs directly from a moving liquid medium. GM, mirror galvanometric; D, dichroic mirror; O, objective lens; MM, microfluidic modules; DEPE, dielectrophoresis electrode S, slit; G, grating; DMD, digital micromirror device; SPD, single pixel detector.

5.2.2 Expected impact of the project on health and environment

The system proposed in MARDI will allow the identification in flow of small MPs from various matrices (food, environmental, etc.), it will lead to a significant saving of time and thus to an increased capacity of the number of analyses. In addition, it will reduce the handling of samples and their contact with the laboratory environment and thus greatly reduce the risk of contamination.

The MARDI fluidic module incorporating CRT therefore paves the way for the development of a real-time observation system for low-level water such as drinking water and can then be directly applied to the monitoring of food and drink entry points to ensure the use of uncontaminated drinking water. In parallel, the MARDI project is the first brick in the development of an autonomous marine sensor for in situ PM analysis. This type of sensor is needed, for example, to improve the understanding of the vertical transport of MPs by allowing the acquisition of continuous concentration profiles; or the temporal evolution of the MPs concentration of waters used for aquaculture during short intervals over long measurement periods. This type of measurement is essential for understanding the interaction between organisms and MPs. Thus, the MARDI project will ultimately contribute to the monitoring of MPs

pollution and to the assessment and understanding of the behaviour and ultimate fate of plastics in the environment and consequently the impact of MPs on the environment and human health.

5.3 Conclusion

Throughout this thesis, many (new) projects have been added to the original plan. The ones described in this chapter are the most concrete and have already been initiated or discussed at length with our collaborators.

Approaches have been proposed to improve the performance of CRT. This is done by decreasing the number of measurements, previously limited by the number of species to be analysed in a sample. Firstly, experimentally, using the so-called "OB-CD2" technology initially used by Wilcox and his collaborators [156] [99] [95]. The principle is to use two detectors in order to optimise the use of the binary mask, thus sending the information to the first or second detector. This allows gain a factor of two in the measurement time.
Another strategy is to exploit a direct classification step (defined and used in Chapter 4), developed by our collaborators at the Fresnel institute [20] [21]. Indeed, this classification based on the Bhattacharyya bound is able to use a number of spectral filters lower than the number of species to be analysed [20]. This is because our spectral filters are each constructed from the combination of spectra and not with respect to a single species [20]. We should exploit these approaches and benchmark them.

From a practical point of view, the idea of making CRT compact and transportable is above all a strong argument for CRT to be a candidate of choice in analyses that need to be done directly in the field.

Finally, the MARDI project, which received funding in September 2022, represents the major future of CRT in the framework of this thesis. Developed by the IFREMER laboratory, this project aims to provide real-time analysis of a moving sample for rapid detection and identification of PMs. This is achieved by using CRT as an analytical tool, putting to use its good adaptability and performance for this type of analysis (demonstrated in Chapter 4). CRT also has a great potential for improvement that should impact this collaborative project with concrete ambitions in the environmental field.

Conclusion

During the three years of my thesis, I investigated ways to efficiently perform spontaneous Raman imaging by accelerating not only the measurement, but also the whole data flow. This was done by developing and applying the Compressive Raman Technology (CRT) to concrete applied projects, initially initiated by the previous PhD [23]. *The constraints imposed by this new approach were taken into account (a priori information, experimental noise and specific application technology) in order to apply CRT in the best conditions.*

The underlying mechanisms and important notions of spontaneous Raman scattering have been presented in this manuscript. We have seen that the Raman effect relies on the interaction of light with matter. It provides the specific signature, a "spectral fingerprint", of the vibrations of a molecule in a label-free and non-destructive way [8]. The classical method of Raman signal acquisition results in a hyperspectral image with two spatial dimensions (x, y) and one spectral dimension (λ). This recording is post-processed to obtain the final spectral images using chemometrics tools. This workflow is based on a slow acquisition rate, followed by a post-processing step. We have highlighted the need to improve this approach due to its long acquisition times and excessively large datasets generated.
Several alternative techniques have been presented to overcome these limitations. None of them presented convincing results increasing the complexity and price of the technology [122] [132].

Concerning the data generated by hyperspectral imaging, they are always compressible [12] [13]. We have presented recent theoretical and technological progresses allowing not only to better compress the data after acquisition, but also to apply this compressibility further upstream to acquire less data. This is to achieve faster and smaller acquisitions in terms of occupied memory [14] [12] [15]. Under certain conditions, this paradigm can go further: the acquisition process can be modified so that partial processing is carried out directly in the hardware [16] [17]. We have applied the latter enhancement concept to Raman hyperspectral imaging. This was done using a CRT-based imaging method. Its use allows us to overcome the limitations of conventional Raman in terms of speed and storage. Unlike commercial devices that record the full Raman spectrum on an array detector, we have shown that CRT combines specific Raman lines and detects them with a fast single-pixel detector. CRT has been shown to image Raman × 10 × 100 times faster than conventional EMCCD and CCD Raman systems [18].
We have shown that the spectral components are selected (i) numerically with an optimisation procedure that minimises the estimation variance, and (ii) physically with a programmable optical filter (digital micromirror device (DMD, [15]). This programmable optical filter is located in the spectral plane of a spectrometer [18]. The technology is accompanied by a suite of algorithms that define the optimal masks

to detect and identify known chemical species and recover their proportions [115] [101] [19]. Thus, the technique aims to achieve substantial speed-up and massive reduction in the amount of data generated. The only latency required is the design of the spectral masks for the DMD, through a calibration step at the beginning of the study. However, this time is negligible considering the total imaging acquisition time. Furthermore, this new approach using CRT requires a priori knowledge of the system under study in order to correctly program the spectral filters. Although in many study cases we already know which species are present in the samples, in which case CRT is optimal for the application. The compressive Raman imaging framework is most useful when several experiments with the same type of chemicals and the same target are conducted [96].

Under these conditions, we subjected CRT to two concrete studies in order to discuss the results and compare them with the literature.

In the first study, we used CRT to map chemical compounds in compact pharmaceutical tablets among which two polymorphs show very similar Raman spectra. This was a major challenge for our system based on binary spectral filters. The ability of the CRT to estimate the chemical proportion of each polymorph and excipient at each pixel was successfully demonstrated. Furthermore, to image 1 mm² of a pharmaceutical tablet with a resolution of 1 μm, conventional Raman imaging results in over night acquisition time (> 25 hours with 0.1 s per pixel) [131]. CRT is able to map a comparable image of the same size in 45 min.

Our second study applied CRT to an environmental project concerning plastic pollution. The aim of the project was to rapidly detect and identify microplastics (MPs). This challenge was particularly interesting due to the high background noise generated by MPs and its various additives that we took into account in our measurements. We showed conclusive results where CRT was able to correctly discriminate the different MPs with scan times per pixel of 250 μs. The literature indicates that for a mapping of MPs with an area of 1 mm², a conventional Raman spectrometer would require a measurement time of 38 h with good detection quality [153]. Under the same conditions, CRT can achieve a total acquisition time of 30 min.

These two studies, which were described in two separate chapters, met the necessary conditions for the use of CRT. Clearly, we were able to demonstrate that our technology was relevant to both projects. The results that have been demonstrated make CRT a strong contender in these two application areas.

It was only in the MPs stage that we introduced and applied improvements to this compressive imaging technique. First, we proposed a new numerical approach to applying the filters. Instead of going through an estimation step, a direct application of classification was applied to tailor the measurement to a fast detection and identification demand [20]. Although this generated a lower data flow, the time saving was negligible.

The sampling ratio (η) parameter was also introduced in our CRT imaging results. This parameter indicates the number of measurements that have been performed on an image compared to the total number of pixels present in the measurement area. By decreasing this value in our measurements, we have shown that it is possible to decrease the measurement times by at least a factor of four. For example, with a spacing of 2 μm per measurement, an image of 1 mm² in MPs analysis required less than 10 min. Therefore, for further CRT operations, this parameter will have to be seriously considered in order to properly use the full potential of this technology.

Finally, we have projected CRT into a readable future. We have described future plans for optimisation and technological improvements. This is to argue further for the use of CRT in the application areas. These projects aim to improve the performance of CRT by, for example, reducing the number of spectral filters required in relation to the number of species analysed [20] or by optimising the measurement with two detectors [101]. All of this makes it possible to speed up not only the measurement, but also the entire data flow. The practicality of using CRT was also emphasised. Making CRT compact and transportable or combining it with an endoscopic probe further highlights the possible improvements for use in samples that are difficult to access.

The results and plans I have been able to put forward during this thesis show the performance and potential of CRT for faster, cheaper and more efficient Raman imaging. These arguments encourage further exploration and improvement of this technology.

Annex

This annex aims to detail the difficulties that were encountered in Chapter 4, when analysing the MPs in their early stages. Several assumptions were made and solutions were provided and demonstrated in this annex.

The two classification methods are performed and compared in order to understand why a more direct classification method is more appropriate for the study. We will see however that the noise generated by the colored plastics causes a real problem for the analysis of the Raman signal. A new design of the spectral filters will be studied and applied in order to be able to carry out our measurements in the best conditions while taking into account the background noise.

This appendix thus provides additional information on the selected parameters.

Background noise

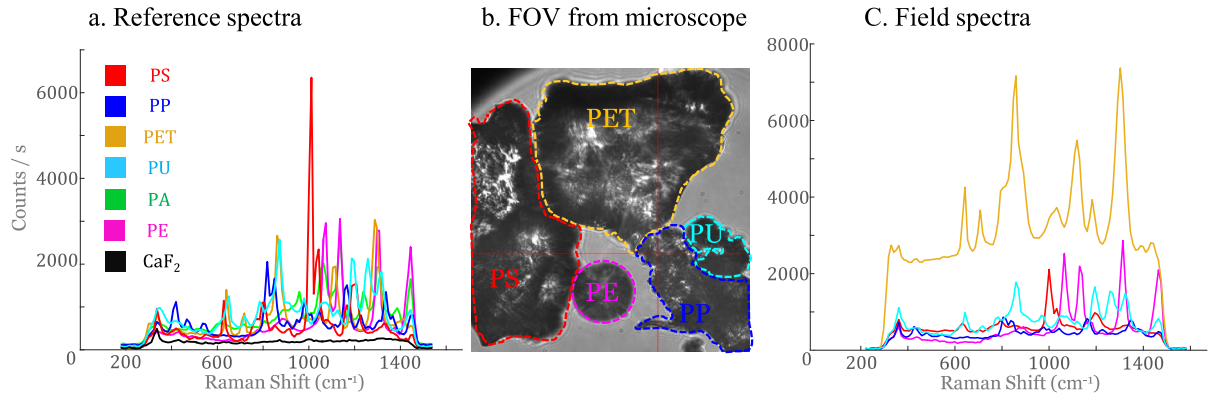

Figure A.1: **(a)** Reference spectra and associated binary filters. **(b)** FOV seen from the microscope where the different plastic polymers are known. **(c)** Averaged spectra from the sample.

Our reference spectra were measured (Fig. A.1(a)) and binary spectral filters were constructed. The analysis was carried out in a FOV where each MP has already been identified to ensure the presence of several types of MPs (Fig. A.1(b)).

In Figure A.1(c), we have shown what is directly measured spectrally on the sample, from the colored MPs present (PET, PS, PE, PP, PU). Each spectrum represents a spatial average of five spectral measurements made on the different areas outlined in Figure A.1(b).

This last figure represents how the Raman signal is captured during our measurements. The PET spectrum (in yellow) clearly shows the presence of background noise. This noise is much more present than during the recording of the reference spectra. We provide the best possible conditions for recording the reference spectra (pure sample, uncolored, etc.) which explains this difference.

CRT image from (i) Direct Classification or (ii) Estimator-based Classification

From this FOV (Fig. A.1(b)), we made two CRT images with two different methods (Fig.A.2). The two analysis methods are (a) a classification based on a proportion estimation step (used in Chapter 3) and (b) a direct application of the classification (used in Chapter 4). These two methods are detailed at the end of Chapter 2. The direct classification method is also detailed at the beginning of Chapter 4.

a. Estimation + Classification

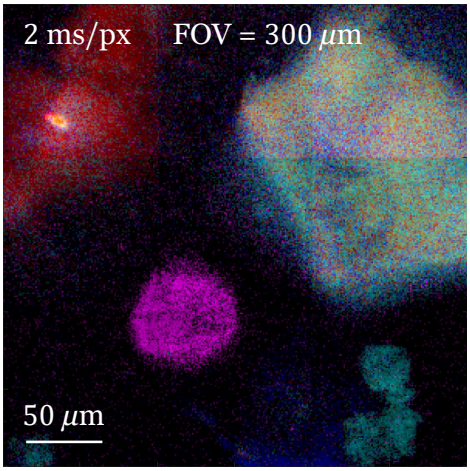

b. Classification

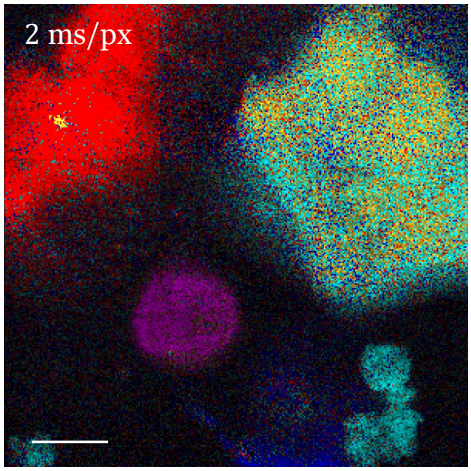

Figure A.2 : CRT image made from **(a)** the estimator-based classification **(b)** a direct classification - The scale bar is 50 μm and the FOV = 300 × 300 μm.

It is clearly seen that both techniques can be used. In this sense, they correctly detect the different MPs present and some are even correctly identified with the two approaches. The PET remains the only unidentifiable chemical species. Our PET sample turned out to be the one producing the most background noise in its spectral data as seen in Figure A.1(c). This may explain the difficulty of our two methods to correctly identify (in yellow) this species.

A difference in intensity is visible between the two images. The data contained in the pixels of each image differs depending on the method applied. In (a) each pixel contains a number of photons for each species, since the model considers a possible mixture of species in one pixel. However, it is the dominant species (the one that collected the most photons when all masks were projected) that is displayed in the final image. In (b), the model is summarised as follows: one pixel = one species. Since it is assumed that there is a single species, we weight the color of each pixel by the total number of photons received on the pixel for all projections of the different spectral filters. Indeed, since in this case all photons are assumed to come from the single species of the pixel.

Non-orthogonal vs. orthogonal filters

Another way to improve the identification of MPs is to modify the filter construction step. In the calibration stages up to the application of CRTs for the mapping of pharmaceutical tables, non-orthogonal spectral filters were used (Fig. A.3(a)).

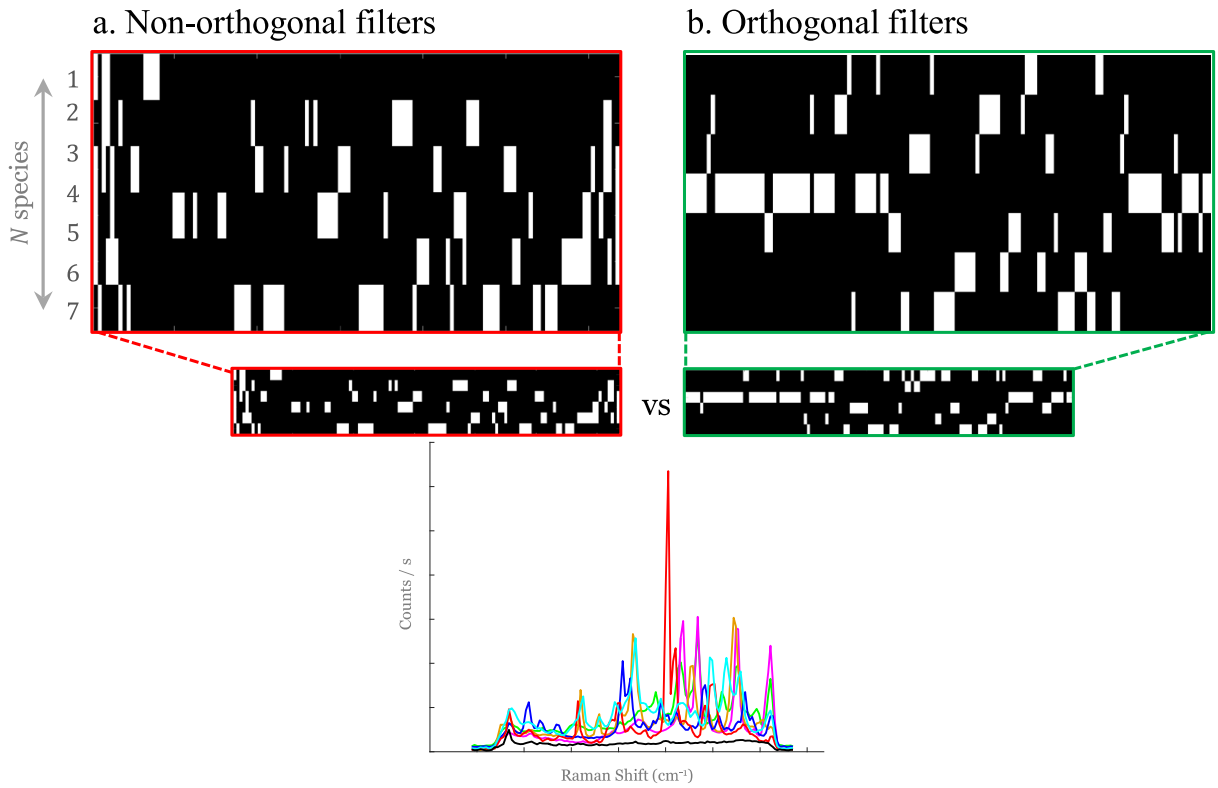

Figure A.3: Combination of **(a)** Orthogonal and **(b)** non-orthogonal spectral filters, adapted to the set of spectra of the different MP polymers referenced.

Non-orthogonality allows the different spectral filters to share one or more spectral regions where photons are selected and directed to the detector. This allows for a greater number of possible combinations of optimal filters for the set of reference spectra (refractor). Moreover, this parameter played its role correctly in the analysis of the pharmaceutical tablets where the two forms of polymorphs were well discriminated.

This parameter was modified for the analysis of MPs. A reconstruction of the spectral filters was performed using orthogonal filter projections. These orthogonal filters no longer allow to have identical spectral ON (white) pixel. In other words, a spectral pixel that is activated for one filter cannot appear in any other filter. These projections were performed on the same FOV of interest with the same parameters (Fig. A.4).

a. Estimation + Classification

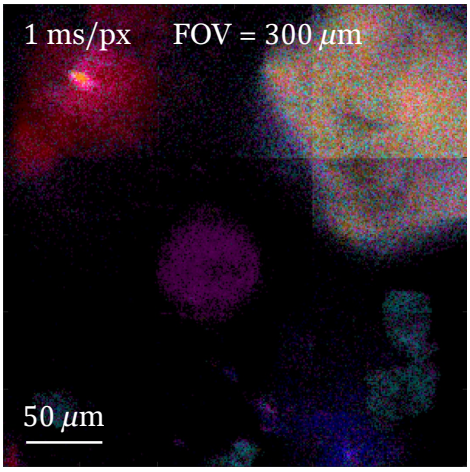

b. Classification

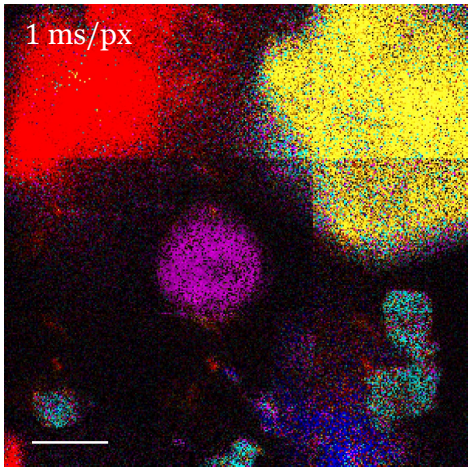

Figure A.4: CRT image made from **(a)** the classification based on the estimator **(b)** a direct classification, under the orthogonal mask projection - The scale bar is 50 μm and the FOV = 300 × 300 μm.

The application of orthogonal spectral filters (Fig. A.4) shows clear differences from the application of non-orthogonal filters (Fig. A.2). This difference is particularly visible with the identification of PET, which is very distinguishable.

It seems that orthogonality allows for a "stricter" discrimination for samples such as MPs which are very noisy. Further analysis should be provided to understand why these results are obtained.

Applying the classification step without going through an estimation step tends to give better imaging results with CRT.

Therefore, all our analyses and results in Chapter 4 concerning MPs are based on the parameters defined in Figure A.4.

Abbreviations

BB	Bhattacharyya bound
CARS	Coherent Raman anti-stock
CDD	Charge-coupled device
CRB	Cramer Rao lower bound
CRT	Compressive Raman technology
CSRS	Coherent Stock Raman scattering
CS	Compressive sensing
DMD	Digital micromirror device
EMCCD	Electron multiplying charge coupled device
FRS	Full Raman spectrum
FOV	Field-of-view
InGaAs	Indium gallium arsenide
IR	Infrared
MAN	Mannitol
MSE	Mean square error
MTF	Modulation transfer function
NA	Numerical aperture
NIR	Near infrared
PA	Nylon
PE	Polyethylene
PEG	Polyethylene glycol
PET	Polyethylene terephthalate
PMMA	Poly-(methyl methacrylate)
PP	Polypropylene
PS	Polystyrene
PSF	Point spread function
PU	Polyurethane
PVC	Polyvinyl chloride
Si	Silicon
SLM	Spatial light modulator
SNR	Signal-to-noise ratio
SPD	Single pixel detector
SR	Sampling Ratio

SRG	Stimulated Raman gain
SRL	Stimulated Raman loss
SRS	Spontaneous Raman scattering
STA	Starch

Bibliography

[1] C. F. Araujo, M. M. Nolasco, A. M. P. Ribeiro, et P. J. A. Ribeiro-Claro, « Identification of microplastics using Raman spectroscopy: Latest developments and future prospects », *Water Research*, vol. 142, p. 426-440, oct. 2018, doi: 10.1016/j.watres.2018.05.060.

[2] A. Germond *et al.*, « Raman spectroscopy as a tool for ecology and evolution », *Journal of The Royal Society Interface*, vol. 14, n° 131, p. 20170174, juin 2017, doi: 10.1098/rsif.2017.0174.

[3] E. S. Allakhverdiev *et al.*, « Raman Spectroscopy and Its Modifications Applied to Biological and Medical Research », *Cells*, vol. 11, n° 3, p. 386, janv. 2022, doi: 10.3390/cells11030386.

[4] C. V. Raman et K. S. Krishnan, « A New Type of Secondary Radiation », *Nature*, vol. 121, n° 3048, Art. n° 3048, mars 1928, doi: 10.1038/121501c0.

[5] D. A. Long, *The Raman Effect: A Unified Treatment of the Theory of Raman Scattering by Molecules*. Chichester ; New York: Wiley–Blackwell, 2002.

[6] A. Smekal, « Zur Quantentheorie der Streuung und Dispersion », *Z. Physik*, vol. 32, n° 1, p. 241-244, déc. 1925, doi: 10.1007/BF01331666.

[7] G. S. Landsberg et L. I. Mandelstam, « New phenomenon in scattering of light », *Journal of the Russian Physico-Chemical Society*, vol. 60, p. 335, 1928.

[8] W. Demtröder, *Laser Spectroscopy*, Laserspect edition., vol. 1. Berlin, Heidelberg: Springer Berlin Heidelberg, 2008. doi: 10.1007/978-3-540-73418-5.

[9] J. P. Nolan et D. S. Sebba, « Chapter 20 - Surface-Enhanced Raman Scattering (SERS) Cytometry », in *Methods in Cell Biology*, vol. 102, Z. Darzynkiewicz, E. Holden, A. Orfao, W. Telford, et D. Wlodkowic, Éd. Academic Press, 2011, p. 515-532. doi: 10.1016/B978-0-12-374912-3.00020-1.

[10] G. Panczer, D. Ligny, C. Mendoza, M. Gaft, et X. Wang, « Raman and fluorescence », 2022. doi: 10.1180/EMU-notes.12.

[11] J.-X. Cheng et X. S. Xie, *Coherent Raman Scattering Microscopy*, 1er édition. Boca Raton: CRC Press, 2012.

[12] E. J. Candes et B. Recht, « Exact low-rank matrix completion via convex optimization », in *2008 46th Annual Allerton Conference on Communication, Control, and Computing*, sept. 2008, p. 806-812. doi: 10.1109/ALLERTON.2008.4797640.

[13] N. Gillis, « The Why and How of Nonnegative Matrix Factorization », in *Regularization, Optimization, Kernels, and Support Vector Machines*, Chapman and Hall/CRC, 2014.

[14] E. J. Candès, « Compressive sampling ». 2006.

[15] D. Dudley, W. M. Duncan, et J. Slaughter, « Emerging digital micromirror device (DMD) applications », in *MOEMS Display and Imaging Systems*, janv. 2003, vol. 4985, p. 14-25. doi: 10.1117/12.480761.

[16] S. E. Bialkowski, « Species discrimination and quantitative estimation using incoherent linear optical signal processing of emission signals », *ACS Publications*, 1 mai 2002. https://pubs.acs.org/doi/pdf/10.1021/ac00125a043 (consulté le 3 octobre 2022).

[17] N. T. Quyen, M. D. Jouan, N. Q. Dao, E. D. Silva, et D. A. Phuong, « New Raman Spectrometer Using a Digital Micromirror Device and a Photomultiplier Tube Detector for Rapid On-Line Industrial Analysis. Part II: Choice of Analytical Methods », *Appl. Spectrosc., AS*, vol. 62, n° 3, p. 279-284, mars 2008.

[18] C. Scotté *et al.*, « Assessment of Compressive Raman versus Hyperspectral Raman for Microcalcification Chemical Imaging », *Anal. Chem.*, vol. 90, n° 12, p. 7197-7203, juin 2018, doi: 10.1021/acs.analchem.7b05303.

[19] P. Réfrégier, C. Scotté, H. B. de Aguiar, H. Rigneault, et F. Galland, « Precision of proportion estimation with binary compressed Raman spectrum », *Journal of the Optical Society of*

America. A Optics, Image Science, and Vision, vol. 35, n° 1, 2018, doi: 10.1364/JOSAA.35.000125.
[20] P. Réfrégier et F. Galland, « Bhattacharyya bound for Raman spectrum classification with a couple of binary filters », *Opt. Lett., OL*, vol. 44, n° 9, p. 2228-2231, mai 2019, doi: 10.1364/OL.44.002228.
[21] T. Justel, F. Galland, et A. Roueff, « Compressed Raman method combining classification and estimation of spectra with optimized binary filters », *Opt. Lett., OL*, vol. 47, n° 5, p. 1101-1104, mars 2022, doi: 10.1364/OL.447769.
[22] H. Rigneault et P. Berto, « Tutorial: Coherent Raman light matter interaction processes », *APL Photonics*, vol. 3, n° 9, sept. 2018, doi: 10.1063/1.5030335.
[23] C. Scotté, « Spontaneous Compressive Raman technology: developments and applications », Theses, Université d'Aix-Marseille, 2020. Consulté le: 11 juillet 2022. [En ligne]. Disponible sur: https://tel.archives-ouvertes.fr/tel-03183047
[24] R. S. Das et Y. K. Agrawal, « Raman spectroscopy: Recent advancements, techniques and applications », *Vibrational Spectroscopy*, vol. 57, n° 2, p. 163-176, nov. 2011, doi: 10.1016/j.vibspec.2011.08.003.
[25] H. Bowley, D. Gradiner, et D. Gerrard, « Practical Raman spectroscopy », 1989. https://scholar.google.com/scholar_lookup?title=Practical%20Raman%20spectroscopy&publication_year=1989&author=Bowley%2CHJ&author=Gardiner%2CDJ&author=Gerrard%2CDL (consulté le 20 juillet 2022).
[26] J. J. Bohning, American Chemical Society, Division of the History of Chemistry, American Chemical Society, et Office of Public Outreach, *The Raman effect: Jadavpur, Calcutta : an International Historic Chemical Landmark, December 15, 1998*. Washington, D.C.: American Chemical Society, 1998.
[27] L. Saul, « IR Versus Raman - The Advantages and Disadvantages », *AZoOptics.com*, 2 février 2018. https://www.azooptics.com/Article.aspx?ArticleID=1291 (consulté le 13 juillet 2022).
[28] M. Trampuž, D. Teslić, et B. Likozar, « Process analytical technology-based (PAT) model simulations of a combined cooling, seeded and antisolvent crystallization of an active pharmaceutical ingredient (API) », *Powder Technology*, vol. 366, p. 873-890, avr. 2020, doi: 10.1016/j.powtec.2020.03.027.
[29] J. Cabannes et R. Aynard, « Étude expérimentale et théorique sur le spectre Raman de l'eau de cristallisation dans le gypse », *J. Phys. Radium*, vol. 3, n° 8, p. 137-145, 1942, doi: 10.1051/jphysrad:0194200308013700.
[30] R. L. Wehling, « Infrared Spectroscopy », in *Food Analysis*, S. S. Nielsen, Éd. Boston, MA: Springer US, 2010, p. 407-420. doi: 10.1007/978-1-4419-1478-1_23.
[31] T. Hirschfeld et B. Chase, « FT-Raman Spectroscopy: Development and Justification », *Appl. Spectrosc., AS*, vol. 40, n° 2, p. 133-137, févr. 1986.
[32] S. S. Saleem, « Infrared and Raman spectroscopic studies of the polymorphic forms of nickel, cobalt and ferric molybdates », *Infrared Physics*, vol. 27, n° 5, p. 309-315, sept. 1987, doi: 10.1016/0020-0891(87)90072-8.
[33] Z. Iqbal et S. Vepřek, « Raman Scattering from Hydrogenated Microcrystalline and Amorphous Silicon », *Journal of Physics C: Solid State Physics*, vol. 15, p. 377, nov. 2000, doi: 10.1088/0022-3719/15/2/019.
[34] M. H. Brooker, C.-B. Huang, et J. Sylwestrowicz, « Raman spectroscopic studies of aqueous uranyl nitrate and perchlorate systems », *Journal of Inorganic and Nuclear Chemistry*, vol. 42, n° 10, p. 1431-1440, janv. 1980, doi: 10.1016/0022-1902(80)80109-6.
[35] N. B. Colthup, « Infrared Spectroscopy », in *Encyclopedia of Physical Science and Technology (Third Edition)*, R. A. Meyers, Éd. New York: Academic Press, 2003, p. 793-816. doi: 10.1016/B0-12-227410-5/00340-9.
[36] « Oscillateur harmonique », *Wikipédia*. 30 mars 2022. Consulté le: 21 juillet 2022. [En ligne]. Disponible sur: https://fr.wikipedia.org/w/index.php?title=Oscillateur_harmonique&oldid=192421361

[37] S. Yao, X. Zhou, et G. Hu, « Experimental study on negative effective mass in a 1D mass–spring system », *New J. Phys.*, vol. 10, n° 4, p. 043020, avr. 2008, doi: 10.1088/1367-2630/10/4/043020.
[38] P. Vandenabeele, M. Ortega-Avilès, D. T. Castilleros, et L. Moens, « Raman spectroscopic analysis of Mexican natural artists' materials », *Spectrochim Acta A Mol Biomol Spectrosc*, vol. 68, n° 4, p. 1085-1088, déc. 2007, doi: 10.1016/j.saa.2007.01.031.
[39] J. Barbillat, D. Bougeard, G. Buntinx, M. Delhaye, P. Dhamelincourt, et F. Fillaux, « Spectrométrie raman », *Techniques de l'ingénieur. Analyse et caractérisation*, vol. 4, n° P2865, p. P2865-1, 1999.
[40] D. A. Long, *Raman spectroscopy*. New York: McGraw-Hill, 1977.
[41] J.-X. Cheng et X. S. Xie, « Vibrational spectroscopic imaging of living systems: An emerging platform for biology and medicine », *Science*, vol. 350, n° 6264, p. aaa8870, nov. 2015, doi: 10.1126/science.aaa8870.
[42] L. Kastrup et S. W. Hell, « Absolute Optical Cross Section of Individual Fluorescent Molecules », *Angewandte Chemie International Edition*, vol. 43, n° 48, p. 6646-6649, 2004, doi: 10.1002/anie.200461337.
[43] F. Soldevila, J. Dong, E. Tajahuerce, S. Gigan, et H. B. de Aguiar, « Fast compressive Raman bio-imaging via matrix completion », *Optica, OPTICA*, vol. 6, n° 3, p. 341-346, mars 2019, doi: 10.1364/OPTICA.6.000341.
[44] D. Dussault et P. Hoess, « Noise performance comparison of ICCD with CCD and EMCCD cameras », présenté à Optical Science and Technology, the SPIE 49th Annual Meeting, Denver, CO, oct. 2004, p. 195. doi: 10.1117/12.561839.
[45] Horiba Scientific, « SWIFT^{TM} Ultra Fast Imaging ». https://www.horiba.com/fra/scientific/products/detail/action/show/Product/swifttm-1683/ (consulté le 19 juillet 2022).
[46] WiTec, « Ultra_Fast Raman Imaging », *Oxford Instruments*. https://raman.oxinst.com/techniques/raman-imaging (consulté le 19 juillet 2022).
[47] A. M. Kelley, « Hyper-Raman Scattering by Molecular Vibrations », *Annual Review of Physical Chemistry*, vol. 61, n° 1, p. 41-61, 2010, doi: 10.1146/annurev.physchem.012809.103347.
[48] D. Wei, S. Chen, et Q. Liu, « Review of Fluorescence Suppression Techniques in Raman Spectroscopy », *Applied Spectroscopy Reviews*, vol. 50, n° 5, p. 387-406, mai 2015, doi: 10.1080/05704928.2014.999936.
[49] S. Burgess et I. W. Shepherd, « Fluorescence suppression in time-resolved Raman spectra », *J. Phys. E: Sci. Instrum.*, vol. 10, n° 6, p. 617-620, juin 1977, doi: 10.1088/0022-3735/10/6/015.
[50] F. Ariese, H. Meuzelaar, M. M. Kerssens, J. B. Buijs, et C. Gooijer, « Picosecond Raman spectroscopy with a fast intensified CCD camera for depth analysis of diffusely scattering media », *Analyst*, vol. 134, n° 6, p. 1192-1197, juin 2009, doi: 10.1039/B821437A.
[51] A. F. Goncharov et J. C. Crowhurst, « Pulsed laser Raman spectroscopy in the laser-heated diamond anvil cell », *Review of Scientific Instruments*, vol. 76, n° 6, p. 063905, juin 2005, doi: 10.1063/1.1931205.
[52] C. Krafft, B. Dietzek, et J. Popp, « Raman and CARS microspectroscopy of cells and tissues », *Analyst*, vol. 134, n° 6, p. 1046-1057, 2009.
[53] M. Göppert-Mayer, « Über Elementarakte mit zwei Quantensprüngen », *Annalen der Physik*, vol. 401, n° 3, p. 273-294, 1931, doi: 10.1002/andp.19314010303.
[54] G. Placzek, *Rayleigh-Streuung und Raman-Effekt*. Leipzig: Akademische Verlagsgesellschaft, 1934.
[55] P. A. Franken, A. E. Hill, C. W. Peters, et G. Weinreich, « Generation of Optical Harmonics », *Phys. Rev. Lett.*, vol. 7, n° 4, p. 118-119, août 1961, doi: 10.1103/PhysRevLett.7.118.
[56] E. G. Woodbury, « Ruby laser operation in near IR », *Proc. IRE*, vol. 50, p. 2347-2348, 1962.
[57] R. W. Boyd, « Nonlinear Optics - 3rd Edition ». https://www.elsevier.com/books/nonlinear-optics/boyd/978-0-12-369470-6 (consulté le 11 juillet 2022).

[58] C. Evans, E. Potma, M. Puoris'haag, D. Côté, C. Lin, et X. Xie, « Chemical imaging of tissue in vivo with video-rate coherent anti-Stokes Raman scattering microscopy », *Proceedings of the National Academy of Sciences of the United States of America*, vol. 102, p. 16807-12, déc. 2005, doi: 10.1073/pnas.0508282102.
[59] X. Nan, J.-X. Cheng, et X. S. Xie, « Vibrational imaging of lipid droplets in live fibroblast cells with coherent anti-Stokes Raman scattering microscopy », *J Lipid Res*, vol. 44, n° 11, p. 2202-2208, nov. 2003, doi: 10.1194/jlr.D300022-JLR200.
[60] M. D. Duncan, J. Reintjes, et T. J. Manuccia, « Scanning coherent anti-Stokes Raman microscope », *Opt. Lett., OL*, vol. 7, n° 8, p. 350-352, août 1982, doi: 10.1364/OL.7.000350.
[61] A. Zumbusch, G. R. Holtom, et X. S. Xie, « Three-Dimensional Vibrational Imaging by Coherent Anti-Stokes Raman Scattering », *Phys. Rev. Lett.*, vol. 82, n° 20, p. 4142-4145, mai 1999, doi: 10.1103/PhysRevLett.82.4142.
[62] J.-X. Cheng et X. S. Xie, « Coherent Anti-Stokes Raman Scattering Microscopy: Instrumentation, Theory, and Applications », *J. Phys. Chem. B*, vol. 108, n° 3, p. 827-840, janv. 2004, doi: 10.1021/jp035693v.
[63] C. L. Evans, E. O. Potma, et X. S. Xie, « Coherent anti-Stokes Raman scattering spectral interferometry: determination of the real and imaginary components of nonlinear susceptibility $\chi^{(3)}$ for vibrational microscopy », *Opt. Lett., OL*, vol. 29, n° 24, p. 2923-2925, déc. 2004, doi: 10.1364/OL.29.002923.
[64] Y. Jung, J. Tam, H. R. Jalian, R. R. Anderson, et C. L. Evans, « Longitudinal, 3D In Vivo Imaging of Sebaceous Glands by Coherent Anti-Stokes Raman Scattering Microscopy: Normal Function and Response to Cryotherapy », *J Invest Dermatol*, vol. 135, n° 1, p. 39-44, janv. 2015, doi: 10.1038/jid.2014.293.
[65] L. G. Rodriguez, S. J. Lockett, et G. R. Holtom, « Coherent anti-stokes Raman scattering microscopy: A biological review », *Cytometry Part A*, vol. 69A, n° 8, p. 779-791, 2006, doi: 10.1002/cyto.a.20299.
[66] C. C. Moura, R. S. Tare, R. O. C. Oreffo, et S. Mahajan, « Raman spectroscopy and coherent anti-Stokes Raman scattering imaging: prospective tools for monitoring skeletal cells and skeletal regeneration », *Journal of The Royal Society Interface*, vol. 13, n° 118, p. 20160182, mai 2016, doi: 10.1098/rsif.2016.0182.
[67] R. M. Goodhead, J. Moger, T. S. Galloway, et C. R. Tyler, « Tracing engineered nanomaterials in biological tissues using coherent anti-Stokes Raman scattering (CARS) microscopy – A critical review », *Nanotoxicology*, vol. 9, n° 7, p. 928-939, oct. 2015, doi: 10.3109/17435390.2014.991773.
[68] M. Ji *et al.*, « Rapid, Label-Free Detection of Brain Tumors with Stimulated Raman Scattering Microscopy », *Science Translational Medicine*, vol. 5, n° 201, p. 201ra119-201ra119, sept. 2013, doi: 10.1126/scitranslmed.3005954.
[69] A. Karuna, F. Masia, M. Wiltshire, R. Errington, P. Borri, et W. Langbein, « Label-Free Volumetric Quantitative Imaging of the Human Somatic Cell Division by Hyperspectral Coherent Anti-Stokes Raman Scattering », *Anal. Chem.*, vol. 91, n° 4, p. 2813-2821, févr. 2019, doi: 10.1021/acs.analchem.8b04706.
[70] R. W. Hellwarth, « Theory of Stimulated Raman Scattering », *Phys. Rev.*, vol. 130, n° 5, p. 1850-1852, juin 1963, doi: 10.1103/PhysRev.130.1850.
[71] Y. R. Shen et N. Bloembergen, « Theory of Stimulated Brillouin and Raman Scattering », *Phys. Rev.*, vol. 137, n° 6A, p. A1787-A1805, mars 1965, doi: 10.1103/PhysRev.137.A1787.
[72] M. B. J. Roeffaers *et al.*, « Label-free imaging of biomolecules in food products using stimulated Raman microscopy », *JBO*, vol. 16, n° 2, p. 021118, févr. 2011, doi: 10.1117/1.3516591.
[73] M. Kasevich et S. Chu, « Atomic interferometry using stimulated Raman transitions », *Phys. Rev. Lett.*, vol. 67, n° 2, p. 181-184, juill. 1991, doi: 10.1103/PhysRevLett.67.181.
[74] J. T. Mendonça, B. Thidé, et H. Then, « Stimulated Raman and Brillouin Backscattering of Collimated Beams Carrying Orbital Angular Momentum », *Phys. Rev. Lett.*, vol. 102, n° 18, p. 185005, mai 2009, doi: 10.1103/PhysRevLett.102.185005.

[75] H. J. Lee et J.-X. Cheng, « Imaging chemistry inside living cells by stimulated Raman scattering microscopy », *Methods*, vol. 128, p. 119-128, sept. 2017, doi: 10.1016/j.ymeth.2017.07.020.
[76] R. C. Prince, R. R. Frontiera, et E. O. Potma, « Stimulated Raman Scattering: From Bulk to Nano », *Chem. Rev.*, vol. 117, n° 7, p. 5070-5094, avr. 2017, doi: 10.1021/acs.chemrev.6b00545.
[77] J.-X. Cheng, W. Min, Y. Ozeki, et D. Polli, *Stimulated Raman Scattering Microscopy: Techniques and Applications*. Elsevier, 2021.
[78] C. H. Camp Jr et M. T. Cicerone, « Chemically sensitive bioimaging with coherent Raman scattering », *Nature Photon*, vol. 9, n° 5, Art. n° 5, mai 2015, doi: 10.1038/nphoton.2015.60.
[79] J. Hahn, C. Debes, M. Leigsnering, et A. M. Zoubir, « Compressive sensing and adaptive direct sampling in hyperspectral imaging », *Digital Signal Processing*, vol. 26, p. 113-126, mars 2014, doi: 10.1016/j.dsp.2013.12.001.
[80] P. Mishra, M. S. M. Asaari, A. Herrero-Langreo, S. Lohumi, B. Diezma, et P. Scheunders, « Close range hyperspectral imaging of plants: A review », *Biosystems Engineering*, vol. 164, p. 49-67, déc. 2017, doi: 10.1016/j.biosystemseng.2017.09.009.
[81] S. Piqueras, L. Duponchel, R. Tauler, et A. de Juan, « Monitoring polymorphic transformations by using in situ Raman hyperspectral imaging and image multiset analysis », *Analytica Chimica Acta*, vol. 819, p. 15-25, mars 2014, doi: 10.1016/j.aca.2014.02.027.
[82] D. H. Foster et K. Amano, « Hyperspectral imaging in color vision research: tutorial », *J. Opt. Soc. Am. A, JOSAA*, vol. 36, n° 4, p. 606-627, avr. 2019, doi: 10.1364/JOSAA.36.000606.
[83] A. M. Fereudoun, Y. Zhang, H. K. Sulehria, A. Babakhani, et M. R. Kardan, « Super-Resolution Challenges in Hyperspectral Imagery », *Science Alert*. https://scialert.net/fulltext/?doi=itj.2008.1030.1036 (consulté le 3 août 2022).
[84] « TEM Imaging & Spectroscopy | Gatan, Inc. » https://www.gatan.com/products/tem-imaging-spectroscopy (consulté le 3 août 2022).
[85] G. McMullan, A. R. Faruqi, D. Clare, et R. Henderson, « Comparison of optimal performance at 300 keV of three direct electron detectors for use in low dose electron microscopy », *Ultramicroscopy*, vol. 147, p. 156-163, déc. 2014, doi: 10.1016/j.ultramic.2014.08.002.
[86] A. Stevens, L. Kovarik, P. Abellan, X. Yuan, L. Carin, et N. D. Browning, « Applying compressive sensing to TEM video: a substantial frame rate increase on any camera », *Advanced Structural and Chemical Imaging*, vol. 1, n° 1, p. 10, août 2015, doi: 10.1186/s40679-015-0009-3.
[87] E. J. Candes, J. Romberg, et T. Tao, « Robust uncertainty principles: exact signal reconstruction from highly incomplete frequency information », *IEEE Transactions on Information Theory*, vol. 52, n° 2, p. 489-509, févr. 2006, doi: 10.1109/TIT.2005.862083.
[88] D. L. Donoho, « Compressed sensing », *IEEE Trans. Inform. Theory*, vol. 52, n° 4, p. 1289-1306, avr. 2006, doi: 10.1109/TIT.2006.871582.
[89] R. G. Baraniuk, « Compressive Sensing [Lecture Notes] », *IEEE Signal Processing Magazine*, vol. 24, n° 4, p. 118-121, juill. 2007, doi: 10.1109/MSP.2007.4286571.
[90] J. Trzasko et A. Manduca, « Highly Undersampled Magnetic Resonance Image Reconstruction via Homotopic $_0$ -Minimization », *IEEE Transactions on Medical Imaging*, vol. 28, n° 1, p. 106-121, janv. 2009, doi: 10.1109/TMI.2008.927346.
[91] M. Tello Alonso, P. Lopez-Dekker, et J. J. Mallorqui, « A Novel Strategy for Radar Imaging Based on Compressive Sensing », *IEEE Transactions on Geoscience and Remote Sensing*, vol. 48, n° 12, p. 4285-4295, déc. 2010, doi: 10.1109/TGRS.2010.2051231.
[92] M. Leigsnering, C. Debes, et A. M. Zoubir, « Compressive sensing in through-the-wall radar imaging », in *2011 IEEE International Conference on Acoustics, Speech and Signal Processing (ICASSP)*, mai 2011, p. 4008-4011. doi: 10.1109/ICASSP.2011.5947231.
[93] M. P. Edgar, G. M. Gibson, et M. J. Padgett, « Principles and prospects for single-pixel imaging », *Nature Photon*, vol. 13, n° 1, Art. n° 1, janv. 2019, doi: 10.1038/s41566-018-0300-7.
[94] V. Studer, J. Bobin, M. Chahid, H. S. Mousavi, E. Candes, et M. Dahan, « Compressive fluorescence microscopy for biological and hyperspectral imaging », *Proceedings of the National Academy of Sciences*, vol. 109, n° 26, p. E1679-E1687, 2012.

[95] D. S. Wilcox, G. T. Buzzard, B. J. Lucier, O. G. Rehrauer, P. Wang, et D. Ben-Amotz, « Digital compressive chemical quantitation and hyperspectral imaging », *Analyst*, vol. 138, n° 17, p. 4982-4990, juill. 2013, doi: 10.1039/C3AN00309D.
[96] D. Cebeci, B. R. Mankani, et D. Ben-Amotz, « Recent Trends in Compressive Raman Spectroscopy Using DMD-Based Binary Detection », *J Imaging*, vol. 5, n° 1, p. 1, déc. 2018, doi: 10.3390/jimaging5010001.
[97] E. P. Wagner, B. W. Smith, S. Madden, J. D. Winefordner, et M. Mignardi, « Construction and Evaluation of a Visible Spectrometer Using Digital Micromirror Spatial Light Modulation », *Appl Spectrosc*, vol. 49, n° 11, p. 1715-1719, nov. 1995, doi: 10.1366/0003702953965731.
[98] G. T. Buzzard et B. J. Lucier, « Optimal filters for high-speed compressive detection in spectroscopy », in *Computational Imaging XI*, févr. 2013, vol. 8657, p. 53-62. doi: 10.1117/12.2012700.
[99] D. S. Wilcox, G. T. Buzzard, B. J. Lucier, P. Wang, et D. Ben-Amotz, « Photon level chemical classification using digital compressive detection », *Analytica Chimica Acta*, vol. 755, p. 17-27, nov. 2012, doi: 10.1016/j.aca.2012.10.005.
[100] D. Cebeci, K. Kwok, P. Wang, L. S. Taylor, et D. Ben-Amotz, « Rapid classification of pharmaceutical ingredients with Raman spectroscopy using compressive detection strategy with PLS-DA multivariate filters », *Journal of Pharmaceutical and Biomedical Analysis*, vol. 80, p. 63-68, juin 2013, doi: 10.1016/j.jpba.2013.02.029.
[101] O. G. Rehrauer, V. C. Dinh, B. R. Mankani, G. T. Buzzard, B. J. Lucier, et D. Ben-Amotz, « Binary Complementary Filters for Compressive Raman Spectroscopy », *Appl Spectrosc*, vol. 72, n° 1, p. 69-78, janv. 2018, doi: 10.1177/0003702817732324.
[102] E. O. Potma et S. Mukamel, « - Theory of Coherent Raman Scattering », in *Coherent Raman Scattering Microscopy*, vol. chapter 1, CRC Press, 2012, p. 3-42.
[103] W. E. Moerner et L. Kador, « Optical detection and spectroscopy of single molecules in a solid », *Phys. Rev. Lett.*, vol. 62, n° 21, p. 2535-2538, mai 1989, doi: 10.1103/PhysRevLett.62.2535.
[104] « Digital_D-Type_ISOLATOR.pdf ». Consulté le: 11 août 2022. [En ligne]. Disponible sur: https://ipslasers.com/wp-content/uploads/2022/07/Digital_D-Type_ISOLATOR.pdf
[105] « SM_L-Type_Turnkey_ISOLATOR.pdf ». Consulté le: 11 août 2022. [En ligne]. Disponible sur: https://ipslasers.com/wp-content/uploads/2022/07/SM_L-Type_Turnkey_ISOLATOR.pdf
[106] S. Coe, *Nebulae and How to Observe Them*. Springer Science & Business Media, 2007.
[107] « TANGO Desktop - Märzhäuser Wetzlar ». https://www.marzhauser.com/en/products/controllers/tango-desktop.html (consulté le 11 août 2022).
[108] « Semrock - Part Number: LPD02-785RU ». https://www.semrock.com/filterdetails.aspx?id=lpd02-785ru-25 (consulté le 12 août 2022).
[109] « Specification for High Efficiency Transmission Grating, T-1200-850s series », p. 2.
[110] P. Zorabedian, « 8 - Tunable External-Cavity Semiconductor Lasers », in *Tunable Lasers Handbook*, F. J. Duarte, Éd. San Diego: Academic Press, 1995, p. 369-389. doi: 10.1016/B978-012222695-3/50009-X.
[111] « dlp650lnir.pdf ». Consulté le: 12 août 2022. [En ligne]. Disponible sur: https://www.ti.com/lit/ds/symlink/dlp650lnir.pdf?ts=1660302992503&ref_url=https%253A%252F%252Fwww.ti.com%252Fproduct%252FDLP650LNIR%253Fdcmp%253Ddsproject%2526hqs%253Dtd%2526%2526bm-verify%253DAAQAAAAF_____0xuu0MWoW4btD8yZ-leshFqI9STYuACkNmR04zL-GHYAolg8PVtgN5i4LosDtaiN7wAwxYgIFMDUjxlpj4C-B5ivt4aYdRD8cEkaPmPfeOmGKquaDepBZhVPmOJljY9fC4MFkmwfX85jwgLXjVLfir15xh_oGa3aylITEs_0IgLLeKZtQSO5bTenjN_AkGXccOWBa33liINfUytIezwGSDodnwgfHyr0pQFiEjAWSxbPUrZ-9QyG2H7-2sx156T85Zs7_FsInWrg8mb5p01wF_urzIHzpz9Pg
[112] « ID120 Visible Single-Photon Detector », *ID Quantique*. https://www.idquantique.com/quantum-sensing/products/id120-visible-single-photon-detector/ (consulté le 12 août 2022).

[113] E. Abbe, « Beiträge zur Theorie des Mikroskops und der mikroskopischen Wahrnehmung », *Archiv f. mikrosk. Anatomie*, vol. 1, n° 1, p. 200-261, déc. 1873, doi: 10.1007/BF02956173.
[114] « ZEISS Microscopy Online Campus | Microscopy Basics | Numerical Aperture and Resolution ». https://zeiss-campus.magnet.fsu.edu/articles/basics/resolution.html (consulté le 19 août 2022).
[115] P. Réfrégier, E. Chevallier, et F. Galland, « Compressed Raman classification method with upper-bounded error probability », *Opt. Lett., OL*, vol. 44, n° 23, p. 5836-5839, déc. 2019, doi: 10.1364/OL.44.005836.
[116] H. G. Brittain, Éd., *Polymorphism in Pharmaceutical Solids*, 2e éd. Boca Raton: CRC Press, 2018. doi: 10.3109/9781420073225.
[117] H. Feng, R. W. Bondi, C. A. Anderson, J. K. Drennen, et B. Igne, « Investigation of the Sensitivity of Transmission Raman Spectroscopy for Polymorph Detection in Pharmaceutical Tablets », *Appl. Spectrosc., AS*, vol. 71, n° 8, p. 1856-1867, août 2017.
[118] I. R. Lewis et H. Edwards, *Handbook of Raman Spectroscopy: From the Research Laboratory to the Process Line*. CRC Press, 2001.
[119] C. Gendrin, Y. Roggo, et C. Collet, « Pharmaceutical applications of vibrational chemical imaging and chemometrics: A review », *Journal of Pharmaceutical and Biomedical Analysis*, vol. 48, n° 3, p. 533-553, nov. 2008, doi: 10.1016/j.jpba.2008.08.014.
[120] G. Févotte, « In Situ Raman Spectroscopy for In-Line Control of Pharmaceutical Crystallization and Solids Elaboration Processes: A Review », *Chemical Engineering Research and Design*, vol. 85, n° 7, p. 906-920, janv. 2007, doi: 10.1205/cherd06229.
[121] X. Audier, « Spectroscopie Raman stimulée rapide et imagerie spectrale », These de doctorat, Aix-Marseille, 2018. Consulté le: 5 septembre 2022. [En ligne]. Disponible sur: https://www.theses.fr/2018AIXM0580
[122] B. Sarri *et al.*, « Discriminating polymorph distributions in pharmaceutical tablets using stimulated Raman scattering microscopy », *Journal of Raman Spectroscopy*, vol. 50, n° 12, p. 1896-1904, 2019, doi: 10.1002/jrs.5743.
[123] J. K. Haleblian, « Characterization of Habits and Crystalline Modification of Solids and Their Pharmaceutical Applications », *Journal of Pharmaceutical Sciences*, vol. 64, n° 8, p. 1269-1288, août 1975, doi: 10.1002/jps.2600640805.
[124] E. R. Bates, W. C. Lau, et D. J. Angiolillo, « Clopidogrel–Drug Interactions », *Journal of the American College of Cardiology*, vol. 57, n° 11, p. 1251-1263, mars 2011, doi: 10.1016/j.jacc.2010.11.024.
[125] K. Raza, P. Kumar, S. Ratan, R. Malik, et S. Arora, « Polymorphism: The Phenomenon Affecting the Performance of Drugs », p. 10, 2014.
[126] N. Lakshmi Prasanthi, M. Sudhir, N. Jyothi, et V. S. vajrapriya, « A Review on Polymorphism Perpetuates Pharmaceuticals », *Am J Drug Deliv*, vol. 04, n° 05, 2016, doi: 10.21767/2321-547X.1000002.
[127] J. F. Bauer, « Polymorphism—A Critical Consideration in Pharmaceutical Development, Manufacturing, and Stability », p. 9.
[128] E. H. Lee, « A practical guide to pharmaceutical polymorph screening & selection », *Asian Journal of Pharmaceutical Sciences*, vol. 9, n° 4, p. 163-175, août 2014, doi: 10.1016/j.ajps.2014.05.002.
[129] R. Censi et P. Di Martino, « Polymorph Impact on the Bioavailability and Stability of Poorly Soluble Drugs », *Molecules*, vol. 20, n° 10, Art. n° 10, oct. 2015, doi: 10.3390/molecules201018759.
[130] Y. Roggo, K. Degardin, et P. Margot, « Identification of pharmaceutical tablets by Raman spectroscopy and chemometrics », *Talanta*, vol. 81, n° 3, p. 988-995, mai 2010, doi: 10.1016/j.talanta.2010.01.046.
[131] H. Carruthers, D. Clark, F. Clarke, K. Faulds, et D. Graham, « Comparison of Raman and Near-Infrared Chemical Mapping for the Analysis of Pharmaceutical Tablets », *Appl Spectrosc*, vol. 75, n° 2, p. 178-188, févr. 2021, doi: 10.1177/0003702820952440.

[132] S. Heuke *et al.*, « Shot-noise limited tunable dual-vibrational frequency stimulated Raman scattering microscopy », *Biomed. Opt. Express, BOE*, vol. 12, n° 12, p. 7780-7789, déc. 2021, doi: 10.1364/BOE.446348.
[133] H. Wu *et al.*, « Sub-Nyquist computational ghost imaging with deep learning », *Opt. Express, OE*, vol. 28, n° 3, p. 3846-3853, févr. 2020, doi: 10.1364/OE.386976.
[134] R. Geyer, J. R. Jambeck, et K. L. Law, « Production, use, and fate of all plastics ever made », *Science Advances*, vol. 3, n° 7, p. e1700782, juill. 2017, doi: 10.1126/sciadv.1700782.
[135] « Plastics | Initiatives | WWF », *World Wildlife Fund*. https://www.worldwildlife.org/initiatives/plastics (consulté le 15 septembre 2022).
[136] A. A. de Souza Machado, W. Kloas, C. Zarfl, S. Hempel, et M. C. Rillig, « Microplastics as an emerging threat to terrestrial ecosystems », *Global Change Biology*, vol. 24, n° 4, p. 1405-1416, 2018, doi: 10.1111/gcb.14020.
[137] A. J. Jamieson, L. S. R. Brooks, W. D. K. Reid, S. B. Piertney, B. E. Narayanaswamy, et T. D. Linley, « Microplastics and synthetic particles ingested by deep-sea amphipods in six of the deepest marine ecosystems on Earth », *R Soc Open Sci*, vol. 6, n° 2, p. 180667, févr. 2019, doi: 10.1098/rsos.180667.
[138] I. Peeken *et al.*, « Arctic sea ice is an important temporal sink and means of transport for microplastic », *Nat Commun*, vol. 9, n° 1, p. 1505, avr. 2018, doi: 10.1038/s41467-018-03825-5.
[139] S. Kühn, E. L. Bravo Rebolledo, et J. A. van Franeker, « Deleterious Effects of Litter on Marine Life », in *Marine Anthropogenic Litter*, M. Bergmann, L. Gutow, et M. Klages, Éd. Cham: Springer International Publishing, 2015, p. 75-116. doi: 10.1007/978-3-319-16510-3_4.
[140] K. Senathirajah, S. Attwood, G. Bhagwat, M. Carbery, S. Wilson, et T. Palanisami, « Estimation of the mass of microplastics ingested - A pivotal first step towards human health risk assessment », *J Hazard Mater*, vol. 404, n° Pt B, p. 124004, févr. 2021, doi: 10.1016/j.jhazmat.2020.124004.
[141] V. Hidalgo-Ruz, L. Gutow, R. C. Thompson, et M. Thiel, « Microplastics in the Marine Environment: A Review of the Methods Used for Identification and Quantification », *Environ. Sci. Technol.*, vol. 46, n° 6, p. 3060-3075, mars 2012, doi: 10.1021/es2031505.
[142] Y. K. Song *et al.*, « A comparison of microscopic and spectroscopic identification methods for analysis of microplastics in environmental samples », *Marine Pollution Bulletin*, vol. 93, n° 1, p. 202-209, avr. 2015, doi: 10.1016/j.marpolbul.2015.01.015.
[143] G. Chen, Z. Fu, H. Yang, et J. Wang, « An overview of analytical methods for detecting microplastics in the atmosphere », *TrAC Trends in Analytical Chemistry*, vol. 130, p. 115981, sept. 2020, doi: 10.1016/j.trac.2020.115981.
[144] L. Van Cauwenberghe, A. Vanreusel, J. Mees, et C. R. Janssen, « Microplastic pollution in deep-sea sediments », *Environmental Pollution*, vol. 182, p. 495-499, nov. 2013, doi: 10.1016/j.envpol.2013.08.013.
[145] K. Enders, R. Lenz, C. A. Stedmon, et T. G. Nielsen, « Abundance, size and polymer composition of marine microplastics ≥10µm in the Atlantic Ocean and their modelled vertical distribution », *Marine Pollution Bulletin*, vol. 100, n° 1, p. 70-81, nov. 2015, doi: 10.1016/j.marpolbul.2015.09.027.
[146] A. L. Lusher, A. Burke, I. O'Connor, et R. Officer, « Microplastic pollution in the Northeast Atlantic Ocean: validated and opportunistic sampling », *Mar Pollut Bull*, vol. 88, n° 1-2, p. 325-333, nov. 2014, doi: 10.1016/j.marpolbul.2014.08.023.
[147] M. Cole *et al.*, « Microplastic Ingestion by Zooplankton », *Environ. Sci. Technol.*, vol. 47, n° 12, p. 6646-6655, juin 2013, doi: 10.1021/es400663f.
[148] M. C. Goldstein et D. S. Goodwin, « Gooseneck barnacles (Lepas spp.) ingest microplastic debris in the North Pacific Subtropical Gyre », *PeerJ*, vol. 1, p. e184, oct. 2013, doi: 10.7717/peerj.184.
[149] L. Van Cauwenberghe et C. R. Janssen, « Microplastics in bivalves cultured for human consumption », *Environmental Pollution*, vol. 193, p. 65-70, oct. 2014, doi: 10.1016/j.envpol.2014.06.010.

[150] L. Zada *et al.*, « Fast microplastics identification with stimulated Raman scattering microscopy », *Journal of Raman Spectroscopy*, vol. 49, n° 7, p. 1136-1144, 2018, doi: 10.1002/jrs.5367.
[151] P. Ribeiro Claro, M. Nolasco, et C. Araújo, « Characterization of Microplastics by Raman Spectroscopy », in *Comprehensive Analytical Chemistry*, vol. 75, 2016. doi: 10.1016/bs.coac.2016.10.001.
[152] « MakroPor_002.pdf ». Consulté le: 27 septembre 2022. [En ligne]. Disponible sur: http://www.smartmembranes.de/fileadmin/user_upload/Datenblaetter/MakroPor_002.pdf
[153] A. Käppler *et al.*, « Identification of microplastics by FTIR and Raman microscopy: a novel silicon filter substrate opens the important spectral range below 1300 cm−1 for FTIR transmission measurements », *Anal Bioanal Chem*, vol. 407, n° 22, p. 6791-6801, sept. 2015, doi: 10.1007/s00216-015-8850-8.
[154] A. M. Elert *et al.*, « Comparison of different methods for MP detection: What can we learn from them, and why asking the right question before measurements matters? », *Environmental Pollution*, vol. 231, p. 1256-1264, déc. 2017, doi: 10.1016/j.envpol.2017.08.074.
[155] A. Fürstenberg, « Water in Biomolecular Fluorescence Spectroscopy and Imaging: Side Effects and Remedies », *Chimia (Aarau)*, vol. 71, n° 1-2, p. 26-31, févr. 2017, doi: 10.2533/chimia.2017.26.
[156] O. G. Rehrauer, B. R. Mankani, G. T. Buzzard, B. J. Lucier, et D. Ben-Amotz, « Fluorescence modeling for optimized-binary compressive detection Raman spectroscopy », *Opt. Express, OE*, vol. 23, n° 18, p. 23935-23951, sept. 2015, doi: 10.1364/OE.23.023935.
[157] A. Lombardini *et al.*, « High-resolution multimodal flexible coherent Raman endoscope », *Light Sci Appl*, vol. 7, p. 10, mai 2018, doi: 10.1038/s41377-018-0003-3.
[158] A. Kudlinski *et al.*, « Double clad tubular anti-resonant hollow core fiber for nonlinear microendoscopy », *Opt. Express, OE*, vol. 28, n° 10, p. 15062-15070, mai 2020, doi: 10.1364/OE.389084.
[159] D. Septier *et al.*, « Label-free highly multimodal nonlinear endoscope », *Opt. Express, OE*, vol. 30, n° 14, p. 25020-25033, juill. 2022, doi: 10.1364/OE.462361.
[160] P. Ghenuche *et al.*, « Kagome hollow-core photonic crystal fiber probe for Raman spectroscopy », *Opt. Lett., OL*, vol. 37, n° 21, p. 4371-4373, nov. 2012, doi: 10.1364/OL.37.004371.
[161] L. Challier *et al.*, « Printed Dielectrophoretic Electrode-Based Continuous Flow Microfluidic Systems for Particles 3D-Trapping », *Particle & Particle Systems Characterization*, vol. 38, n° 2, p. 2000235, 2021, doi: 10.1002/ppsc.202000235.
[162] C. Qian *et al.*, « Dielectrophoresis for Bioparticle Manipulation », *International Journal of Molecular Sciences*, vol. 15, n° 10, Art. n° 10, oct. 2014, doi: 10.3390/ijms151018281.
[163] S. Tuukkanen, A. Kuzyk, J. J. Toppari, V. P. Hytönen, T. Ihalainen, et P. Törmä, « Dielectrophoresis of nanoscale double-stranded DNA and humidity effects on its electrical conductivity », *Appl. Phys. Lett.*, vol. 87, n° 18, p. 183102, oct. 2005, doi: 10.1063/1.2117626.
[164] S. K. Srivastava, P. R. Daggolu, S. C. Burgess, et A. R. Minerick, « Dielectrophoretic characterization of erythrocytes: Positive ABO blood types », *ELECTROPHORESIS*, vol. 29, n° 24, p. 5033-5046, 2008, doi: 10.1002/elps.200800166.